Nanocomposite coatings based on quaternary metalnitrogen

Michael Walock

2012-ENAM-0037

École doctorale n° 432 : Sciences des Métiers de l'Ingénieur

Doctorat ParisTech

T H È S E

en cotutelle internationale

pour obtenir le grade de docteur délivré par

l'École Nationale Supérieure d'Arts et Métiers

Spécialité "Mécanique et Matériaux"

et

pour obtenir le grade de PhD délivre par

University of Alabama at Birmingham

Spécialité "Physics"

présentée et soutenue publiquement par

Michael J. WALOCK

le 1 novembre 2012

Nanocomposite coatings based on quaternary metal-nitrogen and nanocarbon systems

Directeurs de thèse: **Corinne NOUVEAU** / **Andrei V. STANISHEVSKY**

Jury

M. Nicolas MARTIN,	Professeur, FEMTO-ST, ENSMM Besancon	Président
M. Luc IMHOFF,	Professeur, ICB, U-Bourgogne	Rapporteur
M. Mark L. WEAVER,	Professor, Dept. of Metallurgical & Materials Engineering, U-Alabama	Rapporteur
M. S. Aaron CATLEDGE,	Assistant Professor, Dept. of Physics, UAB	Examinateur
Mme. Corinne NOUVEAU,	Maitre de Conférences-HDR, LaBoMaP, A & M ParisTech-Cluny	Examinateur
M. Andrei V. STANISHEVSKY,	Associate Professor, Dept. of Physics, UAB	Examinateur
M. Yogesh K. VOHRA,	Professor, Dept. of Physics, UAB	Examinateur

T H È S E

Indeed, what is there that does not appear marvelous when it comes to our knowledge for the first time? How many things, too, are looked upon as quite impossible until they have been actually effected?

Pliny the Elder in *Naturalis Historia*, circa 77-79 AD

NANOCOMPOSITE COATINGS BASED ON QUATERNARY METAL-NITROGEN AND NANOCARBON SYSTEMS

MICHAEL J. WALOCK

PHYSICS

ABSTRACT

For this project, CrN-WC coatings are investigated as a hybrid hard and tough material. The use of a hard-carbide with a corrosion-resistant nitride may produce tailored coatings with the desired combination of properties for use as a stand-alone protective coating, or as a basis for nanocrystalline diamond deposition. The work is divided into three stages. The initial study determined the viability of the CrN-WC system, and its use as an interlayer for nanocrystalline diamond. This successful study was followed by a variation of deposition conditions at low deposition temperature. By varying the deposition parameters, the microstructure, chemical, mechanical, and tribological behavior may be optimized. While the system has relatively good adhesion to silicon substrates, its adhesion to steel was lacking. Additionally, the system showed lower than expected mechanical properties. The final step increased the deposition temperature. The aim here was to increase adhesion and improve the mechanical properties. Prior results with other systems show consistent improvement of mechanical properties at elevated deposition temperatures. The high deposition temperature coatings showed marked improvement in various characteristics over their low deposition temperature cousins.

Keywords: hard coatings, carbide, carbo-nitride, magnetron sputtering

ACKNOWLEDGEMENTS

For me, this has been a very long journey. First, I would like to thank my advisors, Andrei Stanishevsky and Corinne Nouveau. Not only have they been extremely generous with their invaluable time, comments, and suggestions, they are also directly responsible for initiating this unique opportunity of a co-tutelle between the University of Alabama at Birmingham and Arts et Métiers ParisTech.

Next, I would like to thank Nicolas Martin for serving as president, Luc Imhoff and Mark Weaver for serving as reporters, and my examiners: Yogesh Vohra and S. Aaron Catledge. Their comments and suggestions have been a key component of this work.

I would also like to thank the combined administrations of the University of Alabama at Birmingham and Arts et Métiers ParisTech for their support of this tremendous opportunity. Specific thanks go out to Gérard Coffignal and Penny Whiteside.

While it would be impossible to thank everyone who has contributed and/or helped along the way, I would like to specifically thank Romaric Masset, Aurélien Besnard, Denis Lagadrillére, Issam Rahil, Nasser Beliardouh, Ahcene Siad, Amel Zairi, Philippe Steyer, Frédéric Herbst, Ludovic Largeau, Philippe Perez, Franck Sénéquier, Rich Martens, Johnny Goodwin, Rob Holler, Dan Stockinger, Damian Batory, Marcin Gołąbczak, Jeff Montgomery, Jerry Sewell, and Yujiao Zou. All have provided immeasurable assistance with their time, suggestions, and experimental skills. And I cannot forget the assistance of Claude Roy, Florence Dumard, Carole Wahnoun, Christine Loudot, Nathalie Laroche, Hicham Ghossein, Catherine Daniélou, Amanda Holt, and Mark Case.

Last, but far from least, I would like to thank my friends and family. Especially, I would like to thank my immediate family: Steve, (in loving memory of) Karen, Christopher, Audrey, Eric, and Jennifer. I would have never made it this far without their undying love and support.

The project described in this dissertation was primarily supported by the U.S. National Science Foundation's Materials World Network (DMR-08606521) and the French Regional Council of Burgundy. Additional funding for travel was supported by the U.S. National Science Foundation (OISE-0854945, OISE-1027692). Instrumentation was supported via the U.S. National Science Foundation (DMR-0922910, DMR-1040474) and by the U.S. National Institute of Arthritis and Musculoskeletal and Skin Diseases (R01AR056665). And finally, part of this work was performed at the Central Analytical Facility, which is supported by The University of Alabama.

TABLE OF CONTENTS

LIST OF TABLES

Table

LIST OF FIGURES

Figure

LIST OF ABBREVIATIONS

a- amorphous-

AC Alternating-Current

at. atomic

AFM Atomic Force Microscopy

bcc body-centered cubic

bct body-centered tetragonal

c- cubic-

CSM Constant Stiffness Mode

CVD Chemical Vapor Deposition

DC Direct-Current

DFT Density-Functional Theory

DLC Diamond-Like Carbon

E Young's Modulus

EBSD Electron Back-Scatter Diffraction

EDS Energy Dispersive X-ray Spectroscopy

EM Electromagnetic

ESCA Electron Spectroscopy for Chemical Analysis

fcc face-centered cubic

FEG Field Emission Gun

FoV Field of View

FWHM Full-Width Half-Maximum

h- hexagonal-

H Hardness

H_s Scratch Hardness

hcp hexagonal close packed

HIPIMS HIgh Power Impulse Magnetron Sputtering

HR-SEM High-Resolution Scanning Electron Microscope

HR-TEM High-Resolution Transmission Electron Microscope

HW-CVD Hot-Wire Chemical Vapor Deposition

ICB Laboratoire Interdisciplinaire Carnot de Bourgogne

ICDD International Center for Diffraction Data

IB-MS Ion Beam-Magnetron Sputtering

LaBoMaP Laboratoire Bourguignon des Matériaux et Procédés

LPCVD Low-Pressure Chemical Vapor Deposition

MDT Movchan-Demchishin-Thornton

MPCVD Microwave Plasma Chemical Vapor Deposition

nc- nanocrystalline-

nc-D nanocrystalline-Diamond

NEH No External Heating

PDF Powder Diffraction File

PEMS Plasma-Enhanced Magnetron Sputtering

PSI Phase Shift Interferometry

PVD Physical Vapor Deposition

R_a Average Roughness

R_{RMS} Root Mean Square Roughness

RF Radio-Frequency

SCE Saturated Calomel Electrode

SEM Scanning Electron Microscope

UHV Ultra-High Vacuum

UHV-CVD Ultra-High Vacuum Chemical Vapor Deposition

UMS Unbalanced Magnetron Sputtering

UAB University of Alabama at Birmingham

UPS Ultraviolet Photoelectron Spectroscopy

VSI Vertical Scanning Interferometry

WDS Wavelength Dispersive X-ray Spectroscopy

wt. weight

XRD X-ray Diffraction

XPS X-ray Photoelectron Spectroscopy

CHAPTER I

INTRODUCTION

1.1 Overview

Since the early Stone Age [1], cutting tools have been ubiquitous elements within society. They have played a key role in our development as a species and as a civilization [2]. While stone and bone tools remained the state of the art for well over 3 million years, man continuously sought to improve on these early devices. For example, handles were added to improve the ease of use, effectiveness, and efficiency [3, 4]. Firing of stone tools increased their durability [5]. However, around 8000 years ago and the advent of the early Bronze Age, metallurgy was developed [6, 7] . Starting with copper, followed shortly by bronze, man was able to harness the power of metal tools for the first time. This stage of development lasted throughout the dynastic periods of Egypt.

However, around 1800 BC, ironworking began in earnest [8, 9]. The development of steel followed [10]. However, early steel making processes were difficult and expensive. Steel did not become ubiquitous until the Bessemer process was introduced in the middle of the 19^{th} century [11]. Improvements in the steel-making process rapidly developed, along with the introduction of more exotic compounds, such as cemented carbides. However, even these modern tools show the same defects as our early hand-axes: they wear out and can be expensive to replace.

1.2 Introduction to Protective Coatings

Tool wear and corrosion are surface-driven processes. Therefore, there are two available methods to extend tool-life: development of new bulk materials for the body of the tool and/or develop surface protection schemes, such as coatings. By applying a surface-treatment, such as a protective coating, the tool's wear properties can be tailored for specific operating environments. However, the means for producing consistent and economical surface treatments were lacking. Not until the 1960's, with the development of physical vapor deposition techniques, did scientists began developing effective wear-resistant coatings which significantly improved tool lifetime over prior techniques [12–15].

1.3 Types of Protective Coatings

Protective coatings for tools can be classified into three categories, dependent on the nature of their bonds: metallic, covalent, and ionic. Metallic compounds share their conduction electrons. Effectively, an electron gas is distributed across the substance, shared by the positively charged nuclei located at the lattice sites. Typically, metallic bonding leads to high electrical and thermal conductivity, high boiling points, ductile, and luster. And, since the bonding is not directional, metallic compounds are usually very ductile. Table 1.1 lists some relevant protective coatings with metallic bonding.

Covalent bonds are the localized version of metallic bonding. Here, electrons are shared between neighboring atoms rather than the whole lattice. For example, H_2 is covalently bonded[1]. A stable balance between attractive and repulsive forces allows the two atoms to share their electrons. Due to the strength of this bond, covalent compounds tend to be very strong, with high melting points. However, the directional nature of this bond lends to a characteristic brittleness. And the lack of

[1] At high pressure, hydrogen is known to form metallic bonding.

delocalized electrons result in low electrical and thermal conductivities. Table 1.2 lists some relevant covalent coatings used as protective coatings.

Ionic materials are the result the electrostatic attractive of opposite charges. A prime example is table salt, NaCl. This is formed by the combination of a sodium cation (positively-charged ion) and chloride anion (negatively-charged ion). Purely ionic bonds cannot exist, there is always some amount of covalent bonding between the ions. Bonds are considered primarily ionic when their character dominates the material. Generally, this occurs with a large difference in the electronegativities[2] of the relevant atoms. Table 1.2 lists some ionic compounds and properties which are relevant to the protective coating industry.

The most successful protective coatings are typically metallic in nature. The nature of the bonding is probably the main reason for the success of the metallic coatings. Most tools are made out of materials with similar bonding structure: metals. While it is possible to manufacture adherent covalent and/or ionic protective coatings, it is typically easier (and less costly) to produce metallic coatings on metal substrates.

[2]This is the tendency for an atom, or functional group, to attract an electron towards itself.

Table 1.1: Properties of binary metallic hard materials [16].

Phase	Density (g/cm^3)	Melting Point (°C)	Hardness (GPa)	Young's Modulus (GPa)	H^3/E^2 (GPa)
TiB_2	4.50	3225	30	560	0.086
TiC	4.93	3067	28	470	0.099
TiN	5.40	2950	21	590	0.027
ZrB_2	6.11	3245	23	540	0.042
ZrC	6.63	3445	25.6	400	0.105
ZrN	7.32	2982	16	510	0.016
VB_2	5.05	2750	21.5	510	0.038
VC	5.41	2648	29	430	0.13
VN	6.11	2177	15.6	460	0.018
NbB_2	6.98	3040	26	630	0.044
NbC	7.78	3613	18	580	0.017
NbN	8.43	2204	14	480	0.012
TaB_2	12.58	3040	21	680	0.02
TaC	14.48	3985	15.5	560	0.012
CrB_2	5.58	2188	22.5	540	0.04
Cr_3C_2	6.68	1810	21.5	400	0.06
CrN	6.12	1050	11	400	0.008
Mo_2B_5	7.45	2140	23.5	670	0.03
Mo_2C	9.18	2517	16.6	540	0.016
W_2B_5	13.03	2365	27	770	0.033
WC	15.72	2776	23.5	720	0.022
LaB_6	4.73	2770	25.3	(400)	0.10

Table 1.2: Properties of binary covalent and ionic hard materials [16].

Phase	Density (g/cm^3)	Melting Point (°C)	Hardness (GPa)	Young's Modulus (GPa)	H^3/E^2 (GPa)
Covalent					
B_4C	2.52	2450	40	441	0.33
c-BC	3.48	2730	∼50	660	0.29
Diamond	3.52	3800	∼100	1050	0.91
B	2.34	2100	35	470	0.19
AlB_{12}	2.58	2150	26	430	0.095
SiC	3.22	2760	26	480	0.076
SiB_6	2.43	1900	23	330	0.11
Si_3N_4	3.19	1900	17.2	210	0.115
AlN	3.26	2250	12.3	350	0.015
Ionic					
Al_2O_3	3.98	2047	21	400	0.058
Al_2TiO_5	3.68	1894	...	13	...
TiO_2	4.25	1867	11	205	0.032
ZrO_2	5.76	2677	12	190	0.048
HfO_2	10.2	2900	7.8	...	...
ThO_2	10.0	3300	9.5	240	0.015
BeO	3.03	2550	15	390	0.022
MgO	3.77	2827	7.5	320	0.004

1.3.1 Binary Compounds

In addition to the nature of the bonding, protective coatings can be grouped according to the number of elements: binary compounds are formed from two elements, ternary compounds add a third element, quaternary compounds add a fourth element, and so on. Binary compounds have been very successful as protective coatings on a wide variety of tools. One of the most successful has been TiN, a metallic compound. TiN coatings have relatively good mechanical properties (H $\sim$ 31 GPa; E $\sim$ 550 GPa [17]), and decent corrosion resistance, with the added bonus of an attractive, goldish color. However, thermal stability may be an issue, with possible oxidation at temperatures as low as 500 °C [18].

Another successful binary coating has been another metallic compound, CrN. It is a very good barrier to corrosion [19–22], and these coatings prevent oxidation, up to $\sim$ 700 °C. And thick CrN coatings have demonstrated low wear [23]. However, these films have the drawback of low hardness, ($\sim$ 11 GPa [16]). CrN films tend to form with a porous, columnar structure [24–27]. This tends to not only lower their hardness, but it also reduces their usefulness as corrosion and oxidation inhibitors. The microstructure can be improved with higher growth temperatures, resulting in improved mechanical properties [28]. With regards to the corrosion resistance, one solution is the application of a metal buffer layer between the substrate and the CrN film. This has shown to improve both the oxidation and corrosion resistance of CrN films [20, 29, 30].

With its high melting point and high hardness [31], tungsten carbide (metallic) has played a prominent role in the tool industry since the beginning of the last century. However, its most stable form, hexagonal- (h-)WC, tends to be brittle and is easily damaged [32]. Further development was facilitated with the formulation of a composite: tungsten carbide grains embedded in a metal matrix (usually, cobalt). This cemented-WC has excellent hardness, strength, and fracture

toughness. Unfortunately, both WC and cemented-WC suffer from low thermal stability. At temperatures as low as 500 °C for WC and 600 °C for cemented-WC oxidization and strength deterioration begins to occur [31, 33]. In addition, the prominent wear mechanism for cemented-WC seems to be preferential removal of the relatively soft metal [34–36], which negates the improved ductility of the material.

With its excellent mechanical, chemical, physical, and electronic properties, tungsten nitride has found use in a wide variety of applications. It has proven to be an effective diffusion barrier in microelectronics , preventing the formation of copper silicides up to 600 °C [37]. Tungsten nitride has also shown to be useful in the catalytic conversion of nitrous oxide [38]. As a protective coating, tungsten nitride has excellent wear properties up to 300 °C [39]. Unfortunately, this very low oxidation temperature limits the use of tungsten nitride in mechanical applications.

1.3.2 Ternary Coatings

While some of these binary coating systems are still in wide use, further technological advances in materials are necessary to further improve the efficiency and durability of protective coatings. Tertiary solid solutions were the next step in development, and have proven to be very successful. By adding a third element to the traditional binary compounds, researchers have started to tailor the coating properties to the application. There are many good examples of this, such as W-Al-C [40, 41], W-Al-N [42], Cr-W-N [43–45], Cr-Al-N [46], Cr-Si-N [47], Cr-Mo-N [48], Ti-C-N [49–51], and Ti-Al-N [52–55].

For example, adding Al to CrN improves both the hardness and the thermal stability of CrN [56]. Using Si in lieu of Al, further improves the hardness, with the advantage of lower friction [57, 58]. For the TiN system, adding aluminum can increase the thermal stability to 800 °C [18, 59], and depending on the amount of the Al, the mechanical properties can be improved, with low Al-content systems

show the greatest improvement in hardness, at 42 GPa, but with high modulus $\sim$ 520 GPa. Adding aluminum can drop the hardness to 29 GPa, but the system becomes more ductile, with E $\sim$ 325 GPa [54].

1.3.3 Structural modifications

1.3.3.1 Superlattices

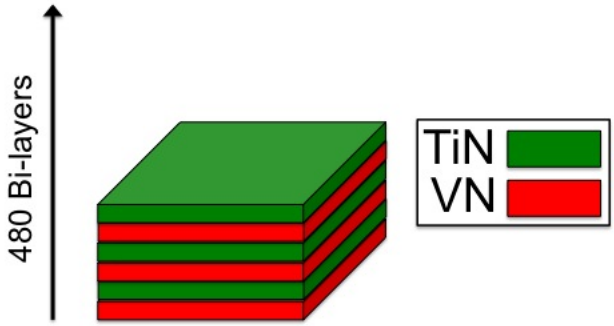

Figure 1.1: Schematic diagram of a TiN/VN superlattice structure, based on the results of Helmersson, et al. [60]. The complete 2.5 μm coating consists of 480 layers of 2.6 nm thick TiN and 2.6 nm thick VN.

Another effort to improve traditional coatings is with superlattices. Superlattices consist of thin coatings, in a repeated bilayer. As shown in Fig. 1.1, a typical example is a 2.5 μm TiN/VN coating, with 480 bilayers of 2.6 nm thick TiN and 2.6 nm thick VN layers [60]. The resulting mechanical properties are significantly higher than the properties of the constituent layers, see Table 1.3. Another example is AlN/CrN. Single layer AlN and CrN films have measured hardnesses of 16.2 GPa and 26.7 GPa, respectively. However, when combined in a superlattice structure (with bilayer period of 3.8 nm), the composite H is 40 GPa. This is significantly higher than the H calculated by rule-of-mixtures, 21.5 GPa [61].

Of course, the obvious question is why; what mechanisms are at play? There are several models that offer insight into the mechanisms at play. There are several competing models for this behavior. One is based on dislocation blocking. If the

dislocation line energies (which are proportional to the Young's moduli of the coatings) are significantly different, dislocations propagation over the interface is not energetically favorable [75, 76]. Additionally, for maximum enhancement, it is necessary for thin component layers with minimal interface width; this limits dislocation motion within the layers [77]. While this model has done particularly well in describing the hardness enhancement [78, 79], dislocation blocking may not be the only mechanism at play.

Another possible mechanism for hardness enhancement is strain [80], due to lattice mismatch. Here, the blocking of dislocation propagation is the result of the interface structure. In most superlattice structures, the component materials will have lattice mismatch. However, epitaxial growth can still be accomplished via one of two different mechanisms: (a) lattice matching via strain, leading to coherent interfaces, or (b) an incoherent interface, with significant defects. In either case, the free energy of the system is increased. As the bilayer thickness is decreased, coherent interfaces are more favorable. The resulting increase in the strain field inhibits dislocation propagation [81].

However, there is a limit to this increase. Below a critical thickness, interdiffusion begins to play a significant role, and interfaces begin to blur. With the loss of sharp interfaces, the strain is relaxed. Lower strain equals improved dislocation propagation, and decreased hardness. As the bilayer thickness is increased, incoherent interfaces become more favorable, leading to lower strain. However, it is generally agreed that strain-blocking is a small effect compared to dislocation-blocking [82]. As such, it may only be prominent in superlattice systems with structural transformations [61, 83, 84], or relatively small differences in elastic moduli.

In summary, the key to hardness enhancement in superlattices are clean interfaces, with small bilayer thicknesses ($5 \sim 10$ nm). Unfortunately, these

requirements are the primary limiting factors on the use of superlattices in the tool industry. For example, research-scale machines can accurately produce these highly-technical films, industrial-scale processes may not have the accuracy to do so over the course of time. Inconsistency in the bilayer period can significantly affect the overall mechanical properties of the coatings. Additionally, the interfaces need to be clean and sharp. Unfortunately, in many industrial uses, tools suffer heating. Heating leads to diffusion, and blurring of the interfaces.

1.3.3.2 Nanocomposite films

Nanocomposites are an improvement on the idea of superlattices. In a typical composite, there are at least two materials with little or no solubility between the constituent phases. When the crystallite sizes shrink to less than 10-20 nm, the system is now considered a nanocomposite (see Fig. 1.2). For example, single crystal diamond films are superhard, but have low toughness. In addition, its high crystallinity may lead to high surface roughness. To overcome these difficulties, a nanocomposite of graphitic C and diamond is formed:
nanocrystalline-Diamond (nc-D)[3].

The combination of multiple phases, with nanoscale crystallites, leads to changes in the dislocation behavior. In traditional materials, dislocation nucleation and movement occurs primarily within the grains. This process leads to a building up of dislocations at the grain boundary (a.k.a. pile-up), which increases the stress field at the boundary. Upon reaching a critical point, the stress field is relieved by the movement of the dislocations through the grain boundaries, and into other grains. In nanostructured materials, such as nanocrystalline- (nc-)metals or nanocomposites, the reduced grain-size limits dislocation nucleation and movement. In turn, this limits the pile-up of dislocations at grain boundaries. As a result, the

[3]However, adhesion is still an issue. Typically, significant surface modification is necessary for good adhesion to a wide variety of substrates [85–91].

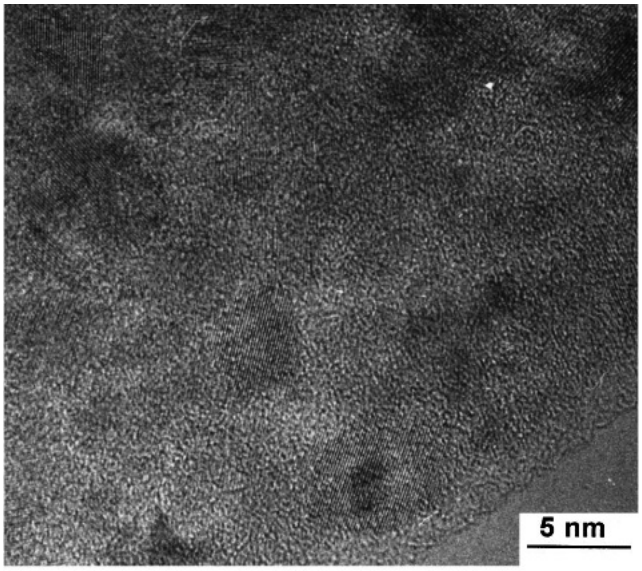

Figure 1.2: High-resolution transmission electron micrograph of TiN/SiN nanocomposite coating. The (111) and (200) lattice planes of TiN nanocrystals are clearly visible, due to their orientation with respect to the electron beam. These nearly spherical crystallites are surrounded by an amorphous Si_3N_4 matrix [92].

critical stress becomes unattainable and dislocation movement stalls. This is known as Hall-Petch hardening [93, 94], and can be analytically described by a simple relationship

$$H = H_0 + kd^{-1/2} \tag{1.1}$$

where H is the measured film hardness H_0 is the intrinsic hardness of the bulk material, k is a material-based constant, and d is the grain size[4].

This relationship has been found to hold true down to $\sim$ 10-20 nm [96, 97]. However, further decreases in the grain size results in a decrease in the system hardness [98]. This is probably due to a combination of diffusional creep [99], grain-boundary sliding (i.e. nucleation and movement of dislocations within the

[4]The original Hall-Petch relationship described the effects of decreasing grain size on the yield stress, σ_y. However, modern usage relates the effects of grain size on the Hardness (H). This is possible with application of Tabor's rule, $H \approx 3\sigma_y$ [95].

grain boundaries) [100], and triple-junction effects [101].

Nanocomposites consist of at least two immiscible phases. This miscibility gap permits the formation of a nanocomposite, rather than a solid solution, via spinodal decomposition. Spinodal decomposition is a thermodynamically-driven phase transformative process. Effectively, thermodynamics forces a decomposition from a metastable phase to the stable constituent phases. For example, according to *ab initio* Density-Functional Theory (DFT) calculations, c-$Ti_{1-x}Al_xN$ is only stable above 4010 °C which is higher than the melting temperatures of either TiN or AlN [102]. At lower temperatures (of either deposition or annealing), the system separates into TiN and AlN phases. This precipitation into the constituent phases increases the mechanical properties of the system; there are more obstacles to dislocation movement.

While there have been reports of nanocomposites formed from multiple nc-phases [103] and from nc-phase/metal [104, 105], the typical system has a crystalline phase imbedded in an amorphous matrix. The crystallite sizes (i.e. grain sizes) have a wide range, from $1 \sim 30$ nm. This range seems a bit counterintuitive, due to the transition range from Hall-Petch hardening to softening, i.e. grains $10 \sim 20$ nm. However, the main processes for the transition are diffusional creep and/or grain boundary shear. If these can be avoided, the transition to softening may never occur, and the hardness enhancement due to grain size reduction would continue unhindered [106].

This seems to be confirmed by *ab initio* calculations by Hao et al. [107] and Zhang et al. [108, 109]. They clearly demonstrate that the maximum enhancement occurs with a single atomic layer for the amorphous- (a-)matrix of a nanocomposite. The addition of a second atomic layer in the matrix would significantly reduce the hardness.

An excellent example of a nanocomposite is nc-TiN combined within an

a-Si_3N_4 matrix. This combination has shown a hardness greater than diamond [110–115], with excellent thermal stability. Table 1.3 lists some examples of nanocomposites. Some nanocomposites may not reach superhardness, but are considered supertough, such as nc-TiC/a-C [116–119] and nc-WC/a-C [120–122]. However, these films suffer from low thermal stability [123].

Table 1.3: Properties of structurally modified protective coatings [62].

Material	H (GPa)	E (GPa)	H^3/E^2	Comments
Bulk				
Diamond	100	1050	0.91	
Boron	35	470	0.19	[63]
Sapphire	30	441	0.14	[64]
Amorphous				
Diamond-Like Carbon (DLC)	65	550	0.91	[65]
a-C	>59	>395	$\sim$ 1.3	Produced by cathodic arc [66]
Nanocrystalline				
nc-ZrC	23	325	0.12	T_{growth} = 290 °C; d = $\sim$ 3.5 nm [67]
Superlattice				
CrN/WN	31	200	0.71	Bilayer period = 24 nm [68]
CrN/CrC	21	198	0.24	Bilayer period = 5.4 nm [69]
Nanocomposite				
nc-TiN/a-Si_3N_4	48	$\sim$ 565	$\sim$0.34	[70]
nc-TiN/a-BN	69	585	0.96	[71]
nc-TiAlN/a-AlN	47	402	0.64	[53]
nc-W_2N/a-Si_3N_4	51	560	0.42	[70–72]
nc-Mo_2C/a-(C + Mo_2N)	49	440	0.61	[73]
nc-WC/a-Cu_3N	41	396	0.41	[74]

1.4 Materials selection for protective coatings

The future of protective coatings seems to lie with nanostructured materials, either superlattices or nanocomposites. And given the wide variety of materials, and the number of possible combinations, it would be useful to describe the desired material properties for a new protective coating. For superlattices, the desired material phases should:

- be immiscible. This allow for sharp interfaces, with little interdiffusion (i.e. no alloy formation in an interfacial phase).
- have a large difference in the elastic moduli for enhanced dislocation-blocking.
- have similar lattice spacing for epitaxial growth. However, an exact match is unnecessary (and may be detrimental) because the strain field from induced lattice matching will contribute to the hardness enhancement[5].
- have a bilayer period within the sweet spot, $\sim$ 5-10 nm. This will assist the dislocation-blocking of the elastic moduli difference by limiting the total number of dislocations possible within the individual layers. Additionally, this size limit increases the strain field which also contributes to the enhancement.

For nanocomposites, the desired material combination are very similar and the phases should:

- be immiscible. This allow for good phase segregation in the nanocomposite, with little interdiffusion (i.e. no alloy formation).
- have a large difference in the elastic moduli. Dislocation-blocking is key to hardness enhancement.

[5]Crystal structure match may be unnecessary. During epitaxial growth, some systems, such as AlN, will undergo a phase transformation [124, 125].

- have nanocrystalline grains, with very thin grain boundaries (to prevent diffusional creep and grain boundary sliding).

Up until now, the vast majority of research in nanostructured coatings has been on nitride/nitride [126–129], nitride/metal [130–133], nitride/a-C [134, 135], carbide/metal [136], and carbide/a-C [137, 138] combinations. There have been few publications on carbide/nitride nanostructured systems [74, 139, 140]. Here, the goal of this research is the deposition and characterization of a nanocomposite coating system based on a carbide/nitride combination.

1.5 CrN-WC material system

Going back to Section 1.3.1, CrN and WC are both excellent materials as binary coatings. Both systems offer excellent corrosion protection in acidic media, which may be useful in coating wood-cutting tools [141–144]. Additionally, the two materials have similar thermal stability/oxidation resistance. While the oxidation temperature is too low for metal-cutting operations (tool faces may reach $\geq$ 800 °C), it should be sufficient for many wood-cutting operations (tool faces may be $\leq$ 500 °C) [145, 146].

In addition to their potential use in wood-cutting, there is interest in using CrN-WC coatings as an interlayer for nc-D deposition. In many cases, significant chemical or physical pretreatments are necessary for adherent nanocrystalline-Diamond growth. Unfortunately, these processes can be difficult, time-consuming, and dangerous. Another possible method is the use of interlayers rather than physical seeding or chemical etching. However, if a soft material is used, it may weaken the overall mechanical properties of the system. Therefore, it is desirable to form interlayers with reasonable mechanical properties of their own. One possibility is a nanocomposite system. As stated in Section 1.3.3.2, nanocomposites have significant mechanical properties, and with the selection of the

proper constituents, the coatings may be suitable interlayers for subsequent nc-D deposition. Both CrN [147, 148] and WC [149–151] are suitable for adherent nc-D growth. But, will these materials combine to form a suitable nanocomposite?

CrN and WC would form a quaternary component coating. The literature on these types of coatings is relatively limited, and the phase diagram is non-existent. However, there is evidence of a miscibility gap in the Cr-W system below 1677 °C [152]. However, when either carbon or nitrogen are added to the system, the solubility improves. Cr-W-N is available across a wide range of temperatures and compositions [43–45, 153, 154]. Cr-W-C is significantly more limited, with very little diffusibility of Cr in WC [155]. In other words, this system does not quite meet the immiscibility requirement of Sec. 1.3.3.2, but it is pretty close.

Referring to the second requirement for successful nanocomposites, CrN and WC do have a large difference in the elastic moduli. And while the exact numbers depend on the deposition conditions, Table 1.1 gives WC an E $\sim$ 720 GPa and CrN an E $\sim$ 400 GPa. This is similar to the elastic moduli difference of other successful nanocomposite systems, such as TiN/SiN (590 GPa for TiN; 210 GPa for Si_3N_4) and TiN/AlN (590 GPa for TiN; 350 GPa for AlN) [16]. And as for the remaining requirement, nc-grains, with very thin grain boundaries, are completely possible with the appropriate growth conditions.

Therefore, it is reasonable to expect some amount of success in the following goals:

- the deposition CrN-WC nanocomposite coatings with good mechanical properties;
- the deposition of adherent nc-D coatings on CrN-WC, without additional surface treatments.

CHAPTER II

METHODOLOGY

2.1 Experimental Design

This project consisted of three phases to investigate the optimal parameters for hard, protective coatings based on CrN-WC. In the summer of 2009, a study was conducted to determine the viability of the system: were hard, adherent CrN-WC coatings possible, and would nanocrystalline-Diamond (nc-D) grow on these coatings without additional pre-treatment? This successful study was followed by a variation of deposition conditions at low deposition temperature. By varying the deposition parameters, the microstructure and relevant chemical, mechanical, and tribological behavior may be optimized and controlled. While moderately successful as tribological coatings, CrN-WC coatings (deposited at low temperature) suffered from adhesion problems and lower than expected mechanical properties.

The final step increased the deposition temperature. The aim here was to increase adhesion, and assist with the spinodal phase segregation - leading to improved mechanical properties. Prior results with other multi-phase systems, as noted in Section 1.3.3.2, show consistent improvement of mechanical properties at elevated deposition temperatures. These high deposition temperature coatings showed marked improvement in chemical, mechanical, and tribological properties over their low deposition temperature cousins.

At each stage of the project, the properties of the CrN-WC coatings were thoroughly investigated. The surface topography was measured with AFM and HR-SEM; internal structure was imaged with cross-sectional HR-SEM. XRD

yielded the crystallographic structure. Chemical composition was evaluated with EDS, Raman spectroscopy, and X-ray Photoelectron Spectroscopy (XPS). Optical profilometry measured wafer curvature; combining this with the Stoney equation, stress is determined. The mechanical and tribological properties were investigated with nanoindentation, scratch testing, and pin-on-disc tribometry.

2.2 Deposition

2.2.1 Sputter Deposition

Sputtering is a simple, effective Physical Vapor Deposition (PVD) technique to deposit a vast array of coating materials. It was developed in the 1960s (based on work from the Second World War). In this technique, inert gas (argon is the most common) is injected into a high vacuum chamber at low pressure. The gas particles interact with free electrons within the chamber. As a result, a small portion of the gas becomes ionized. This ionized gas is attracted to a negatively biased "target" material. The resulting momentum transfer from the impact releases material from the target. The released material has a finite probability of depositing onto any interior surface of the chamber, as shown in Fig. 2.1. Depending on the placement of a substrate holder, significant amounts of material can be deposited, leading to the formation of coatings on any substrates mounted on the holder.

Unfortunately, with a standard Direct-Current (DC) power supply, the technique was limited to conducting materials. During sputtering, dielectric materials would develop a positive surface charge. The result is a significant decrease in the number of impinging gas ions; eventually, the surface charge would be large enough to stop ions from impacting the target surface[1]. No impacts, no sputtering. However, by applying an RF power signal, or through pulsing a DC

[1]This applies to conducting targets in a reactive gas environment as well. During the sputtering process, some amount of chemical reactions will take place on the target surface, leading to the formation of dielectric compounds on the surface of a conductor.

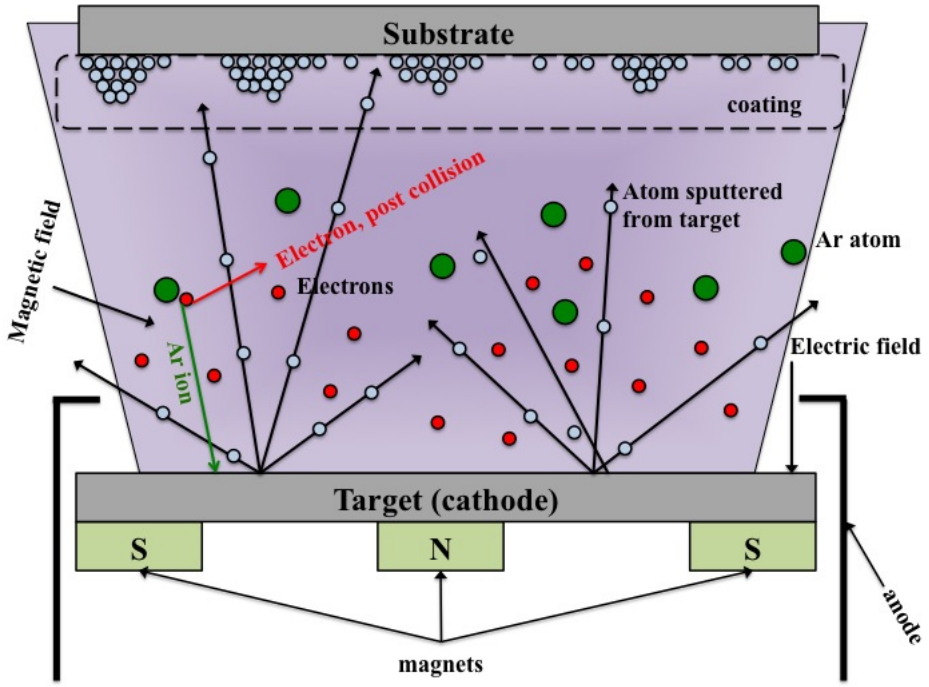

Figure 2.1: Schematic of the sputtering process.

signal, the surface charge can be eliminated. This expands the sputtering technique to dielectric materials. Additionally, mixing the reactive gases in with the inert gas has further broadened the capabilities of sputtering systems [156].

Other improvements to the basic sputtering process have improved gas ionization, and/or increased the energy of the gas ions. For example, in magnetron sputtering, a set of permanent magnets are placed behind the target material. The magnetic field lines trap free electrons in the vacuum chamber (see Fig. 2.1). When gas is injected, there is a higher probability of an ionization event [157, 158]. While this increases the deposition rate over traditional sputtering, there is a drawback. The use of a magnetic field to trap the electrons increases the impacts along the field lines. As such, only a fraction of the target material is utilized before the target material is completely removed from the "racetrack" formed by the impacts along the field lines. This characteristic dimple can be seen in Fig. 2.2.

With Plasma-Enhanced Magnetron Sputtering (PEMS), a hot filament

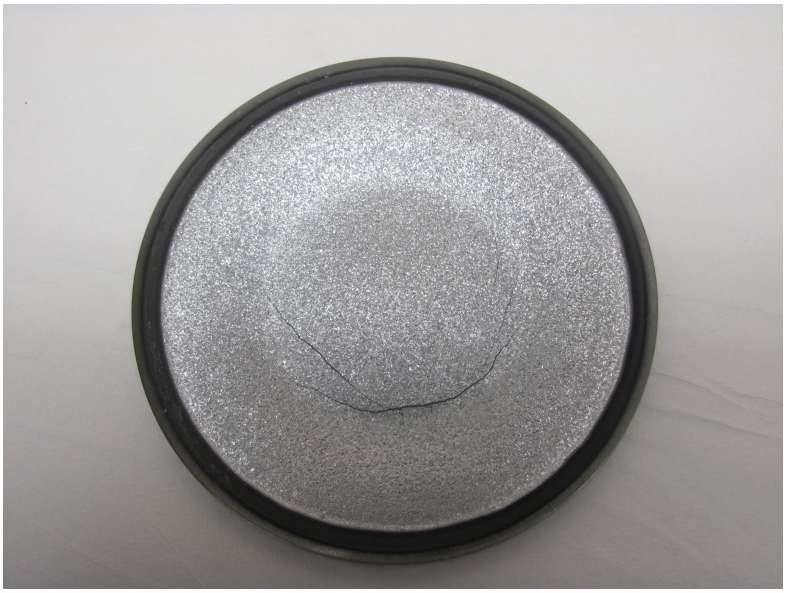

Figure 2.2: A used 4-in Cr target which shows the characteristic racetrack of magnetron sputtering, and the beginning of target "burn-through," i.e. the cracking observed in the lower part of the target resulting from extensive use.

releases extra electrons into the chamber, with the same effect: increased gas ionization [159]. In HIgh Power Impulse Magnetron Sputtering (HIPIMS), a high power pulse is cycled on/off for a short amount of time, at a low duty cycle. A typical pulse of several kV·cm^{-2} for about 10 μs. To avoid target overheating (subsequent melting), the pulses only occur during about 10 % of the entire deposition time. This high power pulsing leads to an increase in both the gas ionization and the energy of individual ions [160]. For both improvements, i.e. PEMS and HIPIMS, the increase in gas ionization leads to increased ion bombardment of the substrates before and during the deposition process. As will be explained in Section 2.2.3, the increased ion bombardment leads to an increases in film density and adhesion.

In this project, a modified Nordiko 3500 sputtering system (see Fig. 2.3) was used to deposit the CrN-WC coatings in all phases. The original Nordiko 3500 used a single 4-in planar magnetron sputtering source, with RF electronics (1.25 kW,

Figure 2.3: The modified Nordiko 3500 sputtering system used for depositing the CrN-WC coatings, located at LaBoMaP, Cluny, France. The inset shows the interior of the chamber, and the arrangement of the substrate holder with respect to the two 4-in, confocally-arranged magnetron sputtering guns.

13.56 MHz), to deposit a wide array of materials onto various substrate materials. Since its installation at the LaBoMaP, the system has undergone a major modification with the installation of a second 4-in planar magnetron sputtering gun, see the inset of Fig. 2.3. This second gun is also powered by an RF source (1.25 kW, 13.56 MHz). The center of the substrate holder is 8 cm from the guns, see Fig. 2.4(a). Substrate bias is provided by a 600 W DC power supply; sample heating can be achieved by attaching a custom-designed, 4-in $\times$ 4-in, 5 Ω (125W) resistive heater, see Fig. 2.4(b), to the 8-in diameter substrate holder. This is powered by a 1200 W, Alternating-Current (AC) power supply. Maximum temperature is 350 °C, as read by a shielded K-type thermocouple attached to the heater surface.

Rough vacuum is provided by an Alcatel 2063C rotary vane pump, with a peak speed of 18 L/s and an ultimate base pressure of 0.2 Pa. However, before reaching this pressure, cross-over for this system is set at 7 Pa; pressure is monitored by a DV-23 thermocouple gauge, marked TC-1 on Fig. 2.5. Here, the

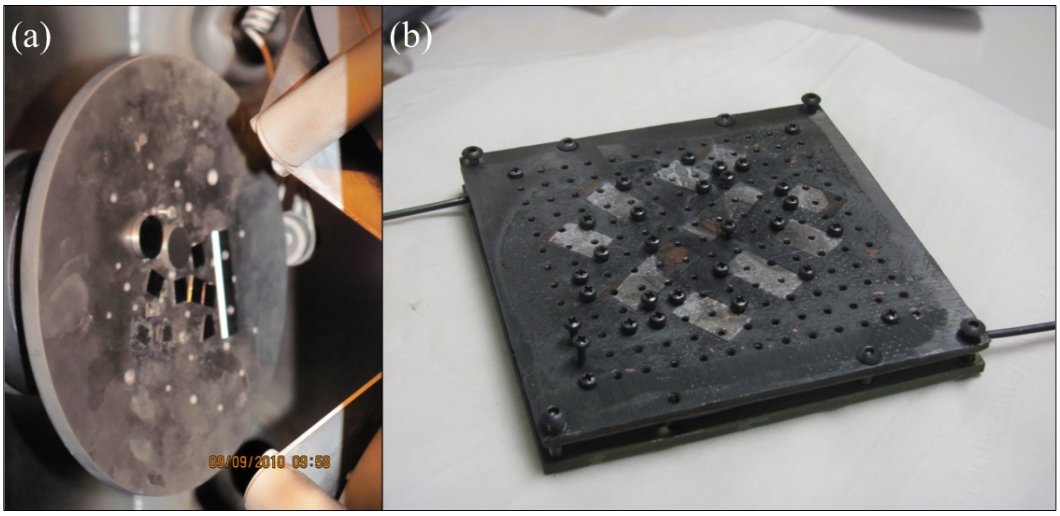

Figure 2.4: (a) The 8-in diameter substrate holder and (b) the 4-in × 4-in custom substrate heater for the Nordiko vacuum system. These images are not to scale; when mounted, the substrate heater moves the samples about 1 cm closer to the sputtering guns.

main pumping is switched to a CryoTorr 8 cryogenic pump (peak N_2 pumping speed of 1500 L/s) via the valve marked HV in Fig 2.5[2]. This pumping arrangement reaches an ultimate base pressure of 2×10^{-5} Pa in approximately 6-8 hours. Pressure from middle to high-vacuum is monitored by two cold cathode Penning gauges: an Alcatel CF2P gauge head, with an Alcatel FN121 controller, and a BOC Edwards CP25EK gauge head, with a BOC Edwards 505 controller. These are identified as PG1 and PG2, respectively, on Fig. 2.5.

Three separate gases can be individually controlled and injected into the chamber, through the mass flow controllers, marked MFC's on Fig. 2.5, for both normal and reactive sputtering. During sputtering, pressure is monitored by a Barocell 655AB capacitance manometer with BOC Edwards ADD controller, identified as CM on Fig. 2.5. While most vacuum gauges are calibrated to N_2, and

[2]Overtime, the cryogenic pump needs to be purged of gas molecules that have built up within the pump. This regeneration is accomplished by isolating the both the cryopump and roughing pump from the main chamber via valves HV and RV, respectively. Once isolated, the cryopump is turned off, valve FV is opened, and the pump is allowed to come to room temperature. As the temperature increases, the adsorbed molecules are released and pumped away by the roughing pump.

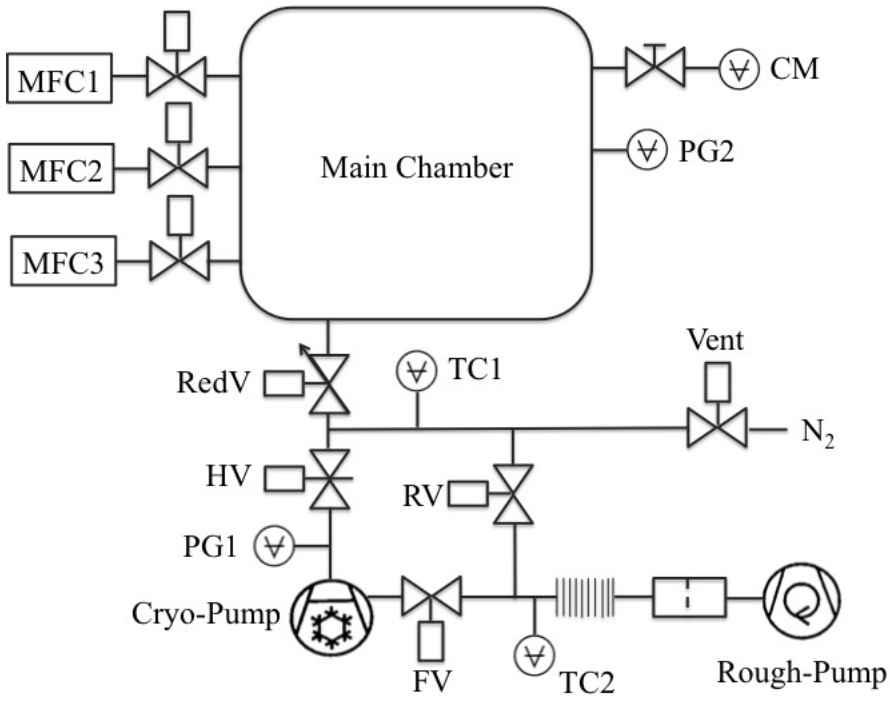

Figure 2.5: Vacuum diagram of the modified Nordiko 3500 sputtering system.

need correction factors to accurately read the pressure of other gas species, capacitance manometers are gas insensitive. These gauges will read the correct total pressure, regardless of the gas species within the chamber. To reduce gas consumption during sputtering, the system pumping speed is reduced by a reduction valve, RedV on Fig. 2.5.

2.2.2 Chemical Vapor Deposition

With PVD, a physical target is used to generate the necessary adatoms for film growth. In Chemical Vapor Deposition (CVD), the "targets" are volatile chemical precursors. While there are several types of CVD deposition tools, the process is effectively the same. A substrate is exposed to volatile chemical precursors, which will either react and/or decompose on the sample surface to form the desired compound. The main differences between the different types of CVD are the operating pressures and the excitation sources.

Obviously, atmospheric CVD processes are carried out at, or near, atmospheric pressures ($\sim$ 101 kPa). Atmospheric processes offer the advantages of lower cost, due to the lack of vacuum equipment. A good example of this is combustion CVD. Here, precursors are added to an open flame. The high temperature of the flame decomposes the precursor into highly reactive intermediates. During this, the desired substrate is passed over the flame, and the intermediates condense on its surface to form the desired film. By optimizing the deposition parameters (i.e. flame, speed of substrate, substrate temperature, substrate-to-flame distance), high quality films, with a wide range of morphologies and optimized for a variety of applications can be easily grown [161–165]. Additionally, this technique can be highly conformal for very thin films. Unfortunately, the number of suitable precursors limits this technique to only a few materials, mostly oxides.

Most modern processes in use are low-pressure ($\sim$ 5 kPa) or Ultra-High Vacuum (UHV) ($\sim 10^{-6}$ Pa). This allows for much more precise control over the reaction chamber atmosphere, yielding higher quality films. Additionally, it opens the possibility to far more excitation sources, such as plasma-based sources. In turn, the additional excitation sources (and available energies) increase the number of available precursors for coating deposition. Low-Pressure Chemical Vapor Deposition (LPCVD) and Ultra-High Vacuum Chemical Vapor Deposition (UHV-CVD) techniques are far more versatile than atmospheric techniques.

A good example is Hot-Wire Chemical Vapor Deposition (HW-CVD). This low-vacuum technique uses a hot-wire, or hot-filament[3], to crack the precursor molecules into reactive intermediates. It is simple to operate, very scalable, and can deposit a wide range of metals, semiconductors, and insulators. Additionally, a

[3]The main difference is the temperature of the heat source. In hot-wire CVD, the wire it typically $\sim$ 1600 °C. For hot-filament, the temperature is increased to $\sim$ 2100 °C.

hot-wire can easily be added to most CVD systems for additional excitation.

Another advantage to low vacuum processes is plasma production. Typical deposition plasmas have a low fractional ionization. As a result, free electrons within the gas maintain a high energy, on the order of several eV, and the vast majority of the gas remains near room temperature. The result is precursor dissociation, and free radical generation, at lower temperatures than would be possible with only thermal excitation. There are a wide variety of methods to generate plasmas: microwave, radio-frequency, electron cyclotron resonance, arc-discharge, and dc glow discharge.

A very common plasma deposition technique is MPCVD. With this technique, the plasma is generated with a microwave signal, electromagnetic radiation in the GHz range. With this plasma-excitation source, it is possible to reach high plasma densities with a high degree of spatial localization. While this spatial localization is very useful for deposition uniformity (within the plasma ball) and for use as a remote plasma source, it is not as easily scalable as other CVD techniques.

Nanocrystalline diamond (nc-D) deposition was accomplished with a Wavemat MPDR microwave plasma chemical vapor deposition system, see Fig. 2.6. This 6 kW system operates at 2.4 GHz. Pumping is provided by a rotary vane pump, leading to a system base pressure of 1.3 Pa. Substrate heating is obtained from the plasma. Typical temperatures are approximately 800 °C for metal substrates and approximately 700 °C with semiconductor substrates. The temperature is measured with a two-color infrared pyrometer system[4] [166].

Growth dynamics for nc-D are not the subject of this study. The main interest in using this system is to check the viability of growing nc-D coatings on CrN-WC, without additional surface treatments. As such, the deposition conditions

[4]The optics for this system have been modified to reduce plasma interference.

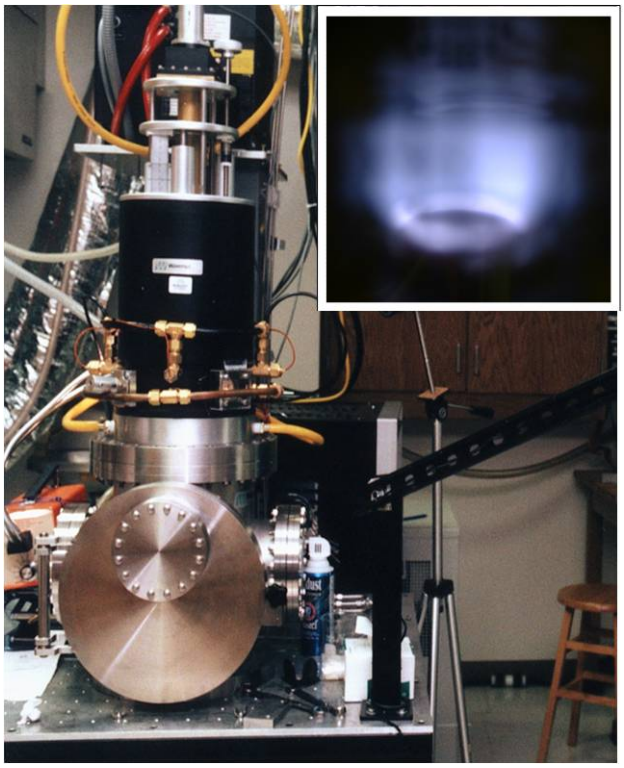

Figure 2.6: The 6 kW, 2.4 GHz Wavemat MPDR microwave-plasma chemical vapor deposition system. This system is used to deposit nanocrystalline diamond films at UAB, Birmingham, AL USA. The inset shows a typical plasma during deposition.

were not varied, and are reported in Table 2.1.

Table 2.1: Deposition conditions for growth of nanocrystalline-Diamond (nc-D) coatings.

Parameter	Conditions
Working Pressure	5.3 kPa
Gas mixture	
H_2	84 %
N_2	1.5 %
CH_4	14.5 %
Substrate Temperature	720 °C
Deposition Time	7 h

2.2.3 Effects of Deposition Parameters on Film Structure

Modern deposition techniques, such as sputtering or MPCVD, can yield a wide variety of coatings, with an equally wide array of properties. Often, those properties are dependent on the microstructure. Luckily, film microstructure can be related to the deposition conditions. In 1969, Movchan and Demchishin presented the three zone model, based on a generalized temperature, T^*. This model was originally developed for evaporative films. However, Thornton expanded this model to include effects from the sputtering gas pressure [167, 168]. As a result, the zone transitions were refined and a few added, such as zone T (a transition zone between zones 1 and 2); this extension has become known as the Movchan-Demchishin-Thornton (MDT) model.

The generalized temperature is a ratio of the deposition temperature (in K) and the coating melting (in K) temperature, T_s/T_m. Growth in zone 1, i.e. low temperature ($T^* < 0.1$), is dominated by low adatom mobility. The film will basically grow along the directions of the incident flux. The end result are tapered crystallites, separated by voids. As the crystallites grow, atomic shadowing coupled with low adatom mobility, create the voids between the crystallites. This porous structure does not have many true grain boundaries. Higher argon pressures will allow this zone to persist to significantly higher T^* than at lower sputtering pressures. Additionally, contamination can also lead to localized zone 1 structures. This is a direct result of reduced adatom mobility. As the generalized temperature moves into zone T ($0.1 < T^* < 0.3$), adatom mobility also increases. Surface diffusion begins to play a more significant role, and dominates over atomic shadowing. The voids are filled, and true grain boundaries begin to form. Tightly-packed, fibrous grains (with a smooth domed surfaces) are characteristic for this zone.

Zone 2 ($0.3 < T^* < 0.5$) has even higher adatom mobility; bulk diffusion

becomes the dominant process. This leads to grain boundary migration and possible recrystallization of the coating. Columnar grains extend the full coating thickness, and are separated by true grain boundaries. Additionally, it should be noted that grain size also increases with increases in the generalized temperature. Changes in the working pressure do not seem to have the same effect as with earlier zones. This may be due to reduced gas adsorption at the surface, during the deposition process. Zone 3 ($0.5 < T^* < 0.75$) has equiaxed grains and faceted surfaces. Above $T^* \sim 0.75$, grains remain equiaxed, but the surface moves to flat tops.

Unfortunately, the MDT model neglects to include effects from ionization events, i.e. plasma-coating interactions. This is a shame, as it has long been known that energetic ion effects can significantly affect the coating microstructure. However, the gap has been filled with a revised structural zone map [169]. The new map includes effects from the incident energy flux, via a normalized energy flux E^*, and thickness, via a net thickness t^*.

As shown in Fig. 2.7, the generalized temperature axis still remains, but it now includes a temperature shift caused by the potential energy of the incoming particles. This potential energy term,

$$E_{pot} = E_c + (E_{ion} - \phi) \tag{2.1}$$

includes the heat of sublimation, i.e. the cohesive energy, Ec, and the ionization energy E_{ion} which is reduced by the electron's work function, ϕ. Obviously, the latter term does not apply to the sputtered atoms, but it can be very significant for multi-charged ions. For metals and singly-charged ions, E_c is $\sim$ 1-9 eV/atom, E_{ion} is $\sim$ 4-10 eV/atom, and the electron work function is $\sim$ 4 eV.

The potential energy term can be converted to a characteristic temperature

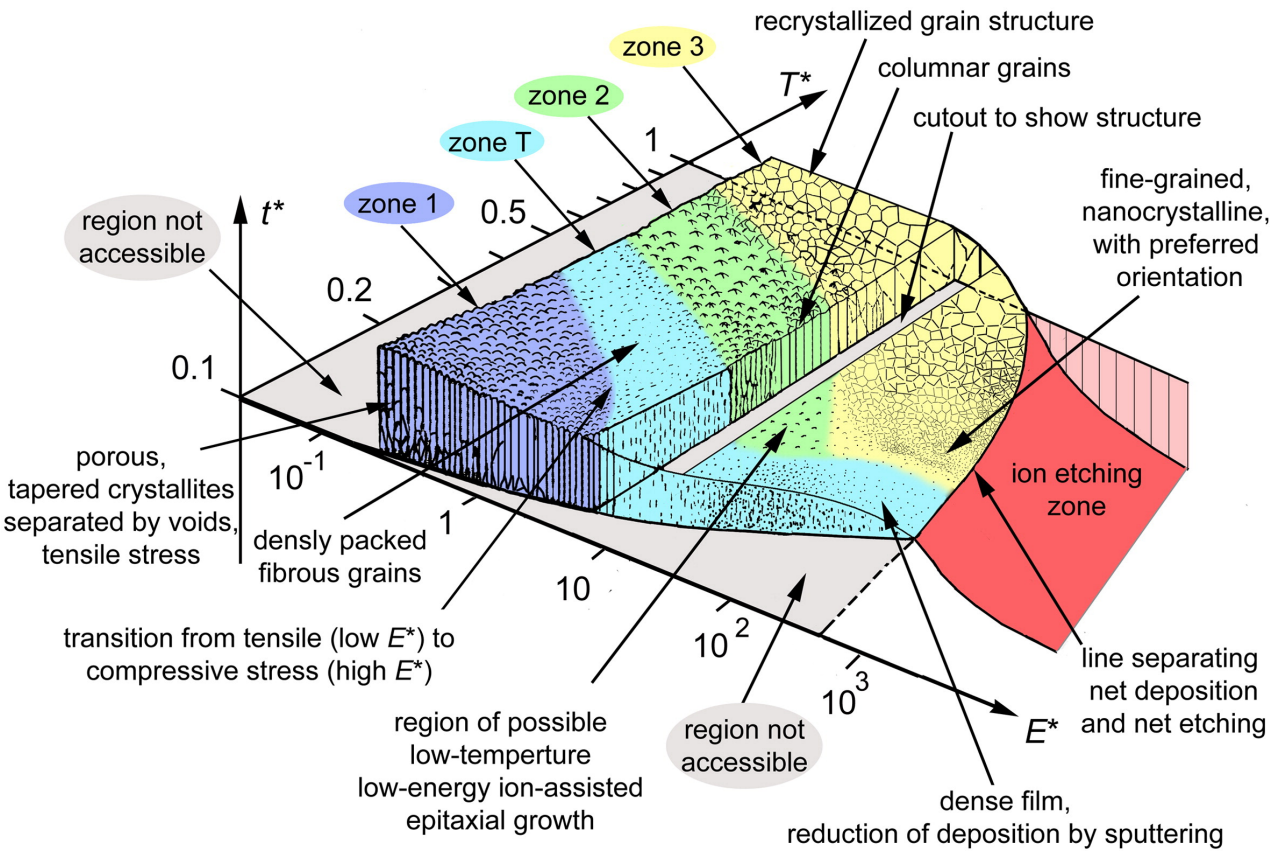

Figure 2.7: An extended version of the film structural zone diagram for energetic depositions which includes plasma and ion effects on thin film growth [169]. The main axes are the generalized temperature T^*, the normalized energy flux E^*, and the net thickness t^*. Zone boundaries are gradual, and for illustration only.

by

$$T_{pot} = \frac{E_{pot}}{kN_{moved}} \tag{2.2}$$

where k is the Boltzmann constant, and N_{moved} is the number of atoms rearranged in the heated region. Therefore, the new temperature scale is

$$T^* = T^*_{MDT} + T_{pot} \tag{2.3}$$

where T^* is the generalized temperature of the extended model, T^*_{MDT} is the

generalized temperature of the MDT model, and T_{pot} is the characteristic temperature of the potential energy.

The pressure axis, which more or less represented kinetic effects in the MDT model has been replaced with a logarithmic axis of normalized energy flux, E^*. This normalized flux consists of an initial plasma component E_0, plus the changes due to ion acceleration with the voltage sheath between the plasma and substrate surface V_{sheath},

$$E^* = E_0 + QeV_{sheath} \tag{2.4}$$

where Q is the ion charge state and e is the elementary charge.

Ions can affect film growth in different ways. If the ion energy is insufficient for penetration into the growing film, it may still promote surface diffusion. As such, it may be possible for epitaxial film growth with few defects in the bulk film. If the ions penetrate, there is localized atomic-scale heating. For a very short time (on the order of picoseconds), this impact will enhance the adatom mobility of the surrounding region. Depending on the balance of the ion's kinetic and potential energies, atomic displacement can occur, and defects can be created, or annihilated. These processes can greatly affect the resulting film stress.

Additionally, the third axis has now been labeled as the net film thickness. This provides a means of showing the affects on the growth rate, due to the potential and kinetic energy effects presented on the x- and y- axes[5]. Note, these changes do not affect the structures observed for each zone, but rather shifts and extends the zone boundaries.

[5]As shown in Fig. 2.7, etching effects from impacting ions can now be shown on the diagram.

2.3 Characterization

2.3.1 Atomic Force Microscopy

Effectively, Atomic Force Microscopy (AFM) is a refinement of the traditional stylus profilometer. In stylus profilometry, a diamond stylus is dragged across the surface. The interaction of the tip with surface features will deflect the height of the stylus. By measuring this vertical deflection, a 3D map of the surface can be measured. With an AFM, the tip's radius of curvature is reduced from the micrometer regime to the nanometer regime. The typical arrangement has the Si, SiN, or diamond nanoscale tip mounted on a cantilever. Using piezoelectric elements, the cantilever is scanned across the sample surface. The deflections of the cantilever-tip system are measured via capacitive sensors, optical interferometry, or the reflection of laser light into a position sensitive detector. As the tip is scanned across the surface, a feedback mechanism is employed to keep a constant force between the sample and the probe. This significantly reduces the risk of damaging the tip and/or the sample through an inadvertent collision.

Depending on the application, the feedback mechanism can be static or dynamic. In static, or contact mode, the tip is kept in constant contact with the sample surface. Using piezoelectric actuators, a constant cantilever deflection acts as the feedback. Recording the adjustments necessary to maintain this deflection yields an accurate 3D map of the surface. Unfortunately, this scan mode is prone to noise and thermal drift. Additionally, over time the tip will suffer degradation.

Dynamic mode measurements involve the oscillation of the cantilever slightly above its resonance frequency; the oscillations are only a few nanometers. Interaction with surface forces, such as Van der Waals or capillary forces, will reduce the resonance frequency of the cantilever-tip system. The driving frequency is adjusted to maintain a constant oscillation. This provides both the measurement

and the feedback loop. With this mode, the tip does not suffer degradation effects. Due to the lack of actual contact, this technique is an excellent choice for soft materials, or imaging adsorbed monolayers on the surface of thin films.

In many cases, ambient conditions lead to the development of a meniscus layer on the sample surface, which can cause sticking problems. To counter this, a dynamic contact mode can be used; this is commonly called intermittent contact, AC, or tapping mode AFM. Similar to regular dynamic (non-contact) AFM, the cantilever system is driven near resonance, but the oscillations are significantly larger (100 nm rather than 10 nm). The measurement and feedback mechanism is also similar to dynamic mode.

For the CrN-WC samples under study, the surface morphology was measured with a Veeco Topometrix Explorer. A v-shaped, high-resonance SiN cantilever with a pyramidal tip radius of 50 nm and a force constant of 0.032 N/m was used to explore the surface roughness via contact mode, at ambient laboratory conditions.

2.3.2 Scanning Electron Microscopy

The Scanning Electron Microscope (SEM) uses a beam of high-energy electrons to image the surfaces of different samples, at significantly higher resolution than an optical microscope. Traditional machines use thermionic emission from a heated wire to produce electrons[6]. Electrons from this hot-cathode are accelerated by their attraction to a positively-charged anode. Newer machines are typically armed with a Field Emission Gun (FEG). In this type of source, a sharp-pointed emitter is held at high negative potential with respect to a nearby electrode. The resulting gradient electric field causes emission of electrons. The resulting beam is typically smaller, more coherent, and with higher brightness compared to thermionic sources. Another type of source is the Schottky FEG. This is sort of a

[6]The wire is typically made of W or LaB_6.

combination of the two sources. An electric field is used to lower the energetic barrier to electron emission from a heated emitter tip. This enhances the thermionic emission of the system.

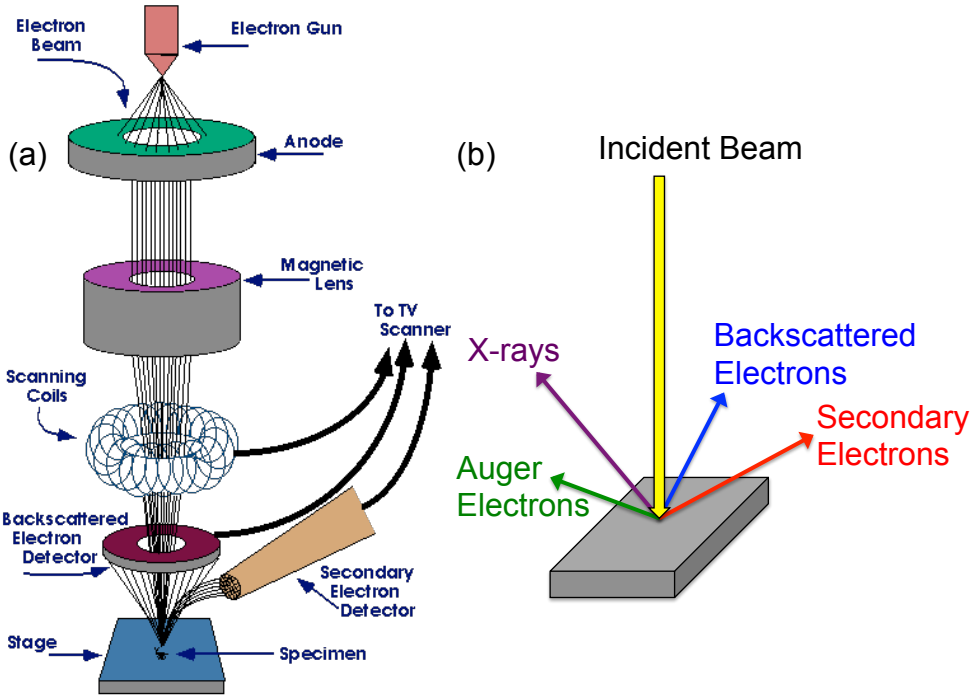

Figure 2.8: Schematic drawing of (a) the typical Scanning Electron Microscope (SEM) column [170], and (b) sample-beam interactions within a SEM.

Whatever the source, a proportion of the electrons will move past the anode. These are focused by a series of magnetic lens to a spot size of only a few nanometers, as shown in Fig. 2.8. This high-energy beam interacts with the sample surface (as shown in Fig. 2.8), producing secondary electrons, back-scattered electrons, Auger electrons, x-rays, and heat. Rastering the beam fulfills two objectives. First, rastering a small diameter beam allows the capture of the full sample surface. Additionally, changing the size of the raster changes the magnification of the image.

Secondary electrons are low-energy electrons which are ejected from the sample via inelastic scattering with the incident high-energy electrons. These are

typically low energy, and from the first few nanometers of the sample surface. Deeper electrons would suffer from scattering off other atoms. These are primarily used for imaging the sample's surface morphology. This is accomplished via a scintillator-photomultiplier system, such as the Everhart-Thornley detector. For detection, a scintillator material is located within a Faraday cage (with a low positive bias). The resulting interaction releases a photon. Using a waveguide, the photon is directed to a conversion device, such as a photomultiplier tube or CCD camera. The result is a 2D intensity distribution matching the sample morphology.

Backscattered electrons are the result of elastic scattering of the incident electrons from the sample surface. The scattering cross-section is dependent on the atomic number of the sample. Heavier materials will scatter more than lighter materials. Therefore, atomic contrast (in multi-component samples) can be imaged by symmetrical collection of the backscattered electrons. Additionally, these can be used to reveal crystallographic information via the projection of Kikuchi lines on a phosphor screen.

When secondary electrons are ejected, a hole is left in the core shell. It is possible for this shell to be filled by a higher orbital electron, but the higher shell electron must lose energy. This energy loss can be emitted in the form of a photon (x-rays) or transmitted to another electron which is ejected from its orbital (Auger process[7]). Both the x-rays and the electrons will carry environmental information (i.e. chemical composition and its ionization state). The main difference is where the information comes from. Electron-photon interactions have a low scattering cross section, i.e. the photon mean free path is longer because of the lower probability of electron-photon interactions. Therefore, the information is in-depth; it comes from atoms near the surface and through the sample thickness. However, Auger electrons are limited to the near surface region. This is due to the

[7]Auger processes are denoted by three letters (such as KLL or LMM): the shell of the initial hole, the hole-filling electron's orbital, and the orbital of the ejected electron.

significantly higher probability of electron-electron interactions.

Three different machines were used in this research, Fig. 2.9. The main unit was a JEOL JSM 6400F. This tool uses a FEG to produce electrons for high-resolution imaging (1.5 nm at 30 keV) of the sample surface and cross-section. Images were taken at an accelerating voltage of 20 keV, and the typical chamber pressure was less than 1×10^{-4} Pa. Additional images were taken with another FEG-SEM, the FEI Quanta 650. This high-resolution SEM has environmental capabilities. As pressure increases, the electron mean free path decreases. As such, SEM's typically operate in the mid- to high-vacuum range. However, this limits the machine to characterizing vacuum-compatible samples, with low outgassing. With this option, the SEM is capable of imaging non-conductive[8] and/or hydrated samples within a variable, controlled environment. This can be extremely useful in the study of biological samples. However, for this study, this capability was unnecessary. All samples are inorganic coatings, with negligible outgassing and reasonable conductivity.

Figure 2.9: Pictures of (a) a JEOL JSM-6400F [171] (ICB, Dijon, France), (b) a FEI Quanta 650 [172] (UAB, Birmingham, AL USA), and (c) a JEOL JSM-5900LV (LaBoMaP, Cluny, France). The JEOL JSM-5900LV is equipped with an Oxford INCA x-act EDS/WDS system.

The final machine was a JEOL JSM 5900LV. This traditional SEM used a W-filament and has low-vacuum capability. While not as versatile as an

[8]One of the limits of SEM research is the necessity of a conducting sample. If the sample is insulating, charge from the incident electrons will build-up, and distort the image.

environmental SEM, it is still useful for the study of high-outgassing materials, such as coal. However, for this study, this option was not utilized as all samples are high-vacuum compatible; this apparatus was mainly used for Energy Dispersive X-ray Spectroscopy (EDS) compositional analysis.

2.3.3 Energy Dispersive X-ray Spectroscopy

As mentioned above in Sec. 2.3.2, the production of secondary electrons will lead to a relaxation process within the sample. This relaxation process can lead to the emission of x-rays. The energy of the emitted photons are element-specific yielding the chemical composition of the sample in a spectrum, as shown in Fig. 2.10. Once the x-ray is emitted, they are collected by the detector. Typically, this is a semiconductor crystal which converts the photon into an electrical signal. This is accomplished through a series of ionizations within the semiconducting crystal[9]. The ejected electron and its associated hole are swept in opposite directions, producing a charge directly proportional to the x-ray energy.

A complimentary technique is Wavelength Dispersive X-ray Spectroscopy (WDS). Here, rather than collecting the x-rays with a semiconducting crystal, the x-rays are diffracted by a crystal with a clearly defined lattice structure. Only x-rays meeting the appropriate Bragg condition will be diffracted. Since each element produces its own x-ray with characteristic energy (i.e. wavelength), the elemental composition can be sequentially determined. This is accomplished by rotating the diffracting crystal with respect to the incident x-rays. While this system has higher resolution than EDS, the data collection times are higher than EDS. Additionally, WDS is more sensitive to lighter elements. With many light elements,

[9]Si, doped with Li, was the first detector, and is still very common. However, there is growing use of Silicon drift detectors, high-purity Si crystals with very low leakage currents are surrounded by a series of ring electrodes. These electrodes produce a transverse electric field, which causes the charge carriers to "drift" towards a collection electrode. The new design provides significant signal amplification over older designs and reduces noise.

such as boron, the signal-to-noise ratio is relatively low, and it can be difficult to accurately determine the amounts present. As such, EDS for bulk analysis, and is combined with WDS for trace and/or light element analysis. With proprietary software, the spectra of either EDS or WDS can be converted into a quantitative list of atomic, and weight, concentrations. Unfortunately, these data sets do not include information about the chemical bonding arrangement of the sample.

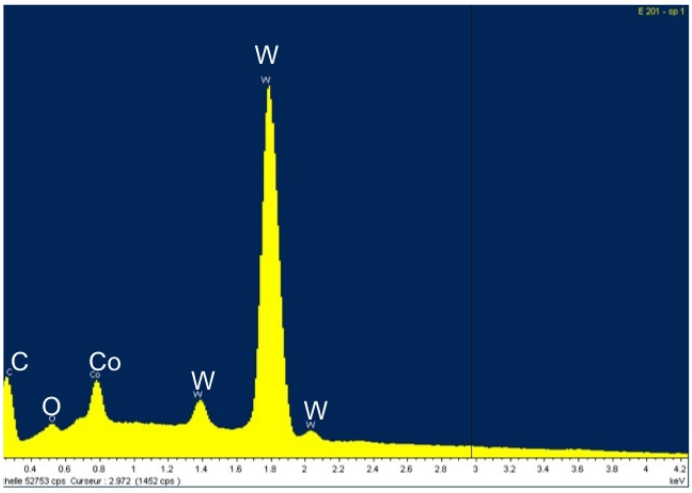

Figure 2.10: Energy Dispersive X-ray Spectroscopy (EDS) spectrum from a cemented carbide (WC-6 wt. %-Co) coating on Si.

Using the Oxford INCA x-act system mounted on the JEOL JSM-5900LV, the chemical composition was determined by EDS. The accelerating voltage was 5 keV, with an integration time of 100 s. The EDS was calibrated with WDS prior to data collection. This improves the accuracy of the results without sacrificing the quick acquisition times of Energy Dispersive X-ray Spectroscopy (EDS).

2.3.4 X-ray Diffraction

In 1901, the first Nobel Prize in Physics was awarded to Wilhelm Röntgen for his discovery of x-rays in 1895. Ever since this humble beginning, x-rays have been a valuable characterization tool in a wide variety of fields. The key is

scattering. Scattering describes the interaction of a wavefront with non-uniformities within the transversing medium. A clear example is the interaction of photons with water droplets in the air after a rainstorm, i.e. a rainbow.

Effectively, scattering can be classified into two categories: inelastic and elastic. Inelastic scattering events change the kinetic energy of the incoming particles. During the interaction, some kinetic energy is either lost or gained by the incident particle[10]. Elastic scattering events do not change the incoming particles kinetic energy. Admittedly, all scattering events are inherently inelastic. There is always some change in the kinetic energy of the incoming wavefront[11]. But, in many cases, the kinetic energy of the incident beam is large enough to ignore the inelastic effects, and the scattering event can be treated as elastic.

Rayleigh scattering is a good example of an elastic scattering process. Here, incoming photons interact with the electron cloud of an atom (or molecule). The result is the "re-emission" of the incoming electromagnetic wave with the same frequency (i.e. energy); there is some blurring, but these are inelastic effects. The outbound waves (photon packets) will interact and interfere with each other. When the phases of the outbound waves are incoherent, destructive interference is the result. However, when the phases are coherent, constructive interference leads to intense peaks at specified locations. These peak locations can be explained by Bragg's Law,

$$n\lambda = 2d\sin\theta \tag{2.5}$$

where n is an integer, λ is the x-ray wavelength, d is the spacing of the diffraction planes, and θ is the angle between the incident beam and the scattering plane. As shown in Fig. 2.11, scattered waves from an interior plane must travel an additional

[10]This should not be confused with inelastic collisions, where the total kinetic energy of the system is not conserved.

[11]It is key to remember that light is both a particle (photon) and a wave.

path-length of $2d\sin\theta$ to meet the in-phase condition for constructive interference. This law holds for practically any wavefront passing through a regular array of obstacles.

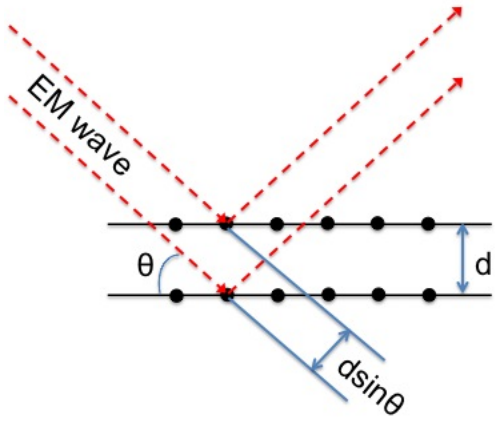

Figure 2.11: Schematic drawing for meeting the Bragg condition. The wavefront scattered from particles on the interior plane must travel an additional path-length of $2d\sin\theta$ to remain in-phase with the scattered wavefronts from the external plane.

Crystals are a perfect example of a regular array of obstacles (i.e. atoms). However, the spacing between the atoms (lattice spacing) is too small to meet the diffraction condition for visible light. Here, the only suitable radiation has wavelengths on the same order, or smaller than the typical lattice spacing of the relevant crystal. As such, crystal diffraction is limited to high energy Electromagnetic (EM) waves (i.e. x-rays and gamma rays) or thermal matter waves[12] (such as electrons, muons, protons, or neutrons).

Crystals are classified by their Bravais lattice, which describes the arrangement of the atoms within the lattice. Since the position of the atoms will define the scattering planes, different Bravais lattices satisfy different Bragg conditions. Luckily, these effects can be summarized by a set of extinction conditions, and the relationship between the diffraction plane d and the lattice

[12]de Broglie postulated that any well-isolated object suffers from wave-particle duality. In other words, the particle demonstrates both wave and particle characteristics, simultaneously. This was first proved by the Davisson-Germer electron experiment in 1927.

spacing a. Table 2.2 lists the fourteen Bravais lattices, their associated extinction conditions (i.e. the absent reflections), and the relationship between the lattice spacing and the diffraction plane[13].

In single-crystal experiments, the only peaks visible would be those allowed by the structure factor, and the derived selection rules. As such, it is a relatively simple matter to index the crystal. However, this procedure can be complicated by the presence of multiple phases. It is next to impossible to index the crystal when there is overlap of the Bragg peaks from the different phases.

Yet, there is still information to be gained even when the indexing cannot be accomplished. There is also information about the grain size. This is provided by the Full-Width Half-Maximum (FWHM) of the sample's Bragg peaks. The average grain size can be obtained by using a simple formula, such as the Debye-Scherrer equation,

$$\tau = \frac{k\lambda}{\sqrt{\beta_{Obs}^2 - \beta_{Si}^2}\cos\theta} \tag{2.6}$$

where τ is the average size of the coherent scattering domains (i.e. crystallites), k is a shape correction factor (for cubic shaped crystallites, $k = 0.94$), λ is the incoming radiation's wavelength, β_{Obs} is the FWHM of the Bragg peak (in radians), β_{Si} is the FWHM of a Bragg peak from a Si sample (to account for instrumental broadening; also, in radians), and θ is the Bragg angle.

A Cu Kα tube ($\lambda = 0.15406$ nm), operating at 45 kV, 40 mA was used to generate x-rays for laboratory-based diffraction. The detector was scanned between 20° and 70°, with a constant take off angle of 5°. All measurements were taken at ambient laboratory conditions. The peak parameters were determined with the CMPR program [173], and the patterns were compared with the International

[13]The various diffraction planes are defined by the Miller indices. The Miller indices denote a plan orthogonal to a direction, in the basis of reciprocal lattice vectors.

Table 2.2: The extinction conditions and relationship between the lattice spacing and the diffraction plane for the different types of crystalline lattices.

Bravais lattice	Absent Reflections	Diffraction plane-Lattice parameter Relationship
triclinic	none	$\frac{1}{d^2} = \frac{1}{V^2}(S_{11}h^2 + S_{22}k^2 + S_{33}l^2 + 2S_{12}hk + 2S_{23}kl + 2S_{13}hl)$
		V = cell volume
		$S_{11} = b^2c^2\sin^2\alpha$
		$S_{22} = a^2c^2\sin^2\beta$
		$S_{33} = a^2b^2\sin^2\gamma$
		$S_{12} = abc^2(\cos\alpha\cos\beta - \cos\gamma)$
		$S_{23} = a^2bc(\cos\beta\cos\gamma - \cos\alpha)$
		$S_{13} = abc^2(\cos\gamma\cos\alpha - \cos\beta)$
simple monoclinic	none	$\frac{1}{d^2} = \frac{1}{\sin^2\beta}(\frac{h^2}{a^2} + \frac{k^2\sin^2\beta}{b^2} + \frac{l^2}{c^2} - \frac{2hl\cos\beta}{ac})$
base-centered monoclinic	none	$\frac{1}{d^2} = \frac{1}{\sin^2\beta}(\frac{h^2}{a^2} + \frac{k^2\sin^2\beta}{b^2} + \frac{l^2}{c^2} - \frac{2hl\cos\beta}{ac})$
simple orthorhombic	none	$\frac{1}{d^2} = \frac{h^2}{a^2} + \frac{k^2}{b^2} + \frac{l^2}{c^2}$
base-centered orthorhombic	h, k, l = mixed odd or even	$\frac{1}{d^2} = \frac{h^2}{a^2} + \frac{k^2}{b^2} + \frac{l^2}{c^2}$
body-centered orthorhombic	h, k, l = mixed odd or even	$\frac{1}{d^2} = \frac{h^2}{a^2} + \frac{k^2}{b^2} + \frac{l^2}{c^2}$
face-centered orthorhombic	h, k, l = mixed odd or even	$\frac{1}{d^2} = \frac{h^2}{a^2} + \frac{k^2}{b^2} + \frac{l^2}{c^2}$
rhombohedral	none	$\frac{1}{d^2} = \frac{(h^2+k^2+l^2)\sin^2\alpha + 2(hk+kl+hl)(\cos^2\alpha - \cos\alpha}{a^2(1-3\cos^2\alpha+2\cos^2\alpha)}$
simple tetragonal	none	$\frac{1}{d^2} = \frac{h^2+k^2}{a^2} + \frac{l^2}{c^2}$
body-centered tetragonal (bct)	$h + k + l = odd$ = even	$\frac{1}{d^2} = \frac{h^2+k^2}{a^2} + \frac{l^2}{c^2}$
hexagonal close packed (hcp)	$h + 2k = 3n$, l = odd	$\frac{1}{d^2} = \frac{4}{3}\frac{h^2+hk+k^2}{a^2} + \frac{l^2}{c^2}$
simple cubic	none	$\frac{1}{d^2} = \frac{h^2+k^2+l^2}{a^2}$
body-centered cubic (bcc)	$h + k + l = odd$	$\frac{1}{d^2} = \frac{h^2+k^2+l^2}{a^2}$
face-centered cubic (fcc)	h, k, l = mixed odd or even	$\frac{1}{d^2} = \frac{h^2+k^2+l^2}{a^2}$

Center for Diffraction Data (ICDD) Powder Diffraction File (PDF) database [174]. The crystallite size was estimated with the Debye-Scherrer equation, Eqn. 2.6. A silicon standard yields $\beta_{Si} = 0.31^\circ = 0.00541$ radians.

2.3.5 Raman Spectroscopy

As noted in the previous section, Sec. 2.3.4, there are two types of scattering: elastic and inelastic. XRD is a good example of elastic scattering. Raman scattering provides a good example of inelastic scattering. In this case, the incoming photons interact with the molecular vibrations of the sample, i.e. phonons. If the photon loses energy as a result of this interaction, the outcome is labeled as Stokes Raman. If the photon gains energy, the outcome is Anti-Stokes. The energy difference between the incoming and outgoing photon corresponds to the phonon resonance of the material; it is independent of the overall photon energy. Stokes and Anti-Stokes scattering form a symmetrical spectrum centered on the photon energy.

Since phonons are quasiparticles representing lattice vibrations, their resonance is affected by different bonding environments. Thus, Raman scattering is an excellent method to elucidate the chemical bonding environment of various samples. With Raman scattering, both the nature of the bond, and the relative amounts of different bonds can be determined. A typical green laser, anti-Raman spectrum from a diamond crystal is plotted in Fig. 2.12. Note, the x-axis is in units of relative Raman shift, i.e. the spatial frequency, or wavenumber, of the scattered wave.

There are clearly two peaks in this spectrum. The main peak is from normal diamond, consisting of sp^3-bonded carbon. The second peak is from diamond growth using a precursor with a different isotope of carbon, C^{13}. Since these are both diamond peaks, the nature of the bonds are the same (sp^3-bonded). The only difference is due to the nature of the lattice's constituent atoms, i.e. C^{12} vs. C^{13}

atoms. As such, a precise picture of the chemical environment can be determined.

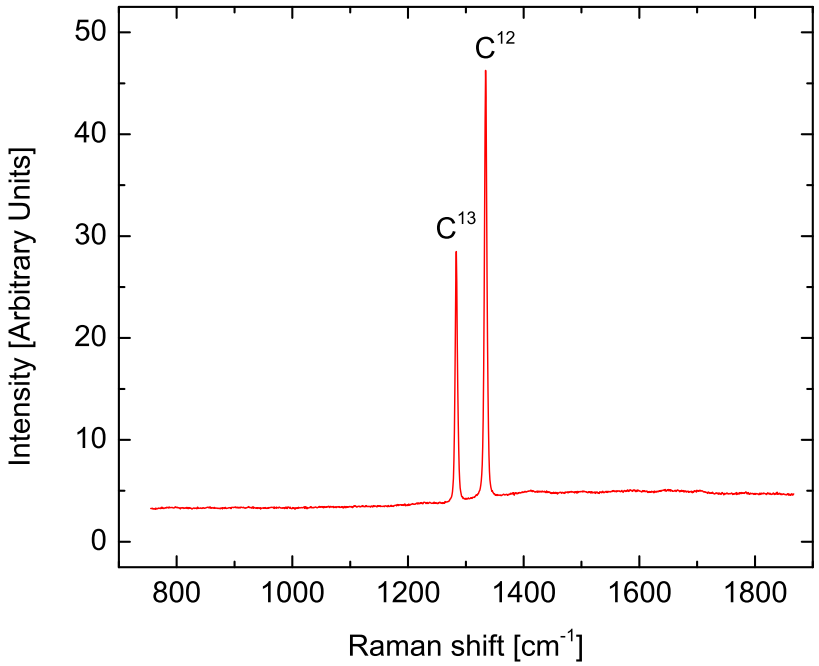

Figure 2.12: Raman spectrum from a single-crystal diamond with a coating of C^{13} diamond.

Unfortunately, not all materials exhibit a Raman effect. In order to observe a Raman signal, their needs to be deformation of the electron cloud, i.e. a change in the polarization, with respect to the vibrational modes of the sample's atoms/molecules. The intensity of the peak is directly related to the polarizability change. Therefore, most conductors do not show an appreciable Raman signal.

Anti-Stokes, Raman spectroscopy of the relevant coatings was taken with a 300 mW solid state laser (Dragon Lasers), operating at $\lambda = 532$ nm, focused thru the 100X objective of an optical microscope (Olympus) to a 10 μm spot size. The signal passes through a 1200-slit grating, centered at the 1332 cm^{-1} wavenumber; from here, it is collected and analyzed with a Dilor XY spectrometer, Fig. 2.13. Prior to the measurements, the system is cooled to -115 °C (with liquid N_2) and calibrated with the Raman lines of an argon glow-discharge plasma. All measurements were taken in ambient laboratory conditions.

Figure 2.13: This Dilor XY Raman spectrometer, located at UAB, Birmingham, AL USA, uses a 532 nm, 300 mW laser as its source, which can be focused to a 100 μm, spot size. Different neutral density filters can be used to reduce the intensity of the light irradiating the sample.

2.3.6 X-ray Photoelectron Spectroscopy

X-ray Photoelectron Spectroscopy (XPS), or Electron Spectroscopy for Chemical Analysis (ESCA), was developed in the 1960s by Siegbahn's group at the University of Uppsala, Sweden [175, 176]. With the advent of commercial UHV systems, its use became wide-spread and a standard characterization tool for surface analysis. The technique is based on the excitation of photoelectrons, from a sample, by x-rays.

When light irradiates the surface of a sample, the incident photons will interact with the atoms of the sample. Depending on the frequency of the incoming light (i.e. the energy), the electrons may absorb sufficient energy to escape from its atomic orbital, Fig. 2.14. This threshold is the binding energy of the electron, and is very specific to both the element and the atomic orbital of the electron's origin. Using a spectrometer, the kinetic energy of the emitted photoelectrons can be

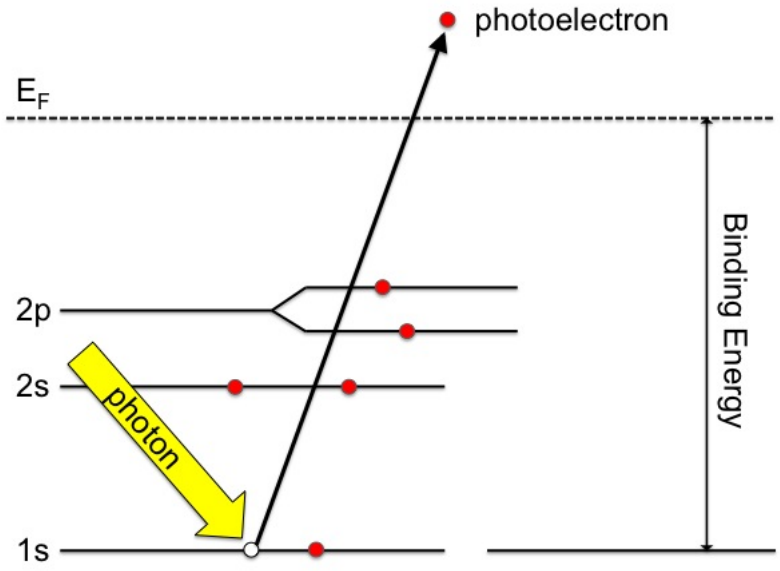

Figure 2.14: Schematic representation of the photoelectric effect.

evaluated. From this, the binding energy of the electrons can be determined by Eqn. 2.7.

$$KE = h\nu + BE + \phi_s \tag{2.7}$$

where KE is the kinetic energy of the photoelectrons, h is Planck's constant (= 6.626×10^{-34} J·s), ν is the frequency of the incoming light[14], BE is the binding energy, and ϕ_s is the spectrometer work function. With this information, the relative amounts of different elements can be accurately determined for a given sample. Additionally, any shifts in the binding energies from the values of pure elements can yield information about the bonding of elements (i.e. formation of compounds) within the sample.

However, there is a limit to photoelectron spectroscopy: mean free paths. In vacuum, the typical mean free path of photons in the x-ray range is $\sim$ 1-10 μm.

[14]For XPS, the light comes from a Mg Kα (E = $h\nu$ = 1253.6 eV), an Al Kα (E = 1486.6 eV), or a monochromatic Al Kα (E = 1486.7 eV) source. In Ultraviolet Photoelectron Spectroscopy (UPS), the source is a helium-I (E = 21.2 eV) or helium-II (E = 40.8 eV) lamp.

However, since electrons are charged particles, the mean free path of the emitted photoelectrons is only on the order of 2-3 nm[15]. As such, only the near surface region of a sample can be probed by photoelectron-based techniques, such as XPS or UPS. Photoelectrons from further down in the sample will suffer collisions (and possible reabsorption) with other atoms in the system.

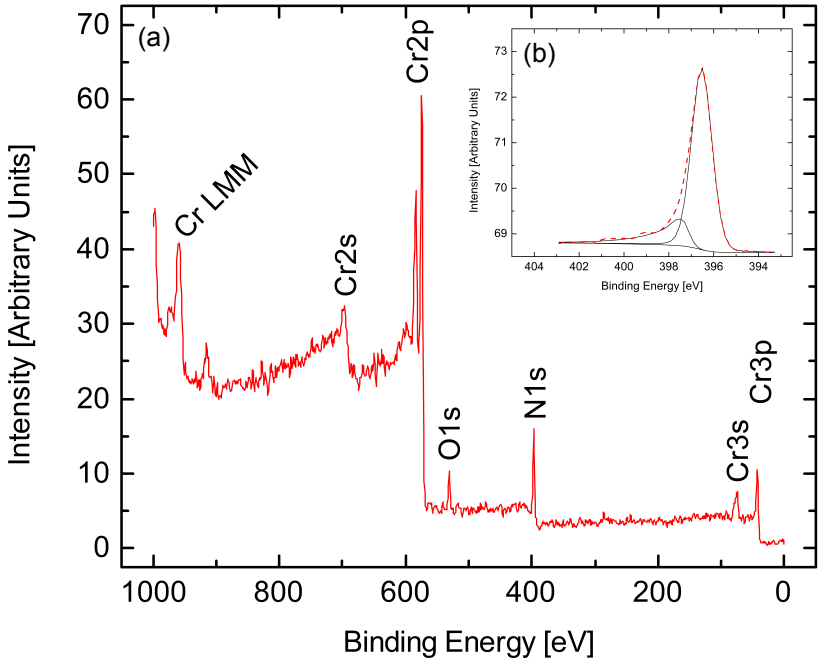

Figure 2.15: (a) Survey scan of a CrN sample, deposited by RF magnetron sputtering. (b) High-resolution scan of the N1s peak. For this high-resolution scan, solid lines are the deconvoluted peaks (identifying the relevant chemical states present), and the dashed lines are the original data. Both scans were taken after 15 minutes of sputter etching with Ar at 1 kV accelerating voltage.

Figure 2.15(a) shows an example survey of a CrN sample, deposited by magnetron sputtering. While the hemispherical analyzer and channel plate detector actually measure kinetic energy, it is standard procedure to plot intensity versus binding energy. Another quirk is plotting from high energy to low energy. Looking at the spectra, there are several distinct features. The broad peaks at high energy are Auger lines; the Auger process is explained in Sec. 2.3.2. The narrow,

[15]In UPS, the mean free path of the photoelectrons is only $\sim$ 1-2 nm. As such, this technique is better suited to measure the sample's valence band.

high-intensity peaks are the photoelectric peaks. Surveys are typically used to help determine the chemical composition of an unknown sample. This is accomplished through the following equation:

$$C_x = \frac{I_x/S_x}{\sum I_i/S_i} \tag{2.8}$$

where C_x is the atomic % of element x, I_x is the intensity of a specific photoelectric peak of element x, S_x is the atomic sensitivity factor for the specific photoelectric peak of element x[16], and the denominator is the sum of all peak intensities, corrected by the appropriate sensitivity factors. An alternative analysis would replace the peak intensity with the peak area, and suitable sensitivity factors. Going back to the spectrum in Fig. 2.15(a), Eqn. 2.8 yields 58 atomic (at.) % chromium, 31 at. % nitrogen, 4 at. % oxygen, and 6 at. % carbon within the sample.

While these quantitative results are very useful, it should be noted that there are some limits to their applicability. If there is peak overlap (for example, Mo3p and N1s), a different peak (such as the N KLL) must be used to accurately determine the atomic composition. Heterogeneous samples may not be suitable for compositional analysis with XPS. The variability within the microstructure may affect the quantitative results. Additionally, contamination layers can affect higher binding energy peaks more than low binding energy peaks, and thus skew the results.

Survey scans are useful, but they do not have the necessary resolution to determine chemical shifts. Therefore, high-resolution spectra are taken at specific binding energies to determine the peak shift, as shown n Fig. 2.15(b). Using the Multipak™, the high-resolution spectra can be deconvoluted. and information on

[16]The sensitivity factor is a spectrometer-specific correction factor to account for the x-ray flux, photoelectric process efficiency for the relevant orbitals, the spectrometer geometry, and the detector efficiency. For the PHI Versaprobe, all peaks are referenced to the F1s peak.

the chemical state of the element can be extracted[17]. For example, the spectra in Fig. 2.15(b) is the N1s spectrum of a CrN thin film on Si. The N1s elemental peak should be located at 398.1 eV [177]. Here, the observed peak is located at 396.6 eV, with a peak shape that implies multiple chemical states. Deconvoluting yields two states at 396.6 eV and 398.1 eV. By consulting the literature, the states are identified as CrN and pure N_2, respectively. The nitrogen is most likely trapped with the CrN lattice.

The ULVAC-PHI PHI-5000 Versaprobe uses an Al Kα source to produce x-rays for both sample imaging and chemical analysis. The source consists of a focused electron beam scanning across an Al anode. The resultant x-rays are feed into a quartz crystal monochromator which both removes satellite energies from the beam and focuses it upon the sample. The PHI 5000 Versaprobe can produce a focused x-ray spot with a 10 μm diameter; beam energy is only 1.25 W which requires increased acquisition time to reduce noise. This is usually reserved for imaging, as it offers the best spatial resolution[18].

For standard analysis (i.e. chemical composition and high-resolution scans of specific peaks), an x-ray spot size of 100 μm is used; beam energy is significantly higher than the 25 μm beam at 15 W. In both cases (imaging and standard analysis), emitted photoelectrons enter a high-resolution spherical capacitor energy analyzer, with a 16-channel plate detection system. Depending on the desired analysis, an Ar ion gun can provide sputter etching to clean (and/or remove) material from the sample surface. This gun is also used in the dual-beam charge neutralization system, in parallel with a low-energy electron flood gun. This will raise the working pressure of the main chamber to 2×10^{-6} Pa.

Samples are introduced into the chamber via a load-lock system. Depending

[17]The software can also perform peak shifting (to account for charging), smoothing, and other standard peak analysis functions.

[18]Images are produced from secondary photoelectrons, in a manner analogous to an SEM. This allows for the production of a spatial image with chemical information.

on the sample geometry, up to 12 samples can be placed into the load lock. The load-lock is pumped by an ULVAC GLD-136C rotary vane pump (2.7 L/s) and a Pfeiffer TMU-071 turbomolecular pump (60 L/s). These pumps bring the load-lock down from atmospheric pressure to UHV ($\sim 10^{-8}$ Pa). Once the pressure has stabilized, the samples are transferred into the main chamber via a magnetic transfer arm. The sample stage can be rotated for angle-resolved studies and has a temperature range of -120°C to 300°. The main chamber is pumped with a Gamma Vacuum TiTan 300 TV differential ion pump (240 L/s) and Titanium sublimation pump (1000 L/s) which brings the system to a base pressure of $\sim 2\times10^{-8}$ Pa. The system is pictured in Fig. 2.16.

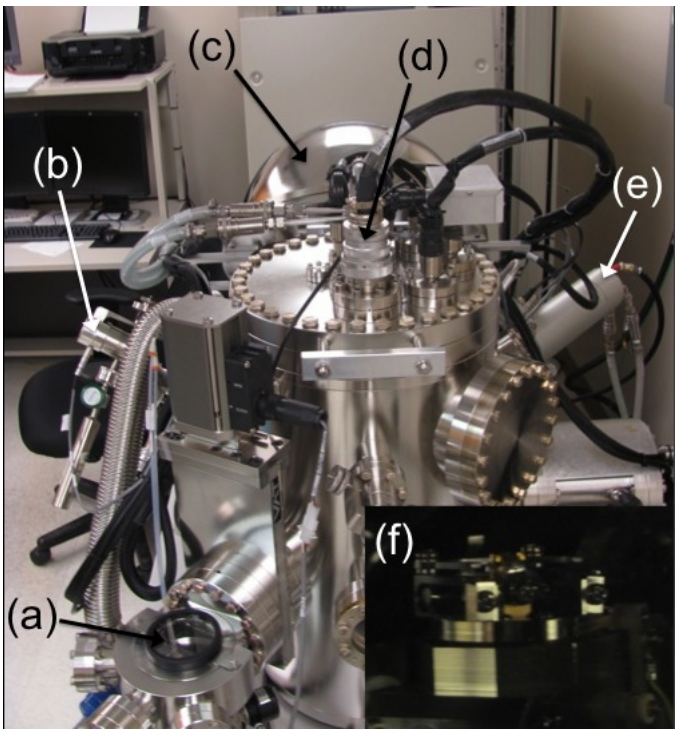

Figure 2.16: This is the PHI5000 Versaprobe, with (a) load-lock, (b) Ar ion gun, (c) hemispherical analyzer, (d) focused x-ray source, (e) dual x-ray source, and (f) variable-temperature sample stage. This system is located at UAB, Birmingham, AL USA

For this work, surveys from 0-1000 eV, and high-resolution scans of the specific peaks, were taken with the 100 μm beam from the monochromatic Al Kα

source, at a chamber pressure of 2×10^{-6} Pa (Ar). To ensure clean surfaces, samples were etched using the Ar ion gun at an accelerating voltage of 1 kV for several minutes[19]. Survey and high-resolution scans were taken both before and after etching.

2.3.7 Optical Profilometry

Stress can be measured several ways, but for coatings, the two most used are XRD or wafer curvature. With a x-ray diffractometer, the sample is rotated side-to-side (through an angle ψ). Using a minimum of 5-10 steps, the changes in the diffraction plane spacing of a high Bragg angle peak (such as the (311) peak) are plotted versus $\sin^2\psi$. If there are no significant shear stresses, the resulting plot yields a straight line. The stress is directly related to the slope of this line via,

$$\frac{d_{\phi\psi} - d_0}{d_0} = \frac{1+\nu}{E}\sigma_\phi \sin^2\psi \tag{2.9}$$

where $d_{\phi\psi}$ is the diffraction plane spacing in a direction defined by ϕ (sample rotation) and ψ (sample tilt), d_0 is the interplanar spacing for the unstressed material (this can be substituted by scanning at a second detector position), ν is the material's Poisson's ratio, E is Young's Modulus, σ_ϕ is the surface stress defined by the rotation angle ϕ, and ψ is the angle of sample tilt.

However, problems can arise from the presence of shear stresses, strong texturing, and/or weak intensities for the high Bragg angle diffraction peaks. However, wafer curvature methods can still be used, provided the substrate is thin-enough to allow flexing[20]. And while, the XRD technique can be used to look at stress through the depth of the film (up to the limit of x-ray attenuation), wafer

[19]For the viability study, this was limited to $\sim$ 5 minutes. For the low temperature study, this was increased to 30 minutes.

[20]500 μm thick Si (100) wafers are too thick, and the sample will not curve. However, 380 μm thick Si (100) wafers will deform/curve.

curvature methods only yield an average stress from the entire coating.

Wafer curvature techniques are based on the Stoney equation, developed in 1909 [178]. This geometric argument yields the average stress via the Stoney equation,

$$\sigma = -\frac{E_s h_s^2}{6(1-\nu_s)h_f}\frac{1}{R} \tag{2.10}$$

where σ is the average coating stress, E_s is the Young's Modulus of the substrate, h_s is the substrate thickness, ν_s is the substrate's Poisson's ratio, h_f is the film thickness, and R is the curvature of the coating-substrate system[21]. However, it assumes an elastic, isotropic stress states which leads to a circular shape for the wafer curvature. In the case of anisotropic stress, the wafer curvature may form an elliptical shape which requires significant modification from the original [179]. Using plate theory, Masters and Salamon [180] reported such a modified Stoney's equation in 1993,

$$\sigma = \frac{E_s}{(1-\nu_s^2)}\frac{h_s^2(a+b)}{6h_f}(1+(1+\frac{3(\nu_s+1))}{(\nu_f+1)})E_r h_r - h_r) \tag{2.11}$$

where σ is the average coating stress, E_s is the Young's Modulus of the substrate, ν_s is the substrate's Poisson's ratio, h_s is the substrate thickness, a is the semi-major axis of the elliptical wafer curvature, b is the semi-minor axis of the elliptical wafer curvature, h_f is the film thickness, ν_f is the coating's Poisson's ratio, $E_r = E_f/E_s$ is the film-to-substrate ratio of the respective Young's Moduli, and $h_r = h_f/h_s$ is the ratio of the film-to-substrate thickness.

While several methods exist for the determination of the wafer curvature, optical profilometry offers quick measurement times with ease-of-use and high

[21] Additionally, this form of the Stoney equation assumes negligible wafer curvature before the deposition.

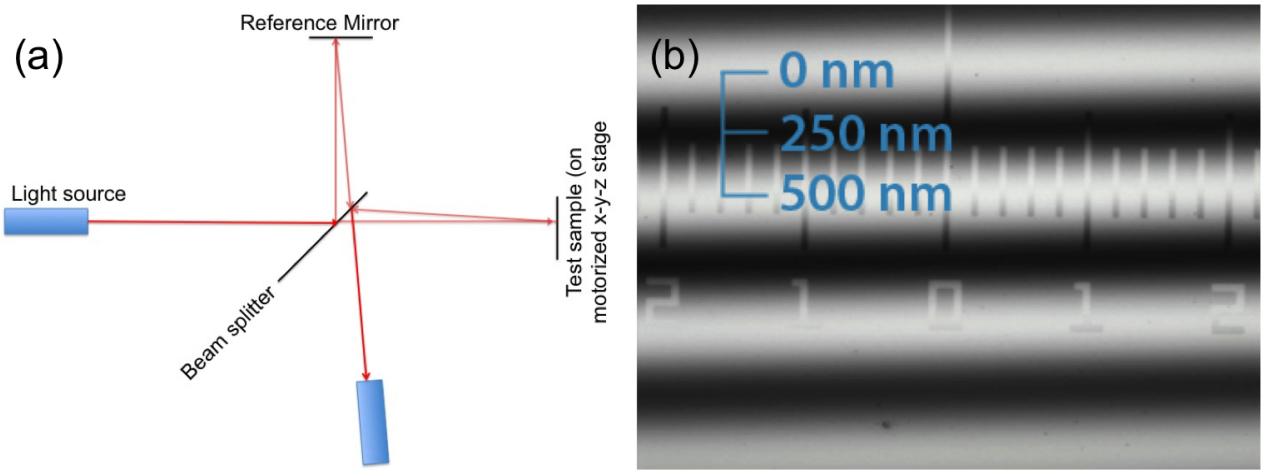

Figure 2.17: (a) A schematic diagram of an optical interferometer. (b) An image of interference fringes of a ruler, using a ZeMetrics profilometer [181].

resolution. An optical profilometer is a non-contact profilometer utilizing an interferometer to accurately determine the changes in height (and curvature) of a sample. A typical set-up is schematically diagramed in Fig. 2.17(a). A beam-splitter divides the beam, with part heading towards the sample and another part to a reference mirror. After reflection from their respective targets, the beams are recombined at the beam splitter, and directed to the detector. If the optical path of the two beams vary, an interference pattern will emerge, Fig. 2.17(b). Since the surface of the reference mirror is known, any deviations in the optical path are related to variations in the sample height, i.e. surface asperities. As a result, a 3D surface map can be imaged. This yields information on both the surface parameters and the wafer curvature (from suitable substrates).

The Veeco-Wyko NT1100 Optical Profilometer (Fig. 2.18 can be used in both Vertical Scanning Interferometry (VSI) and Phase Shift Interferometry (PSI) modes, dependent on the roughness of the sample surface. Very smooth and flat samples are scanned using PSI mode. Interference fringes are produced using a monochromatic, red light. The sample is then moved a series of steps, typically about $1/4\lambda$ in size, and a new image of the interference fringes is recorded. After

Figure 2.18: The Veeco-Wyko NT1100 optical profilometer, located at LaBoMaP, Cluny, France. This unit is mounted on an air-table to reduce the effects of vibration.

the measurement is complete, the software analyzes the images and computes the surface parameters, such as Average Roughness (R_a) and Root Mean Square Roughness (R_{RMS}). The resolution of this technique is typically sub-nanometer.

For rough and/or curved samples, VSI is the preferred methodology. This white-light technique moves the sample through a set distance. If a set of interference fringes are present in this distance, the surface morphology can be accurately determined over a much larger scale than an Atomic Force Microscopy (AFM). Combining a 1.0X Field of View (FoV) with a 5.0x objective lens yields a magnification of 5.1x, and a 920 μm x 1200 μm measurement area. The resolution over this area is sub-micron.

Additionally, individual measurements can be stitched together to cover a significantly larger portion of the sample surface. While there is no loss of resolution, there is the cost of additional time. For example, using the 1.0x FoV and

5.0X objective, an individual measurement is a little over a minute or two. However, on a 10 x 10 mm^2 sample, the number of measurements increases to $\sim$ 110 frames, and a measurement time of $\sim$ 1.5 hours.

In this study, all measurements with the optical profilometry system were taken in the VSI mode. Accurate wafer curvatures were the result of stitching the entire sample surface. Data was analyzed off-line by Gwyddion, a freeware program developed by David Nečas ad Petr Klapetek [182]. The obtained radii of curvature were inserted into Eqn. 2.11. For the few cases of circular stress states, $a = b$, and the modified version reduces to the original Stoney equation, Eqn 2.10.

2.3.8 Nanoindentation

While Hardness (H) is generally defined as a material's resistance to permanent, plastic deformation, it can take several different forms, such as scratch hardness or indentation hardness. In scratch hardness, the relevant forces are due to friction from a sharp object. A very common test for scratch hardness is the Mohs scale, which is used in mineralogy. Indentation hardness is another form. Here, the relevant worry is a compression load from a sharp object. Traditional tests include Rockwell, Brinell, Vickers, Knoop, and Nanoindentation. Rockwell tests are differential depth tests. The residual area of an indentation from a large load is compared to the residual indentation area from a small preload. There are several variants of this test (denoted Rockwell A through Rockwell G). The differences are based on different loads and indenter shapes. The most commonly used are the Rockwell B test, using a 100 kgf (0.98 kN) load through a 1/16-in diameter steel sphere, and the Rockwell C test, using a 150 kgf (1.47 kN) load through a 120° diamond cone indenter.

Brinell testing involves a spherical indenter. Typically, the indenter is made of either steel or tungsten carbide, depending on the expected hardness of the

material. Additionally, the applied load can be adjusted. As a result, it is necessary to report the exact test conditions with a Brinell number. A typical example is 1.6 HBS10/100; a 10 mm steel ball is used to apply a 100 kgf (0.98 kN) of force, and yields a result of 1.6. With Vickers testing, the test regime can move from the macroscopic to the microscopic. Here, a square-sided pyramidal-shaped, diamond tip is used to make the indentations. The total included angle for a Vickers pyramid is 136°. This was based on the ideal size of a Brinell impression, and confirmed experimentally. The applied loads are typically $\sim$ 100 kgf (0.98 kN), or less. When reporting HV, the load is typically specified; for example, HV30 implies a Vickers test with a load of 30 kgf (0.29 kN). Conversion from HV to SI units requires multiplication by a factor of 9.8×10^6. Knoop testing is very similar to the Vickers test. The key difference is the shape of the indenter head. With the Knoop test, the indenter tip is an elongated pyramid, with a typical length-to-width ratio of 7:1. This results in very shallow indentations, which are particularly well-suited for brittle materials.

Finally, nanoindentation, also known as instrumented indentation. This technique uses a variety of small tips (such as Knoop, Vickers, spherical, conical, cube-corner, or Berkovich) with very low applied loads. The resulting indentation area tends to be only a few square microns. As a result, direct observation of the indentation is difficult; an AFM or SEM may be needed. Rather than resorting to time-consuming, and cumbersome techniques, an instrumented indentation test records the penetration depth as the load is applied. This load-displacement curve forms the basis for further analysis; an example is shown in Fig. 2.19. It is interesting to note the hysteresis of the load-displacement curve, i.e. the difference between the loading (increasing load) and unloading (decreasing load)parts of the curve. This is indicative of a mixed deformation process; it is not fully elastic nor fully inelastic, but a little of both. If fully elastic, there would be no gap between

the two curves. Admittedly, the gap is small[22] and it is reasonable to deduce a mainly elastic deformation process.

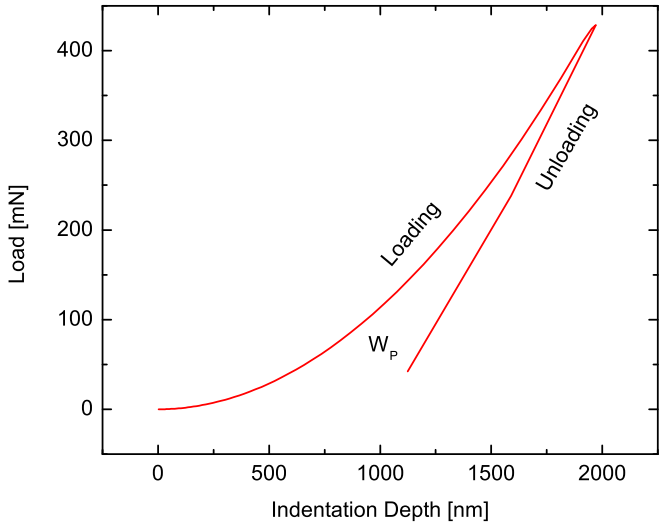

Figure 2.19: A typical load-displacement curve from the fused silica calibration standard. "Loading" indicates the region of increasing load. "Unloading" is the region of decreasing load. The hysteresis between the two regions is "W_P," the plastic work of indentation.

The method developed by Oliver and Pharr [64] is the most common analysis method for calculating the mechanical properties of the system. However, before proceeding to the calculations, the true indentation depth should be defined. The total penetration depth is a combination of the plastic, or contact, depth and the elastic, or flexure, depth,

$$h = h_e + h_c = \epsilon \frac{F}{S} + h_c \tag{2.12}$$

where h is the total indentation depth, h_e is the elastic indentation depth, ϵ is an indenter-specific constant, F is the max load, S is the slope of the unloading curve near the maximum load[23], and h_c is the plastic indentation depth.

[22]The area enclosed by the unloading and loading curves is the plastic work of indentation.
[23]This is the stiffness, $S = \frac{dP}{dh}$.

Using Oliver and Pharr, the hardness is calculated by

$$H = \frac{F_{max}}{A_p} \tag{2.13}$$

where F_{max} is the maximum applied load and A_p is the projected area of the indentation. The applied area will depend on the type of indenter, and its condition. If there is significant blunting, a polynomial form of the projected area is recommended,

$$A_p = C_0 h_c^2 + C_1 h_c + C_2 h_c^{1/2} + \ldots + C_8 h_c^{1/128} \tag{2.14}$$

where A_p is the projected area, h_c is the contact depth, and $C_0 \rightarrow C_8$ are constants. Values of C_0 are related to the geometry of the indenter, and are summarized in Table 2.3. The remaining constants are empirically derived values determined during instrument calibration.

Table 2.3: Geometrically dependent values of the constant C_0.

Indenter Geometry	Semi-Angle, θ	C_0	ϵ	β
Spherical	N/A	$2\pi R/h_c$	0.75	1
Berkovich	65.3°	$3\sqrt{3}\tan^2\theta$	0.75	1.034
Vickers	68°	$4\tan^2\theta$	0.75	1.012
Knoop	θ_1=86.25°, θ_2=65°	$2tan\theta_1 tan\theta_2$	0.75	1.012
Cube-corner	35.26°	$3\sqrt{3}\tan^2\theta$	0.75	1.034
Cone	α°	$\pi\tan^2\alpha$	0.72	1

The initial slope of the unloading curve yields the Young's Modulus (E) by a modified form of Sneddon's flat punch equation,

$$m = \gamma\beta\frac{2}{\sqrt{\pi}}E_r\sqrt{A_p} \tag{2.15}$$

where m is the initial slope of the unloading curve in the vicinity of the maximum

applied load, γ is a correction factor introduced to account for deviations from the ideal behavior predicted by Sneddon, β is a geometric correction factor which accounts for the lack of axial symmetry for different indenter tips (values for different tips are listed in Table 2.3), E_r is the reduced modulus, and A_p is the projected area (from Eqn. 2.14). The reduced modulus is calculated from,

$$\frac{1}{E_r} = \frac{1-\nu_0^2}{E_0} + \frac{1-\nu_1^2}{E_1} \tag{2.16}$$

where E_r is the reduced Young's Modulus (E), E_0 is for the test material, ν_0 is the Poisson's ratio for the test material, E_1 is the Young's modulus of the indenter, and ν_1 is the Poisson's ratio of the indenter. For many materials, Poisson's ratio is $\sim$ 0.25. As a result, the lack of an independent method to accurately determine the Poisson's ratio will not dramatically hurt the derived mechanical properties.

In other hardness testing methods, the test results yield a single number. However, with nanoindentation, an additional option can yield the mechanical properties throughout the entire penetration depth. Constant Stiffness Mode (CSM) applies a small oscillatory force to the applied load during the test. This gives an accurate measurement of the slope of the load-displacement curve, i.e. the stiffness constant, throughout the entire measurement. Therefore, the Oliver-Pharr equations for H and E do not need any modification.

The NanoIndenter XP (see Fig. 2.20) uses an inductive force generation system which provides a wide range of applied loads to the test materials. The displacement is measured by means of a differential capacitive system. A set of parallel-plate capacitors form the displacement sensor. The first capacitor has fixed plates (i.e. this is the reference capacitors). The second capacitor can move one of its plates. Therefore, as the load is applied, the capacitance of the second capacitor will change, due to the movement of the plate. Comparing this to the reference

Figure 2.20: The NanoIndenter XP by MTS, located at UAB, Birmingham, AL USA.

capacitor, a very accurate displacement can be determined. Samples are mounted below the indenter head, and attached to the platen by adhesive. Epoxies are typically too compliant, but carbon paint and crystal bond are good choices.

For the study of CrN-WC coatings, a Berkovich indenter head was used. The maximum indentation depth was 500 nm. To avoid problems with thermal drift and creep effects, a hold time of 10 s at maximum load, and 50 s at 10 % of maximum (during unloading) were selected. Measurements were analyzed with proprietary software (TestWorks 4^{TM}). Additionally, substrate effects were avoided by evaluating the Hardness (H) and Young's Modulus (E) at only 5 % relative indentation depth[24] [183].

2.3.9 Scratch testing

As mentioned in the previous section, Sec. 2.3.8, nanoindentation is only one method to determine the mechanical properties of different materials. Another method is scratch testing. Here, the Scratch Hardness (H_s) of the material is

[24]The indentation depth is normalized to the coating thickness.

determined by dragging a sharp-tipped stylus across a pre-determined distance, with a progressive applied load. The result is a track which can provide several bits of information. For example, the width of the track is directly related to H_s of the coating [184, 185],

$$H_s = \frac{8F_N}{\pi b^2} \tag{2.17}$$

where H_s is the Scratch Hardness, F_N is the applied normal force, and b is the track width.

Another parameter is an estimate of the strength of the coating-substrate interface. Scratch testing can reveal several critical loads which are typically used as a measure of coating adhesion. It is not a direct measure of coating adhesion, but it does offer an insight of the coating adhesion. The first (L_{C1}) is the regime of conformal, or tensile cracking, within a fully adherent coating. The second critical load (L_{C2}) denotes more significant damage to the coating (such as the beginning of spalling); with the third critical load (L_{C3}), there is little evidence of a complete coating. Figure 2.21 shows a typical test on a Cr-WC coating, deposited on XC100 (AISI 1095) steel. The scratch moves from left to right, with insets showing the three critical loads for this coating, with a depth profile of the scar at the first critical coating. The depth of the scar is clearly deeper than the original coating thickness. However, since there is no obvious delamination, it can be assumed that the coating has been pressed into the soft steel substrate. Continuing around, the second and third optical micrographs show the second and third critical loads, respectively.

For this study, the critical loads and the scratch hardness were evaluated on a Tribotechnic Millenium 100. This apparatus can apply a maximum load of 100 N, with 0.05 N resolution. The maximum scan distance is 30 mm. Five 5 mm scratches

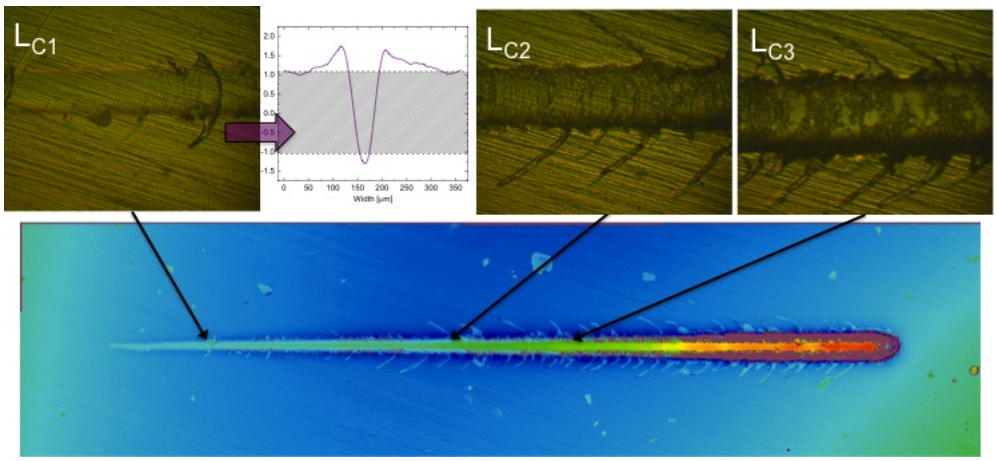

Figure 2.21: A 5 mm scratch produced by progressive loading of 30 N on a Cr-WC coating on XC100 (AISI 1095) steel. Following the same path (from left to right) as the track, the first inset is an optical micrograph of the track at the first critical load, L_{C1}. Next to this image is a profile of the scratch scar. The shaded area is the coating thickness. This is followed by optical micrographs of the second critical load, L_{C2}, and the third critical load, L_{C3}.

were created across the film surface by a Rockwell C, diamond stylus (with tip radius of 200 μm), moving at 5 mm/min. The applied load was progressively increased from 0 N to 30 N within the length of the scratch. During the measurement, the normal force, transverse force, acoustic emission, and a video of the experiment are all recorded for subsequent data analysis.

2.3.10 Corrosion

In many cases, protective coatings operate in less than ideal conditions. As a result, the coatings may be pullling double-duty as a hard coating for wear resistance, and a corrosion-resistant coating. However, successful corrosion protection requires dense, pinhole-free coatings. Unfortunately, coating porosity is not a straightforward measurement. There are typically three methods: physical examination using microscopy, chemical methods with different reagents, and electrochemical methods. Physical examination can be time-consuming and expensive. In addition, it requires a highly trained technician, and there is still no

guarantee for successful elucidation of the coating porosity. Chemical methods are an improvement, but the reagents can be dangerous. Electrochemical methods measure a relatively large area (compared to microscopy), are easy to use (sometimes hard to analyze), and are relatively safe (compared to many chemical reagents).

Samples from the low-temperature and the high-temperature deposition were immersed in a 30g/L aerated NaCl solution at room temperature. A classical three-electrode cell was used: the working electrode is the material to be tested (exposed area of 1.1 cm^2), a reference electrode of Saturated Calomel Electrode (SCE) and a graphite counter-electrode. To ensure a steady-state before the start of any other experiments, the electrochemical potential was measured for 30 minutes. Once complete a potentiodynamic curve was recorded at a 10 mV/min scan rate. This was devoted to the determination of the $i(E)$ curve. Porosity is then calculated by the ratio of $i_{Corr-coated}/i_{Corr-bare}$, at the mixed corrosion potential [186].

Summary

Below is a table which includes all the experimental techniques used during this study, and the investigated sample properties.

Table 2.4: Experimental techniques and the studied sample properties.

Technique	Result
Radio-Frequency (RF) magnetron sputtering	CrN-WC coating deposition
Microwave Plasma Chemical Vapor Deposition (MPCVD)	nanocrystalline-Diamond (nc-D) coating deposition
Atomic Force Microscopy (AFM)	Surface roughness
Scanning Electron Microscope (SEM)	Surface morphology
	Coating microstructure
	Coating thickness
Energy Dispersive X-ray Spectroscopy (EDS)	Chemical composition
X-ray Diffraction (XRD)	Structural composition
Raman spectroscopy	Chemical identification
X-ray Photoelectron Spectroscopy (XPS)	Chemical composition and bonding structure
Optical profilometry	Stress
	Scratch morphology
Nanoindentation	Mechanical properties
Scratch testing	Scratch hardness
	Critical loads (adhesion)
Corrosion	Porosity

CHAPTER III

RESULTS AND DISCUSSION

3.1 Viability of the CrN-WC System

3.1.1 Feasibility and Properties of CrN-WC Coatings

To investigate the viability of the CrN-WC system, four samples of are deposited on 10 x 10 mm^2 pieces of Si and 5 mm diameter discs of commercially-pure titanium. The deposition conditions are summarized in Table 3.1. No external heating was provided, and the substrate temperature was less than 200 °C.

Table 3.1: Deposition conditions for the viability study of CrN-WC coatings. For improved adhesion, a 170 nm Cr coating is deposited onto the bare substrates.

Composition	V, Cr [V]	V, WC [V]	Ar/N	p [Pa]	t [min]
WC	NA	-900	100/0	0.4	187
Cr-WC	-500	-500	100/0	0.4	187
WCN	NA	-500	60/40	0.4	187
CrN-WC	-500	-500	60/40	0.4	187

Figure 3.1(a) shows the XRD pattern for the WC sample on Si. By comparing this pattern with prior work [187] and the ICDD PDF database [174], the structure has been determined as the carbon deficient, cubic WC_{1-x} phase, with an average crystallite size of approximately 3 nm from Debye-Scherrer analysis, see Eqn. 2.6. After removing the surface contamination, XPS, shown in Fig. 3.2(a), yields only two carbide states in C1s core level at 283.5 eV and 282.4 eV; the film may contain some amount of W_2C, as shown by the band splitting in Fig. 3.3(a).

Unfortunately, the WC coating is partially delaminated from the Si substrates, as shown in Fig. 3.4, and Ti substrates (not shown). However, surface

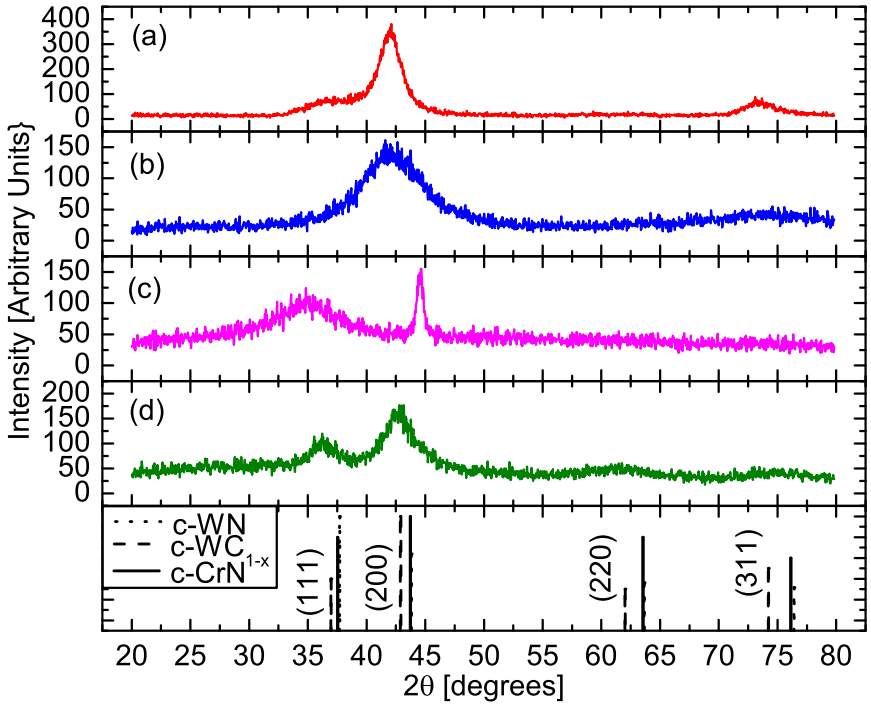

Figure 3.1: X-ray diffractograms of samples (a) WC, (b) Cr-WC, (c) WCN, and (d) CrN-WC deposited onto Si. Note, there is a 170 nm Cr buffer layer underneath the top coating.

topography and mechanical testing was still possible with the remaining adherent fragments of the WC film. These adherent areas were very smooth, with an R_{RMS} of approximately 1.06 nm (as measured by AFM in a 5×5 μm^2 area). In addition, the mechanical properties are quite promising. Nanoindentation tests yielded a E of 537 GPa, and a high H of 47 GPa[1]. As such, the H^3/E^2 is 0.37; this is consistent with coatings of high fracture toughness, as outlined in Tables 1.1 and 1.2. In other words, if this film had remained adherent, it would have shown very good fracture toughness.

The analysis of Cr-WC coatings is not quite as straight-forward as the binary WC material. This is partly due to the lack of accepted data files within the ICDD

[1]Using Bückle's rule [188], the hardness and modulus are evaluated at 5 % film depth. However, the partial delamination of the WC film prohibits an accurate determination of the film thickness. As such, for H and E, the film thickness is estimated based on deposition time and rate. This yields a thickness of 1.34 μm

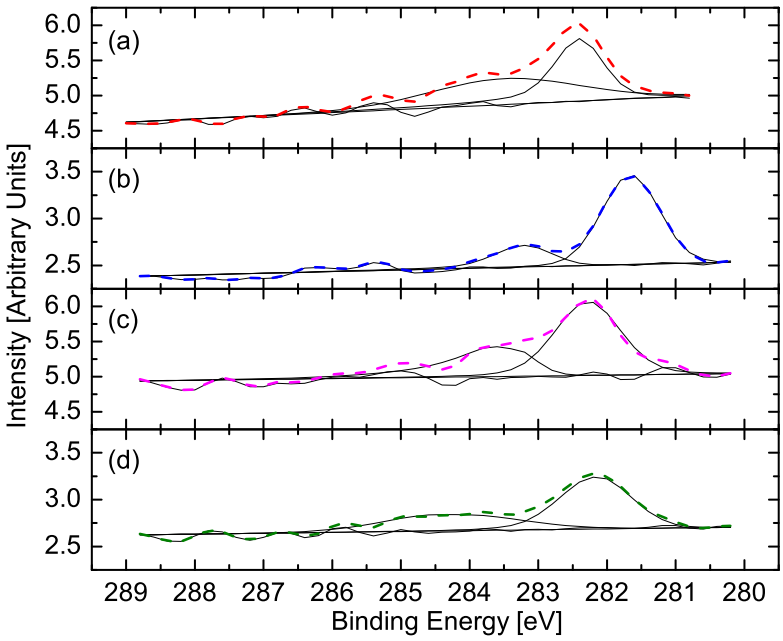

Figure 3.2: C1s spectra from the (a) WC, (b) Cr-WC, (c) WCN, and (d) CrN-WC samples. The solid lines are the deconvoluted peaks used for fitting the original data (dashed lines).

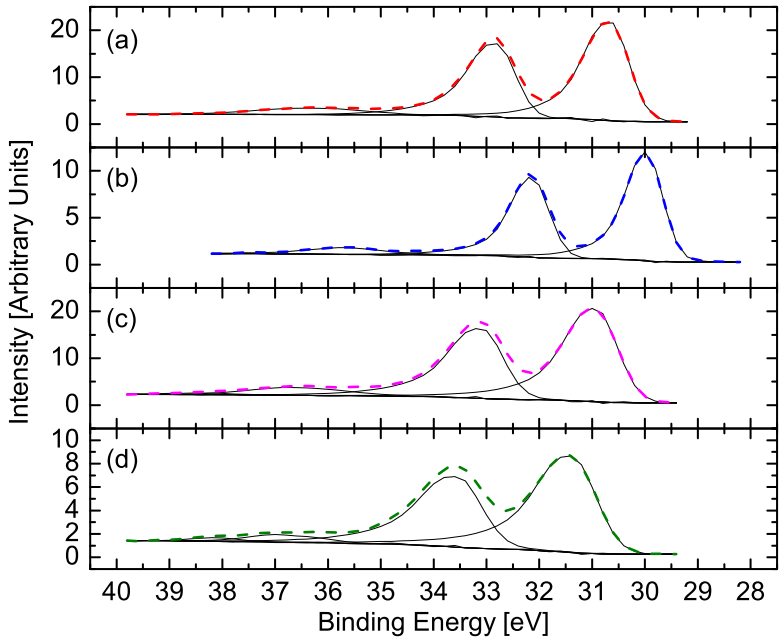

Figure 3.3: W4f spectra from the (a) WC, (b) Cr-WC, (c) WCN, and (d) CrN-WC samples. The solid lines are the deconvoluted peaks used for fitting the original data (dashed lines).

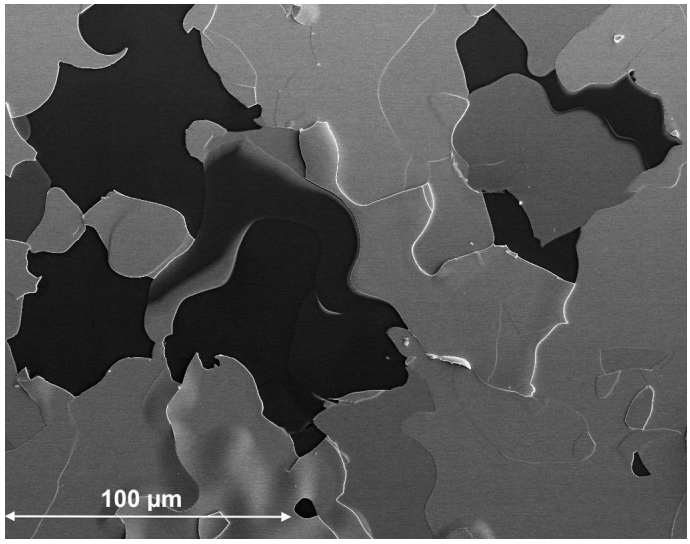

Figure 3.4: HR-SEM image of the partially delaminated surface of a WC sample on Si.

database, and the limited literature on these coatings [153, 155]. As shown in Fig. 3.1(b), there is a single broad peak centered at $2\theta = 42.2°$. If a single phase is assumed, the average crystallite size is 1.7 nm. However, the shape and breadth of this peak suggests the possible overlap of WC_{1-x} and CrC phases. While most likely cubic, the crystallographic structure of the component phases cannot be verified.

Using XPS, the chemical bonding structure can be resolved. As shown in Fig. 3.2(b), the C1s spectrum is split in two states at 283.2 eV and 281.7 eV, which correspond to bound carbide states. Figure 3.3(b) shows the W4f peaks, with only one state. Finally, Fig. 3.5(a) shows that the $Cr2p^{1/2}$ and $Cr2p^{3/2}$ peaks are located at 581.9 eV and 572.5 eV, respectively. From the NIST XPS Database [189], this is most likely a Cr_7C_3 phase. Thus, the Cr-WC system most likely consists of WC_{1-x} and Cr_7C_3 phases, with some small amount of W-O bonding[2].

While the Cr-WC coating is 2 μm thick, smooth, and adherent, the measured H and E are only 18.7 GPa and 269 GPa, respectively; H^3/E^2 is 0.09. These values are significantly lower than the prior WC_{1-x} film and the superhard, supertough

[2]As determined from the W4d and O1s spectra which are not shown.

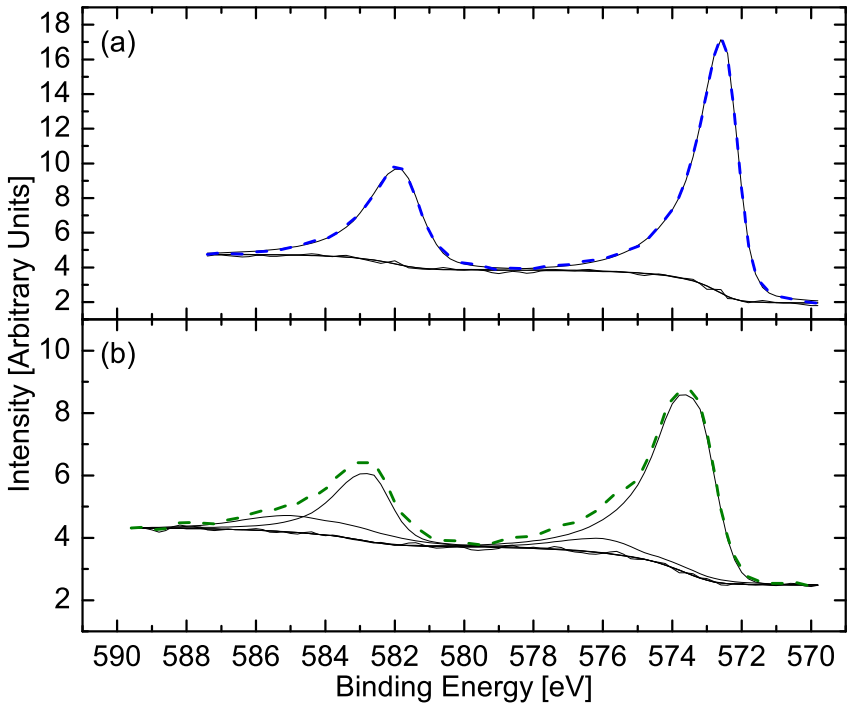

Figure 3.5: Cr2p spectra from the (a) Cr-WC and (b) CrN-WC samples. The solid lines are the deconvoluted peaks used for fitting the original data (dashed lines).

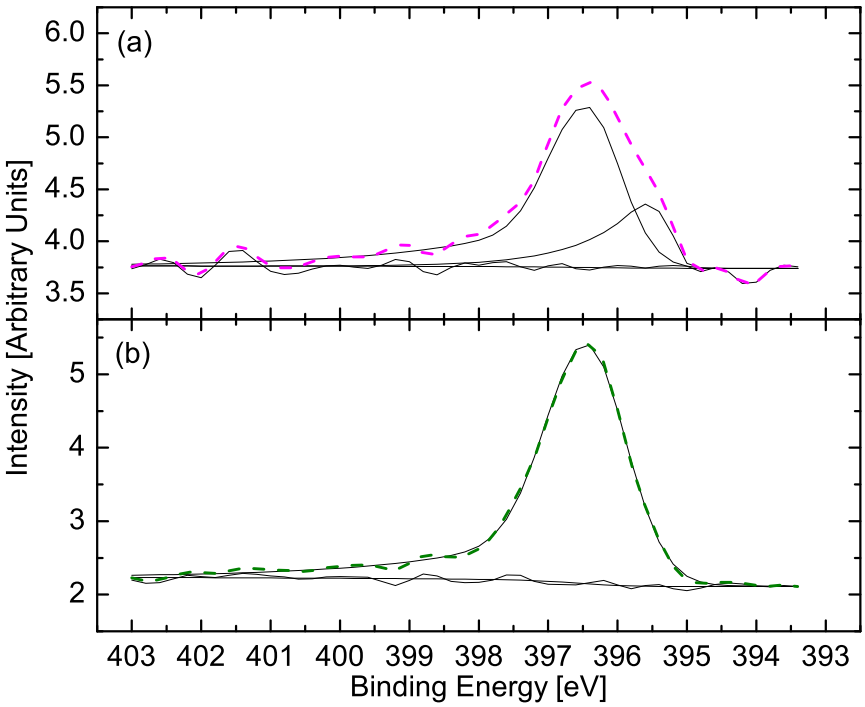

Figure 3.6: N1s spectra from the (a) WCN and (b) CrN-WC samples. The solid lines are the deconvoluted peaks used for fitting the original data (dashed lines).

films of Tables 1.1, 1.2, and 1.3. The average H $\sim$ 18 GPa and E $\sim$ 374 GPa [190–193] of Cr_7C_3, could lead to a definitive drop of the mechanical properties. Stress relaxation, induced by the introduction of a second, more ductile phase, may also have a significant impact on the hardness of the Cr-WC system.

The ternary WCN coatings were found to be highly adherent, but were the thinnest. The reactive gas (N_2) significantly reduces the deposition rate, resulting in a film of only 0.9 μm. XRD pattern of this material in Fig. 3.1(c) shows a small diffraction peak at 44.6° from the Cr buffer layer. The WCN phase is characterized by a single broad peak at 34.9°. The FWHM is 6.1° and rather symmetric, and using the Debye-Scherrer equation, the crystallite size is estimated at 1.6 nm. However, while the symmetry of the peak implies a single phase, the broadness of this peak may imply the overlap of phases with locally varied composition and the presence of partially amorphous phase. In addition, film stress tends to broaden peaks. This analysis is somewhat consistent with WCN formation using a much lower N_2 partial pressure during sputtering [194].

From the fitting of the high resolution XPS spectra (Fig. 3.2(c)), the C1s have three possible states at 284.9 eV, 283.6 eV, and 282.3 eV. The state at 284.9 eV is consistent with sp^2-bonded C within the film. The other carbon states at 283.6 eV and 282.3 eV are both carbides. Raman spectroscopy (not shown) confirms the presence of sp^2-bonded carbon. Figure 3.6(a) shows the nitrogen states, 396.5 eV and 395.4 eV, are bound in nitrides. W4d yields two states (not shown), and the W4f only one state (Fig. 3.3(c)). In addition, this film contains approximately 1 at. % of O1s (not shown). From these results, the film is primarily WCN, but contains small amounts of WO_x and sp^2-bonded C.

The nearly amorphous structure of the WCN coating can be responsible for the very low surface roughness of R_{RMS} = 1.28 nm. Yet, the hardness and Young's modulus are only 12.1 GPa and 246 GPa, respectively; this results in an H^3/E^2 =

0.03. While there are several possible culprits for these low mechanical properties, the two leading candidates are low film thickness [195] and the presence of free graphitic carbon.

The composite coating prepared by the simultaneous sputtering of WC and Cr targets in an argon-nitrogen atmosphere was quite different from the materials discussed above. EDS compositional analysis has determined the Cr:W ratio is 1.94:1. With respect to XPS, both the W4f (Fig. 3.3(d)) and N1s (Fig. 3.6(b)), are in one state. Fig. 3.2(d) is the C1s, with two states located at 284.3 eV and 282.1 eV. Fig. 3.5(b) shows the Cr2p peaks, deconvoluted into two distinct states. The peak locations for W-N and Cr-N are very similar. However, due to thermodynamic considerations, it is more likely for the nitrogen to bind with Cr. Therefore, based on the XPS data, this compound may be comprised primarily of two distinct phases: WC and CrN. This conclusion is partially supported by the XRD pattern in Fig. 3.1(d), where the peaks from CrN and WC_{1-x} phases are close and may overlap. However, regardless of this overlap, the mean grain size is estimated 7-8 nm. As such, the CrN-WC coating is probably a nanocomposite with two crystalline phases.

The formation of a nanocrystalline composite material can be responsible for the improved mechanical and other characteristics of the CrN-WC coatings when compared with other samples. These coatings are adherent and very smooth with R_{RMS} = 1.65 nm, as shown in the AFM image of Fig. 3.7. The hardness and Young's modulus of CrN-WC were determined as 29.6 GPa and 316 GPa, respectively. H^3/E^2 is 0.26; this is similar to coatings with high fracture toughness, as outlined in Tables 1.1, 1.2, and 1.3.

3.1.2 Nanocrystalline Diamond Deposition on CrN-WC

While there are some interesting possibilities within coatings based on CrN-WC, this is only part of the overall picture. One targeted application for these

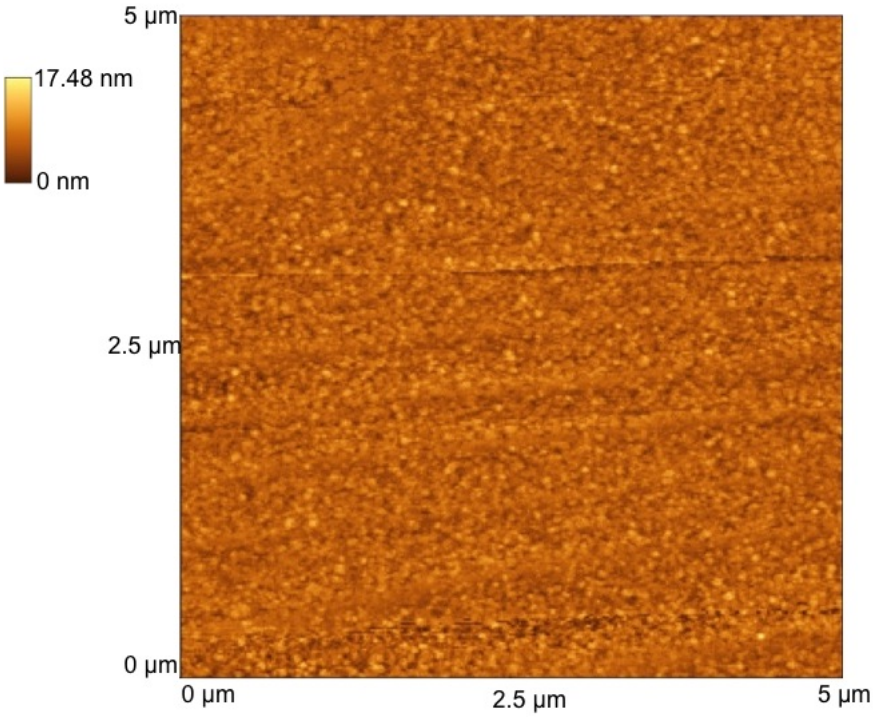

Figure 3.7: AFM micrograph of the CrN-WC sample deposited on Si.

coatings is the use as underlayers for successful nc-D deposition. Each of the samples above, on Si substrates, were used in the deposition of nc-D by MPCVD. The system parameters are listed in Table 2.1. Film thickness should be 2.5 μm, based on prior experiences [196–198].

In these preliminary experiments, it has been found that both the WCN and CrN-WC showed nc-D layer growth without additional seeding. The binary WC and ternary CrWC samples delaminated during the nc-D deposition. Figure 3.8 is the XRD patterns for both the (a) WCN and (b) CrN-WC films after nc-D deposition. In both films, there is a small peak at 44.4° which corresponds to (111) peak of diamond. The size of the diamond crystallites was estimated about 9 nm in both films. However, as can be seen in Fig. 3.8(a), there is a phase transition from a nearly amorphous WCN film to a polycrystalline composite. Due to annealing, and the reducing effects of hydrogen during the nc-D deposition, the ternary layer

decomposes into WC_{1-x} (with a peak at 41.8°), W_2C (with peaks at 36° and 39.4°), and pure W (with a peak at 40.4°) phases. The CrN-WC film (Fig. 3.8(b)) exhibits significantly different behavior. Based on the XRD data, it has been proposed that this coatings decomposes into W_2C (peak at 36°), WC_{1-x} (peak at 41.3°), CrN (peaks at 37.8° and 43.4°), and possibly CrC (peak at 44.9°) nanocrystalline phases without significant changes in the surface morphology and adhesion.

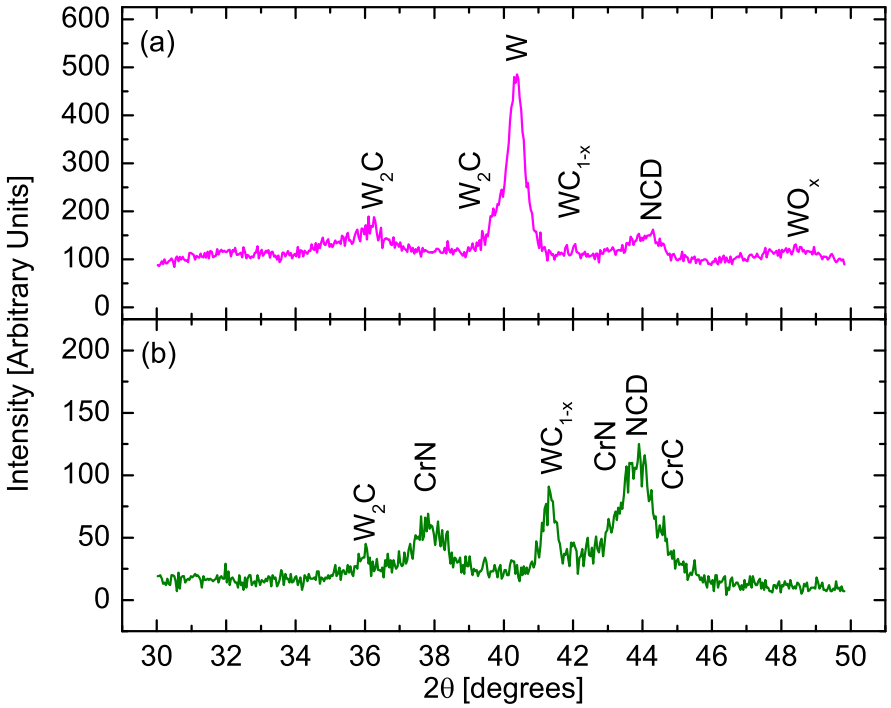

Figure 3.8: X-ray diffractogram of nc-D film on (a) WCN and (b) CrN-WC coatings, deposited on Si.

While XRD clearly shows the development of a diamond film, the nature of this carbon coating cannot be resolved without Raman spectroscopy. Using a 300 mW, 532 nm laser, the Raman spectra for both films clearly shows the proto-typical nc-D line-shapes. For the ternary WCN (Fig. 3.9(a)) and quaternary CrN-WC (Fig. 3.9(b)) films, deposited on both Si and Ti, the nc-D layers demonstrated the same Raman spectra with distinct peaks at 1135 cm^{-1}, 1331 cm^{-1}, 1358 cm^{-1}, 1471 cm^{-1}, and 1536 cm^{-1}. The peak at 1331 cm^{-1} is due to diamond. The peaks at

1135 cm^{-1} and 1471 cm−1 are typically ascribed to polyacetylene chain fragments [199, 200]. The peaks at 1358 cm^{-1} and 1536 cm^{-1} are the D- and G-lines for small, distorted sp^2-bonded cluster [201]. The lack of significant line-shifts may correspond to low internal stress within the nanocrystalline-Diamond layer.

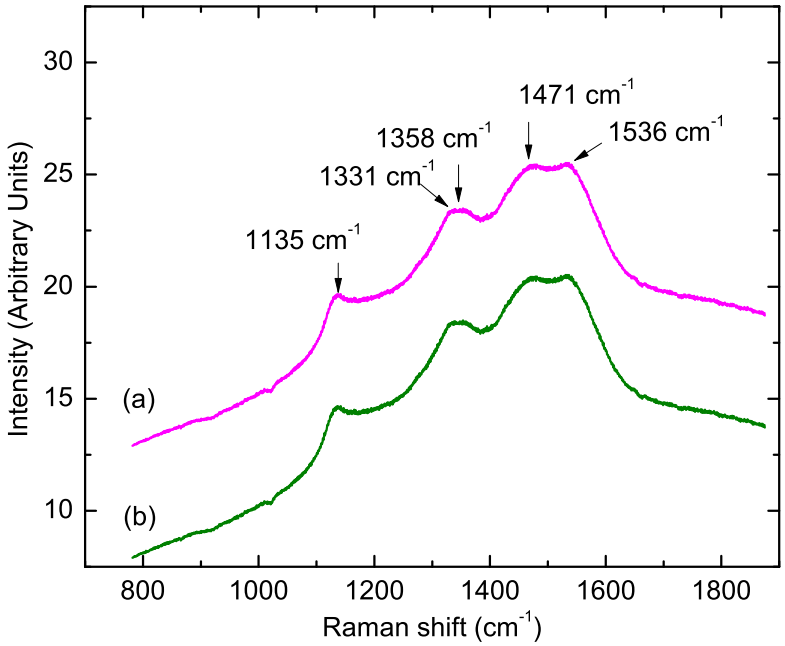

Figure 3.9: Raman spectra from the nc-D coating with (a) WCN and (b) CrN-WC samples acting as a base layer. The substrates are commercially-pure Ti discs.

However, the nc-D does not form a smooth layer as seen in Fig. 3.10. Prior to deposition, the R_{RMS} of the WCN and CrN-WC coatings were 1.28 nm and 1.65 nm, respectively. After deposition, the R_{RMS} of the WCN and CrN-WC based coatings was over 30 nm. Typically, nc-D coatings are much smoother than this. However, these results may be due to enhanced secondary nucleation during the growth process. Since this occurs on both ternary and quaternary underlayers, the problem may lie within the nc-D deposition process rather than the coating parameters[3].

[3]Further investigation of the growth parameters and the MPCVD apparatus confirms there was a problem with feed gas flow stability. This instability had a direct impact on the smoothness of the nc-D coatings.

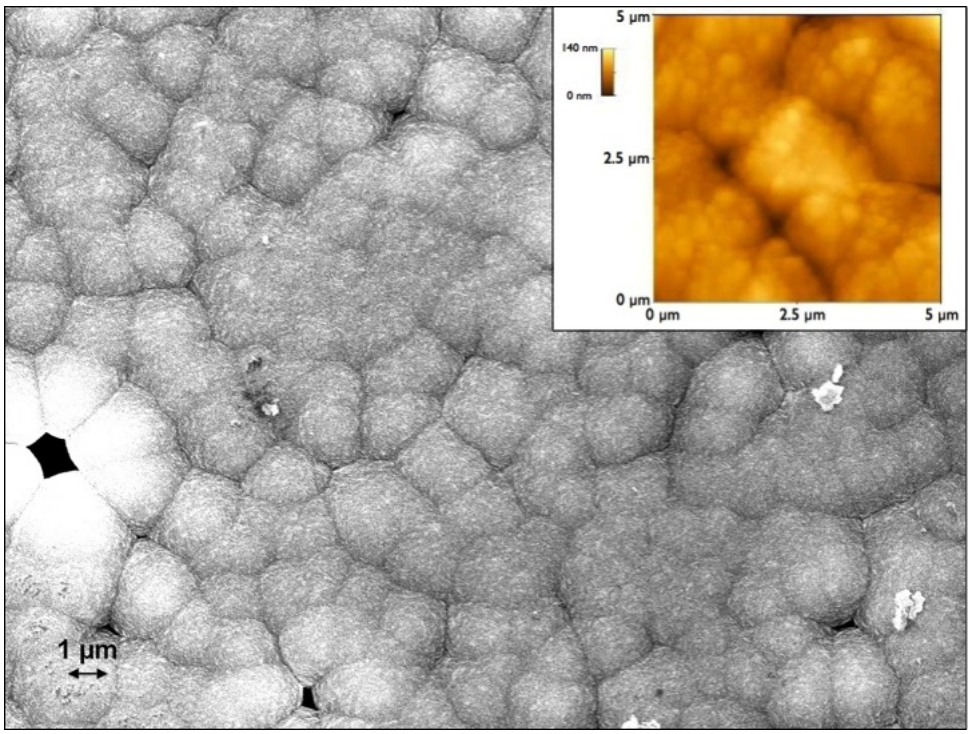

Figure 3.10: HR-SEM image of the CrN-WC sample after nc-D deposition. The inset shows an 5×5 μm^2 AFM micrograph.

3.1.3 Summary of the Viability Study

Using RF magnetron sputtering, Cr-WC-N based coatings were successfully deposited onto both Si and Ti substrates.

- Binary WC coatings have high hardness (H $\sim$ 47 GPa), despite the small crystallite size ($\sim$ 3 nm). This may be due to the presence of both WC_{1-x} and W_2C phases. The coatings were very smooth, with an $R_{RMS} \sim$ 1.1 nm. Still, the films partially delaminated from both the Si and Ti substrates.

- Introducing nitrogen into the working gas significantly reduced the deposition rate of WC. The end result is a WCN coating of only 0.9 μm. Chemical and structural characterization lead to a primarily WCN composition, with small amounts of metal oxide and free carbon. The combination of low thickness and multiple phases in a nearly amorphous structure may explain the

measured mechanical properties (H $\sim$ 12 GPa; E $\sim$ 246 GPa).

- Ternary Cr-WC films also show high hardness (H $\sim$ 19 GPa), with good adhesion. This coating probably consists of WC_{1-x} and Cr_7C_3 phases.

- CrN-WC coatings showed a much higher hardness (H $\sim$ 30 GPa). This may be due to the formation of a nanocomposite of CrN and WC, as supported by XPS and XRD. However, it is unclear if the nanocomposite is formed by the combination of multiple nanocrystalline phases, or the mixture of nanocrystalline and amorphous phases.

While the mechanical results are promising, neither the WC nor the Cr-WC coating survived nc-D deposition via MPCVD. However, the WCN coatings were still adherent after plasma treatment, and did support nc-D growth via MPCVD. The surface roughness of the nc-D coatings were significantly higher than desired. This is probably due to secondary nucleation of the nc-D coating, which may be due to a problem in the feed-gas during deposition.

The CrN-WC also survived plasma treatment and nanocrystalline diamond films were successfully deposited. The nc-D coatings on CrN-WC were deposited in the same run as the nc-D films on WCN. As such, the nc-D coatings on CrN-WC also showed significant secondary nucleation which significantly increased the surface roughness.

3.2 Variation of Deposition Conditions of CrN-WC Films at Low Deposition Temperature

With the success of the viability study, further investigation of the relationship between the deposition conditions and the coating properties was undertaken. Initially, the gas mixture was varied to ascertain the "best" Ar/N_2 ratio for adequate mechanical properties at a reasonable growth rate. This was

followed by a variation of the power/voltage applied to the Cr and WC sputtering targets. The whole process was designed to elaborate on the relationship(s) between growth conditions-coating structure-coating properties.

3.2.1 Fixed Sputtering Power

The deposition conditions for the variation of the sputtering conditions are listed in Table 3.2. Prior to deposition, the substrates were cleaned chemically and then with a 12kV dc glow discharge for 5 min, at an Ar pressure of 2 Pa. To improve adhesion, a 50 nm CrWC buffer layer was deposited; the target Cr:W ratio for this film was 2:1. The plasma-induced voltages of the Cr and WC targets were set at -400 V and -600 V, respectively, and the Ar working pressure was 0.6 Pa. The CrWC underlayer was targeted with a 2:1 ratio of Cr:W. From EDS on a sample made under similar conditions, the composition is 31 at. % C, 45 at. % Cr, 24 at. % W; any oxygen present is below the detection limits (0.1 at. %) of the system. The resulting Cr:W ratio is 1.875:1. The deposition time was varied to obtain a thickness of 2 μm for the CrN-WC layer. Substrates were electrically grounded and deposition temperature was less than 200 °C.

Table 3.2: Deposition conditions for the low deposition temperature study of CrN-WC coatings, with variable gas mixture.

Ar/N_2 Mix	V, Cr [V]	V, WC [V]	t [min]
40/60	-600	-600	417
60/40	-600	-600	400
80/20	-600	-600	364

The target metal ratio for all three samples was 2:1. However, despite the fixed sputtering power and working pressure (0.1 Pa), the actual Cr:W ratios are 2.1, 1.4, and 1.7 for the Ar/N_2 = 40/60, 60/40, and 80/20 samples, respectively. Full EDS results are presented in Table 3.3. Several factors may explain these changes in the metal ratio of the samples. For example, CrN formation is more

energetically favorable over WCN. Also, the addition of N_2 into the gas mixture may affect the WC sputtering rate more strongly than the Cr sputtering rate, i.e. the Cr target suffers less poisoning than the WC target. While there is no clear trend for the Cr:W ratio with the changes in the gas mixture, there is a clear trend with regards to the incorporation of N_2 into the coatings. As more nitrogen was added to the mixture, the films incorporated more nitrogen into the structure.

Table 3.3: EDS results of the CrN-WC coatings created by varying the gas mixture, deposited on Si.

Ar/N_2 Mix	Target Cr:W Ratio	Actual Cr:W Ratio	Cr	W	C	N	O
40/60	2:1	2.13:1	11.9	19.7	14.4	53.3	0.7
60/40	2:1	1.36:1	22.6	14.6	6.3	53	3.5
80/20	2:1	1.71:1	23.1	16.6	14.4	38.7	7.3

Using XPS, further information on the chemical structure can be determined. Starting with the W4f spectra (Fig. 3.11), there are clear differences with the change in the gas mixture. For the highest nitrogen concentration (Fig. 3.11(a)), the W4f is clearly in one state with a peak at 29.9 eV for the $4f^{7/2}$ orbital. When comparing this spectra to the literature, the peaks are shifted by 1.6 eV to the right[4]. In the remaining two samples, Fig. 3.11(b) = 60/40 and Fig. 3.11(c) = 80/20, tungsten is bound in two states (29.5 eV and 30.2 eV). These are most likely carbide states, which are shifted by 2 eV and 1.3 eV, respectively.

The C1s states are much more complicated, Fig. 3.12. The high nitrogen concentration sample deconvolutes into five states: 280.9 eV, 282.8 eV, 284.6 eV, 286.1 eV, and 287.2 eV. The first two are carbide states; the next state is consistent with free carbon; the remaining two are probably C-N and C-O bonds, respectively.

[4]While the XPS system does utilize charge neutralization, it is possible charging could develop within the sample. Sputter etching tends to destroy adventitious carbon, and there is no adequate charge reference. Since the W source is a WC target, the W within the sputtered film will most likely be bonded to carbon. The typical WC peak is located at 31.5 eV [177]; hence, the shift by 1.6 eV, 2 eV, and 1.3 eV for the Ar/N_2 = 40/60, 60/40, and 80/20 samples, respectively. These shifts will be applied to the remaining spectra.

The middle sample has four C1s peaks at 283.2 eV, 285.0 eV, 285.3 eV, and 288.5 eV. These may correspond to a carbide, free carbon, and C-N. The lowest nitrogen gas mixture concentration, Fig. 3.12(c), yields carbide states at 282.6 eV, 284.1 eV, and free carbon at 284.9 eV.

Changing the gas mixture has very little effect on the Cr bonding, Fig. 3.13. All three samples show three $Cr2p^{3/2}$ peaks at 574.2 eV, 575.0 eV, and 576.5 eV. The first two are CrO_x; the last peak is Cr-N. As for the N1s spectra, the high concentration sample (Fig. 3.14(a))has a predominant peak at 397.3 eV, an intermediate peak at 397.0 eV, and a broad peak at 398.7 eV. These correspond to two CrN_x and an azide bonds. The intermediate sample (Fig. 3.14(b))shows a similar peak profile. However, the sample produced with the lowest nitrogen concentration (Fig. 3.14(c)) yields only one Cr-N peak at 397.1 eV.

And finally, the O1s spectra are considered. Once again, starting with the high-nitrogen sample, there are four states: Cr-oxides at 530.1 eV and at 531.1 eV, a hydroxide at 532.6 eV, and a nitrate at 533.7 eV. For the intermediate-nitrogen sample, five states are present: 529.4 eV, 531.0 eV, 531.8 eV, 532.8 eV, and 534.6 eV. These are three metal oxides, a hydroxide, and a nitrate, respectively. The low-nitrogen sample shows four states at 529.4 eV, 529.9 eV, 530.7 eV, and 531.8 eV corresponding to various Cr-oxides.

In summary, the XPS results show very similar bonding structures for the three coatings. Each film consists of WC, CrN, and Cr-oxides, with some free-carbon, azides, hydroxides, and nitrates. While chemical structure is an important part of the picture, it is far from the only part. Crystallographic structure plays a significant part as well. And XRD is used to expand on the crystallography. As shown in Fig. 3.16, all three samples show the typical peak arrangement for a B1 (NaCl) crystal structure [45, 154, 202]. While all three samples show a similar crystallographic structure, the low-nitrogen sample shows a different

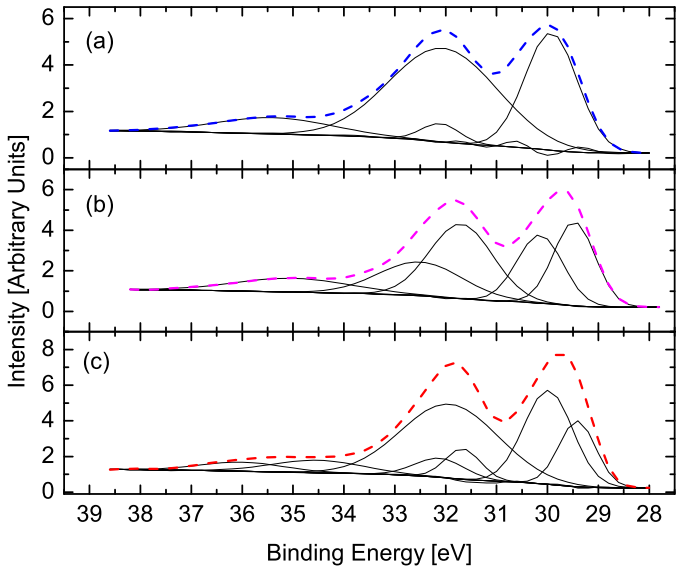

Figure 3.11: W4f spectra from the CrN-WC samples (deposited on Si) with varying gas mixture: (a) $Ar/N_2 = 40/60$, (b) $Ar/N_2 = 60/40$, and (c) $Ar/N_2 = 80/20$. The solid lines are the deconvoluted peaks used for fitting the original data (dashed lines).

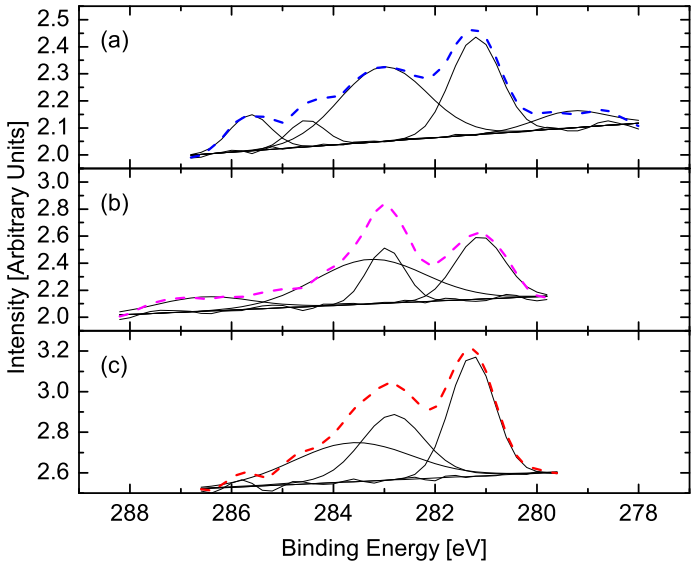

Figure 3.12: C1s spectra from the CrN-WC samples (deposited on Si) with varying gas mixture: (a) $Ar/N_2 = 40/60$, (b) $Ar/N_2 = 60/40$, and (c) $Ar/N_2 = 80/20$. The solid lines are the deconvoluted peaks used for fitting the original data (dashed lines).

preferred orientation compared to the intermediate- and high-nitrogen samples:

(200) compared to (111). This may be indicative of a different growth mode. If a

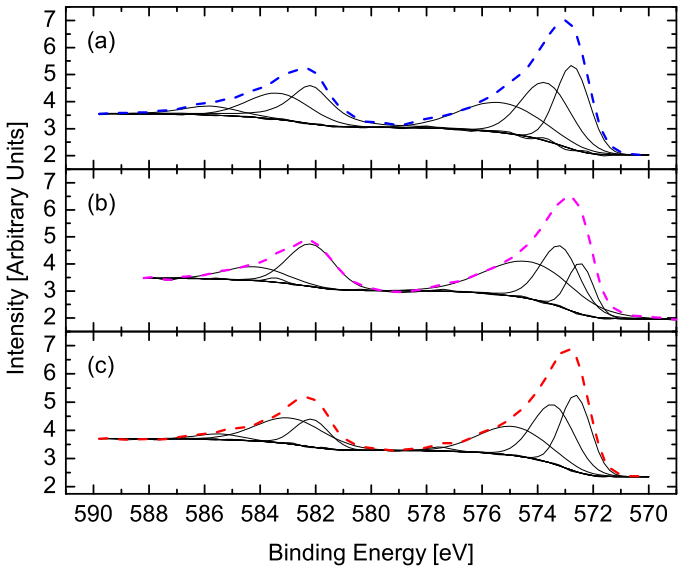

Figure 3.13: Cr2p spectra from the CrN-WC samples (deposited on Si) with varying gas mixture: (a) $Ar/N_2 = 40/60$, (b) $Ar/N_2 = 60/40$, and (c) $Ar/N_2 = 80/20$. The solid lines are the deconvoluted peaks used for fitting the original data (dashed lines).

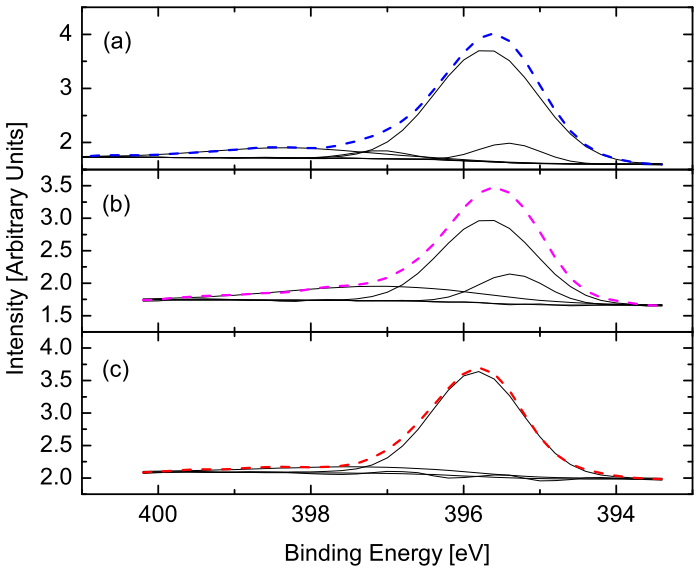

Figure 3.14: N1s spectra from the CrN-WC samples (deposited on Si) with varying gas mixture: (a) $Ar/N_2 = 40/60$, (b) $Ar/N_2 = 60/40$, and (c) $Ar/N_2 = 80/20$. The solid lines are the deconvoluted peaks used for fitting the original data (dashed lines).

single crystalline phase is assumed, the samples may be indexed using the TREOR program within CMPR [173]. This indexing leads to a cubic structure, with a

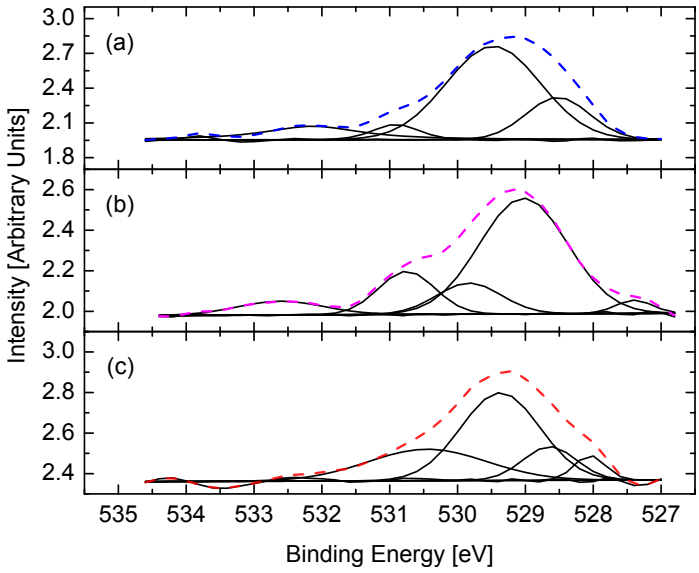

Figure 3.15: O1s spectra from the CrN-WC samples (deposited on Si) with varying gas mixture: (a) $Ar/N_2 = 40/60$, (b) $Ar/N_2 = 60/40$, and (c) $Ar/N_2 = 80/20$. The solid lines are the deconvoluted peaks used for fitting the original data (dashed lines).

lattice parameter of 0.42 nm, for all three samples. Debye-Scherrer analysis on each sample's most intense peak yields an average domain of 9.3 nm, 11.2 nm, and 10 nm for the (a) high-nitrogen, (b) intermediate-nitrogen, and (c) low-nitrogen samples, respectively. However, this single crystalline phase assumption may not hold up. A closer look at the peaks reveals shoulders on the (111), (200) and (220) peaks of each sample, which are indicative of secondary peaks within the main peak, and consequently, secondary crystalline phases with a distribution of grain sizes.

Moving onto HR-SEM results, surface and cross-sectional micrographs are shown in Fig. 3.17. The surfaces appear relatively smooth, with small grains. However, there are few large spherical drops on each surface (see lower section surface micrograph of Fig. 3.17(a)). These are more than likely areas of overgrowth due to defects/contaminates on the Si substrate surface, such as dust particles. AFM confirms this, and the resulting roughness parameters are plotted versus Ar/N_2 ratio in Fig. 3.19. While there is a trend to lower roughness values with higher nitrogen content, the high- and intermediate-nitrogen samples are

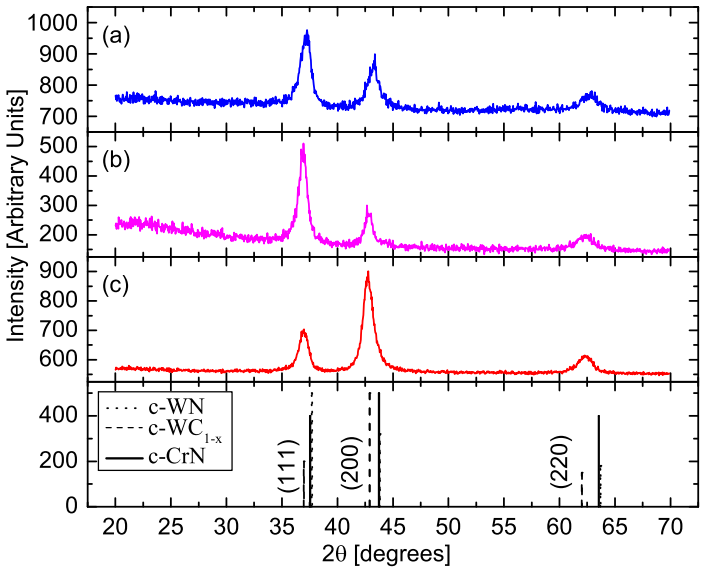

Figure 3.16: X-ray diffractogram for the CrN-WC (deposited on Si) produced by varying the gas mixture: (a) $Ar/N_2 = 40/60$, (b) $Ar/N_2 = 60/40$, and (c) $Ar/N_2 = 80/20$.

significantly lower than the low-nitrogen sample; there is a 56 % difference between the R_{RMS} of the intermediate- and low-nitrogen samples; R_a shows 54 % difference. Both of the intermediate- and high-nitrogen samples have a (111) orientation. The remaining sample has a (200) orientation. Crystallographic orientation can have an effect on the surface roughness [203, 204].

Coating thicknesses and growth modes can be easily determined using the cross-sectional micrographs of Fig. 3.17. Referring to the extended MDT structural zone model presented in Sec. 2.2.3, the generalized temperature for the CrN-WC coatings is ~ 0.18[5]. Without including ion effects, this is within zone T. As such, the coatings should develop tightly-packed, dense fibrous grains. However, depending on the significance of kinetic processes, the growth mode may fall in zone 2. Here, true grain boundaries separate fully developed columns which extend the

[5]This assumes the melting (decomposition) temperature of the coating is equivalent to the lowest melting (decomposition) temperature of the constituent compounds. According to the *CRC Handbook of Chemistry and Physics* [205], the melting temperature of CrN is 1770 °C (2043 K); the melting temperature of WC is 2870 °C (3143 K). Therefore, the melting temperature of CrN is used to determine the generalized temperature.

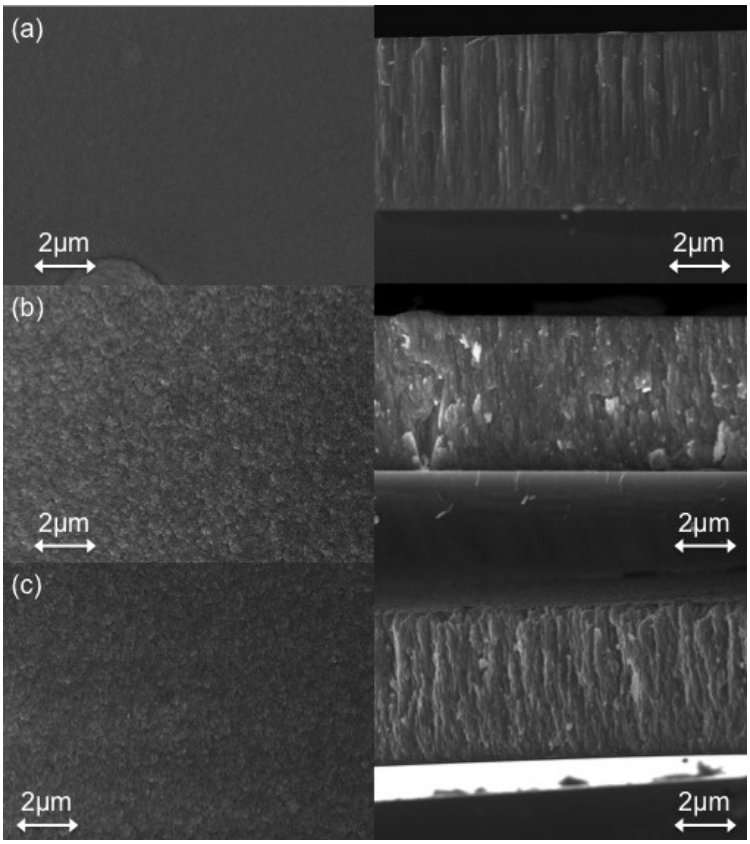

Figure 3.17: High-resolution scanning electron micrographs for the CrN-WC (deposited on Si) produced by varying the gas mixture: (a) Ar/N_2 = 40/60, (b) Ar/N_2 = 60/40, and (c) Ar/N_2 = 80/20.

full thickness of the coating.

Observation shows clear, columnar growth for all three samples. The high-nitrogen sample has well-ordered, aligned columns, with an apparently small diameter and a low porosity (Fig. 3.18). This structure may be formed within the transition between zone T and zone 2. The columns are relatively well-ordered, and appear to extend across the thickness of the coating. However, the relatively small diameter is indicative of reduced adatom mobility. The film is 5.5 μm thick; deposition rate was 13.2 nm/min.

The low-nitrogen sample has ordered columns, but the apparent diameter is larger and a slightly higher porosity. The columns appear to extend most of the film

thickness. As such, the film appears to fall within zone 2. Here is the thinnest sample at 1.9 μm; deposition rate of 5.2 nm/min. This is very unexpected. With low-nitrogen content, the reactive sputtering mode should clearly be within the metallic mode. As such, the targets undergo very little poisoning and the respective deposition rates would be close to the non-reactive sputtering rates. The expected result would have the high-nitrogen content film with the lowest thickness. A high amount of reactive gas in the chamber would lead to target poisoning, and a significant drop in the sputtering rates of the two targets.

The intermediate-nitrogen sample appears as a mix of order and disorder, with a thickness of 4.9 μm; deposition rate of 12.3 nm/min. There is clear columnar growth, but with a more disordered alignment when compared to the other two samples. This microstructure has a very high porosity ($\sim$ 2 %, as shown on Fig. 3.18). i.e. more voids. This mixed microstructure does not clearly fall within zone T nor in zone 2. The columnar grains appear to be larger than the grains in either the high- or low-nitrogen samples. Additionally, the columns do not appear to stretch across the full thickness of the sample. This "disorder" may be indicative of increased adatom mobility. Even though the generalized temperature would indicate otherwise, this sample may actually fall in the transition between zone 2 and zone 3[6].

While crystallographic orientation may have an effect on the surface roughness, the columnar growth mode, and the resulting variations in porosity, do not appear to affect the surface roughness. Overall, the only definitive trend, with respect to surface roughness, is the oxygen contamination. Comparing the results from Table 3.3 with the surface roughness parameters of Fig. 3.19, increased oxygen content (which leads to increased oxide formation) results in an increase in the

[6]It is important to note that the zone boundaries in the MDT model are not fixed. They have some width. Additionally, all structural zone growth models are meant as a generalized guide to describe the different observed growth modes of different coatings. As such, application of these models should allows be taken with a grain of salt.

surface roughness.

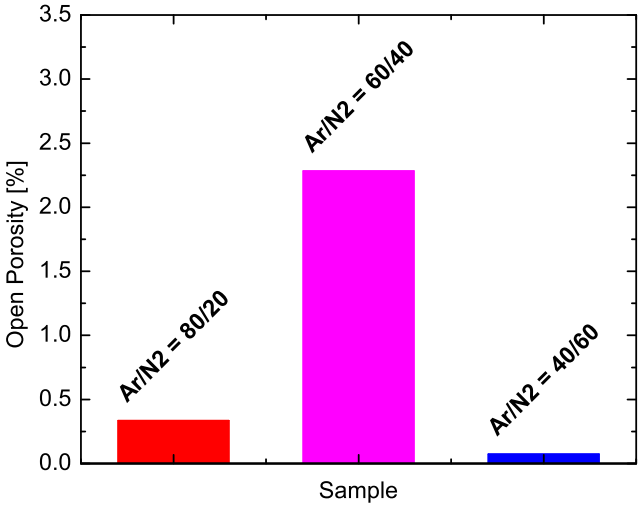

Figure 3.18: Open circuit porosity results for CrN-WC coatings produced by varying the gas composition. These measurements were taken for samples grown on XC100 steel.

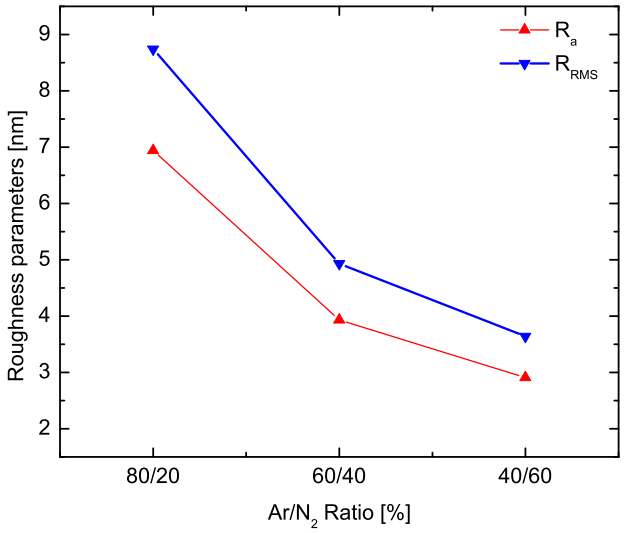

Figure 3.19: Surface roughness parameters of CrN-WC coatings deposited on Si, and grown with varying gas mixtures.

H and E are measured with nanoindentation, and the results for these three coatings are displayed in Fig. 3.20. There is no clear trend in the mechanical properties of the coatings, with respect to the nitrogen concentration in the working

gas. However, there does appear to be a correlation with coating composition. As WC-content is increased, the mechanical properties increase. However, the coatings' values are still lower than expected (compared to the samples in Sec. 3.1).

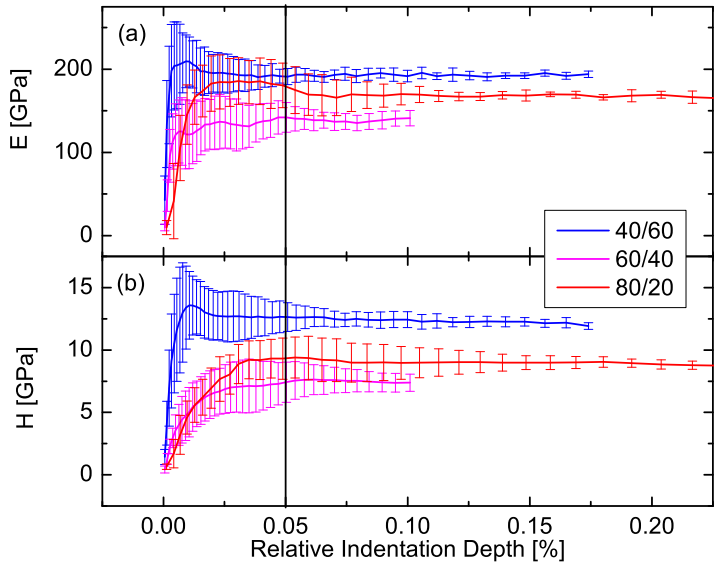

Figure 3.20: The (a) E and (b) H results from the three CrN-WC coatings developed at various Ar/N_2 ratios. To avoid substrate effects, the values are appraised at 5 % of the coating thickness.

There are several possible explanations for this. One is related to the grain sizes of the samples. Once below a critical grain size[7], diffusional creep [99], transfer of dislocations into the grain boundaries [207], grain boundary sliding [208, 209], triple junction effects [101], and/or a combination of these processes [210] may contribute to the reduction of the systems' mechanical properties. This is commonly referred to as the inverse Hall-Petch effect [98].

Another problem may be the low stress state of the coatings. In many materials, high stress states will magnify the elastic response of the material [211]. Using optical profilometry, two coatings show low compressive stress states: -(0.8096 $\pm$ 0.0003) GPa for the high-nitrogen sample and -(0.7778 $\pm$ 0.0005) GPa for the

[7]Currently, the best estimates for critical grain size are $\sim$ 10-20 nm, depending on the system [97, 106, 206].

intermediate-nitrogen sample. The remaining low-nitrogen sample is also under compressive stress, but at at much higher level compared to the other samples: -(3.563 $\pm$ 0.004). The stress does not correlate with the values of the mechanical properties. Therefore, stress may play a role, but it is not likely the major driver for the reduced mechanical properties.

The typical growth mode of Cr may also play a role. Cr (and CrN) tends to form in columnar structures, which are clearly observed here in the cross-sectional micrographs of Fig. 3.17. This growth mode may introduce voids, as evidenced by the porosity, which trap N_2 gas. Ceramic coatings with porosity have shown significantly reduced hardnesses compared to their nonporous counterparts [212, 213]. Another possibility is oxygen contamination. For example, WO_x, and WON have reported hardnesses of 7 GPa [214], and 15 GPa [215], respectively. And while CrO_x is hard at 22 GPa [216], oxygen dissolved in chromium has been shown to reduce the hardness of the metal by a factor of two [217]. XPS results show the presence of free carbon which may be in the graphitic phase. This phase of carbon is expected to be relatively soft. In summary, other material systems have shown a link between high hardness and low impurity levels [107, 114]. The most probable case for the reduced mechanical properties is an unknown combination of stress, growth mode, porosity, and oxygen contamination.

3.2.2 Fixed Gas Mixture

From the variable gas mixture, the next step was varying the sputtering power. Here, the gas mixture is fixed at $Ar/N_2 = 60/40$. A reactive $Ar/N_2 = 80/20$ mixture is clearly metallic, and affects the sputtering rate the least, but the results of Sec. 3.2.1 indicate that this may not be the best mixture. Moving to the other extreme, $Ar/N_2 = 40/60$ produced some interesting results (higher hardness, low porosity, and low surface roughness), but this mixture may lead to significant target

poisoning. As a compromise between the metallic sputtering rate of the low-nitrogen mixture and the target poisoning of the high-nitrogen mixture, the intermediate mixture is within the compound sputtering range. This results in decent film properties with a reasonable deposition rate.

The deposition conditions for the variation of the sputtering conditions are listed in Table 3.4. Similar to the samples from the prior section (Section 3.2.1), prior to deposition, the substrates were cleaned chemically and then with a 12kV dc glow discharge for 5 min, at an Ar pressure of 2 Pa. Additionally, the same Cr-WC interlayer was used to improve adhesion for both the variable gas mixture and variable metal ratio studies. The deposition time was varied to obtain a thickness of 2 μm for the CrN-WC layer. Substrates were electrically grounded and deposition temperature was less than 200 °C. The working gas was a 60/40 mixture of Ar/N_2 and a pressure of 0.1 Pa.

Table 3.4: Deposition conditions for the low deposition temperature study of CrN-WC coatings, with fixed Ar/N_2 gas mixture and deposited on Si.

Target Cr:W Ratio	V, Cr [V]	V, WC [V]	t [min]
1:1	-300	-600	667
1.5:1	-450	-600	445
2:1[a]	-600	-600	400
3:1	-900	-600	222
4:1	-900	-450	222

[a]Same sample from Section 3.2.1, and is also described here for comparison purposes.

In Fig. 3.21, the diffractograms of the CrN-WC samples are presented. Starting from the bottom, Fig. 3.21(e) shows the Cr:W = 1:1. It is very similar to the WCN sample, see Fig. 3.1(c). However, the CrN-WC coating has a slightly narrower peak, and its location is shifted to the right. The center of the WCN peak was located at 34.9° (with a FWHM of 6.1°), the center of this low-Cr content peak is located at 35.6° (with a FWHM of 5.3°)[8]. This leads to an average crystallite size

[8]All spectra were taken on the same instrument, i.e. the instrumental broadening is 0.31°.

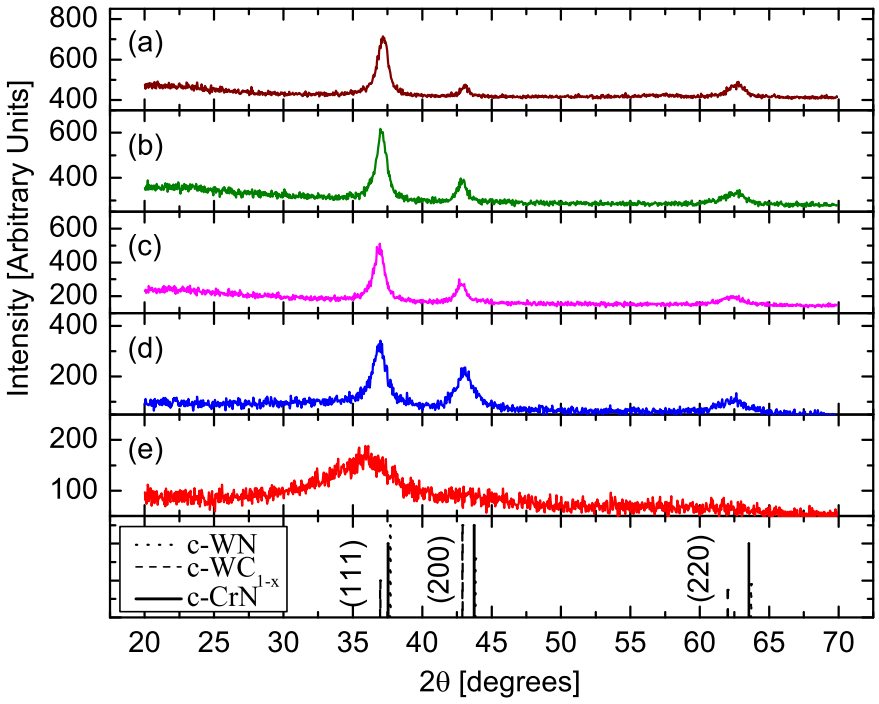

Figure 3.21: XRD diffractogram of the CrN-WC samples (deposited on Si), with varying Cr:W ratios: (a) Cr:W = 4:1, (b) Cr:W = 3:1, (c) Cr:W = 2:1 (d) Cr:W = 1.5:1, and (e) Cr:W = 1:1. The remaining panel shows the PDF peaks of c-WN, c-WC_{1-x}, and c-CrN.

of 1.9 nm for the CrN-WC coating.

While Cr tends to shift the diffraction peaks to higher angle, the crystallite size is very similar. Therefore, additions of small amounts of Cr do not appear to significantly affect the crystalline structure. Within the purview of XRD, this sample may be regarded in a very similar vein as the WCN sample of Section 3.1. The symmetry of the peak implies a single phase system, but multiple phases are most likely present.

As Table 3.5 shows, the Cr:W ratio of the first sample is very low at 0.6:1. Additionally, if you look at the combined metal content, i.e. Me = Cr + W, it is about half the (C + N) content. The XPS results, after 30 min Ar-ion sputter etching at 1 kV accelerating voltage, of the W4f, C1s, Cr2p, N1s, and O1s peaks are shown in Fig. 3.22(e), Fig. 3.24(e), Fig. 3.23(e), Fig. 3.25(e), and Fig. 3.26(e). The

Table 3.5: EDS results of the CrN-WC coatings created by varying the Cr:W ratios, deposited on Si.

Target Cr:W Ratio	Actual Cr:W Ratio	Cr	W	C	N	O
1:1	0.6:1	11.9	19.7	14.4	53.3	0.7
1.5:1	1.6:1	22.6	14.6	6.3	53	3.5
2:1[a]	1.4:1	23.1	16.6	14.4	38.7	7.3
3:1	3.4:1	32	9.5	9.9	42.3	6.3
4:1	5.13:1	34.9	6.8	9.6	41.4	7.5

[a]Same sample from Section 3.2.1, and is also described here for comparison purposes.

W4f deconvolutes into two states, with peaks located at 29.8 eV and 30.4 eV for the $4f^{7/2}$ orbital. Using the PHI Handbook [177] and the NIST database [189], these are most likely a carbide and oxide, respectively. The C1s spectra has a predominate peak at 281.5 eV and a smaller shoulder centered at 282.9 eV. Both of these are carbides.

The trend of two states continues in Cr2p, with the $2p^{3/2}$ peaks at 572.9 eV and 574.0 eV. N1s is a bit more complicated with three peaks at 395.3 eV, 395.9 eV, and 397.3 eV; these are consistent with metal nitrides. The remaining O1s spectra yields 4 states: 526.7 eV, 528.4 eV, 529.3 eV, and 530.8 eV. These peaks are most likely associated with metal oxides. In summary, the low-Cr content sample consists of multiple phases, with various carbides, nitrides, and oxides of both W and Cr.

It is impossible to separate crystalline and amorphous phases with the current set of XRD, EDS, and XPS measurements. As such, it may be no longer valid to assume a single crystalline phase, with an average crystallite size of 2 nm. Using the peak-fitting feature in OriginPro, it is possible to deconvolute the broad peak at 35.6° into several peaks. This yields a range of average crystallite sizes, from 3-13 nm.

Despite the apparent polycrystalline nature of the coatings, HR-SEM micrographs show a smooth, dense[9] film in Fig. 3.29(e). AFM results, presented in

[9]Coating thickness of 5.2 μm; deposition rate of 7.8 nm/min.

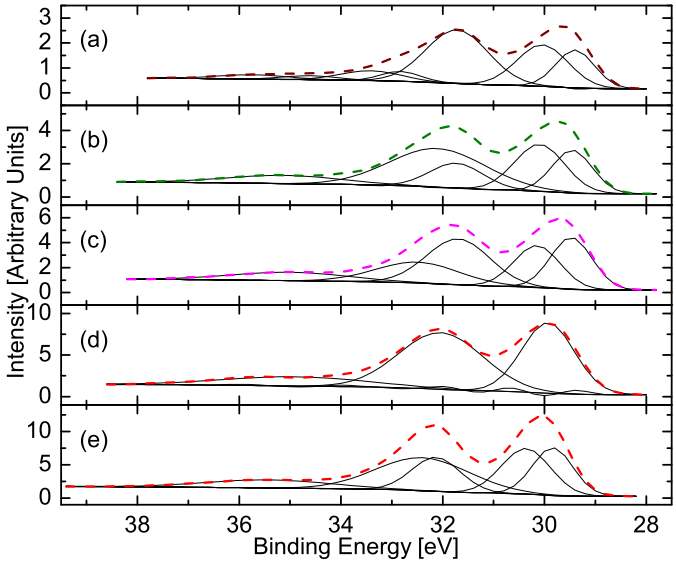

Figure 3.22: W4f spectra from the CrN-WC samples (deposited on Si) with varying metal content: (a) Cr:W = 4:1, (b) Cr:W = 3:1 , (c) Cr:W = 2:1, (d) Cr:W = 1.5:1, and (e) Cr:W = 1:1 samples. The solid lines are the deconvoluted peaks used for fitting the original data (dashed lines).

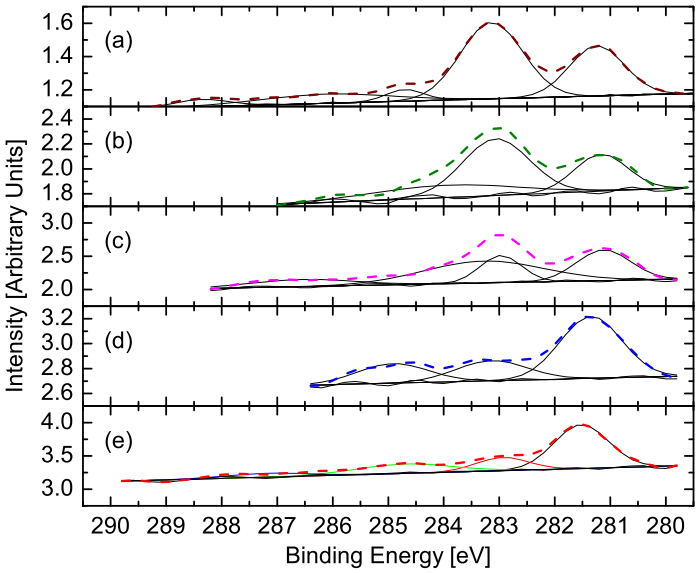

Figure 3.23: C1s spectra from the CrN-WC samples (deposited on Si) with varying metal content: (a) Cr:W = 4:1, (b) Cr:W = 3:1 , (c) Cr:W = 2:1, (d) Cr:W = 1.5:1, and (e) Cr:W = 1:1 samples. The solid lines are the deconvoluted peaks used for fitting the original data (dashed lines).

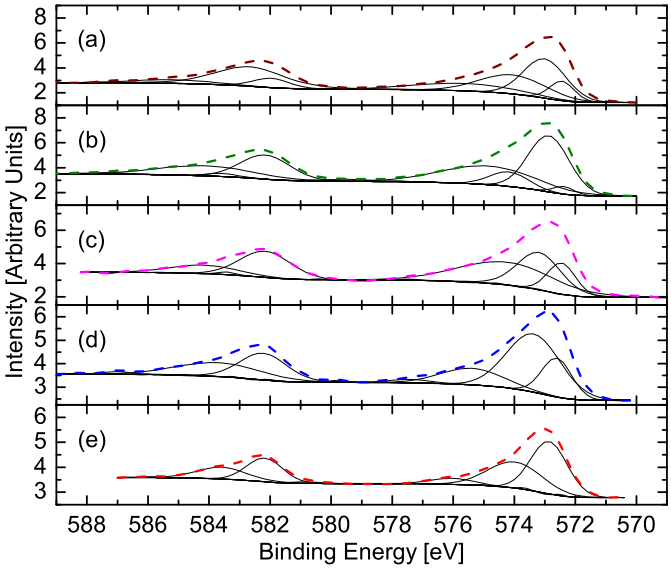

Figure 3.24: Cr2p spectra from the CrN-WC samples (deposited on Si) with varying metal content: (a) Cr:W = 4:1, (b) Cr:W = 3:1 , (c) Cr:W = 2:1, (d) Cr:W = 1.5:1, and (e) Cr:W = 1:1 samples. The solid lines are the deconvoluted peaks used for fitting the original data (dashed lines).

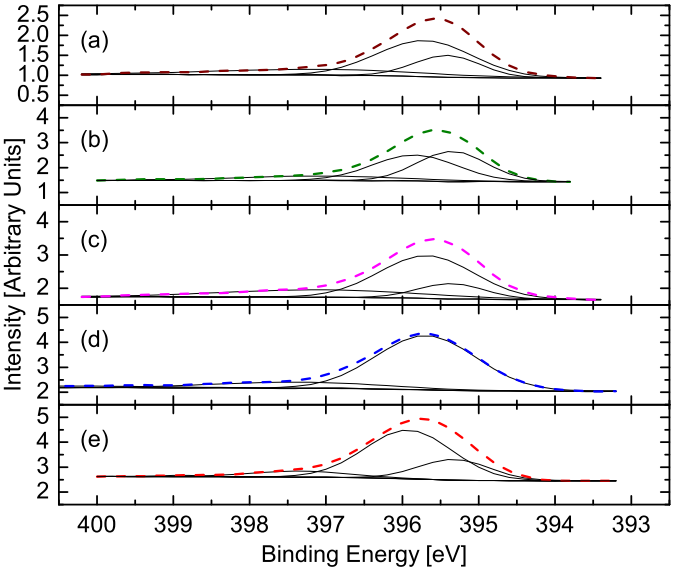

Figure 3.25: N1s spectra from the CrN-WC samples (deposited on Si) with varying metal content: (a) Cr:W = 4:1, (b) Cr:W = 3:1 , (c) Cr:W = 2:1, (d) Cr:W = 1.5:1, and (e) Cr:W = 1:1 samples. The solid lines are the deconvoluted peaks used for fitting the original data (dashed lines).

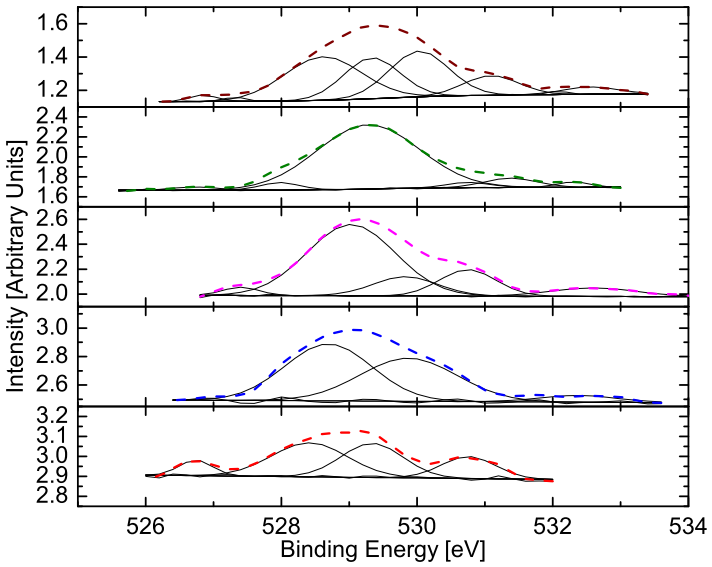

Figure 3.26: O1s spectra from the CrN-WC samples (deposited on Si) with varying metal content: (a) Cr:W = 4:1, (b) Cr:W = 3:1 , (c) Cr:W = 2:1, (d) Cr:W = 1.5:1, and (e) Cr:W = 1:1 samples. The solid lines are the deconvoluted peaks used for fitting the original data (dashed lines).

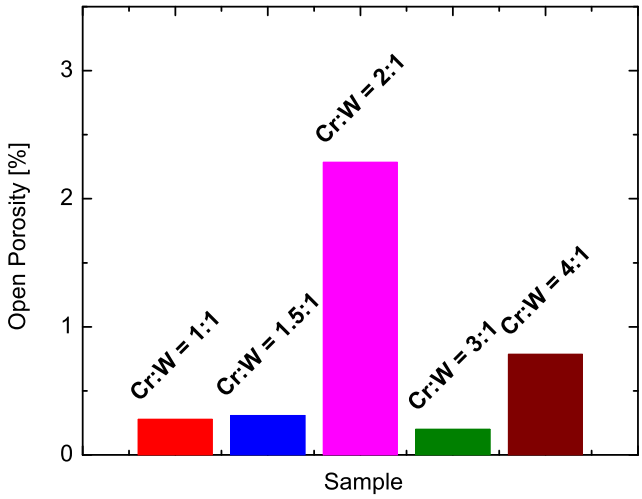

Figure 3.27: Open circuit porosity of the CrN-WC coatings deposited at low deposition temperature, and at fixed gas mixture; deposited on XC100 steel.

Fig. 3.30 confirm the smooth nature of the coating surface. Additionally, open circuit porosity tests yield a coating porosity of only 0.3 % (Fig. 3.27), which correlates with the "dense" structure observed in the cross-sectional HR-SEM micrograph. The electrochemical tests also show significant post-test delamination

(see Fig. 3.28(e)); the film adhesion to XC100 (AISI 1095) steel appears to be very low. This is confirmed by scratch testing, which yields critical loads of only 6.5 N, 9.7 N and 14.3 N for L_{C1}, L_{C2} and L_{C3}, respectively.

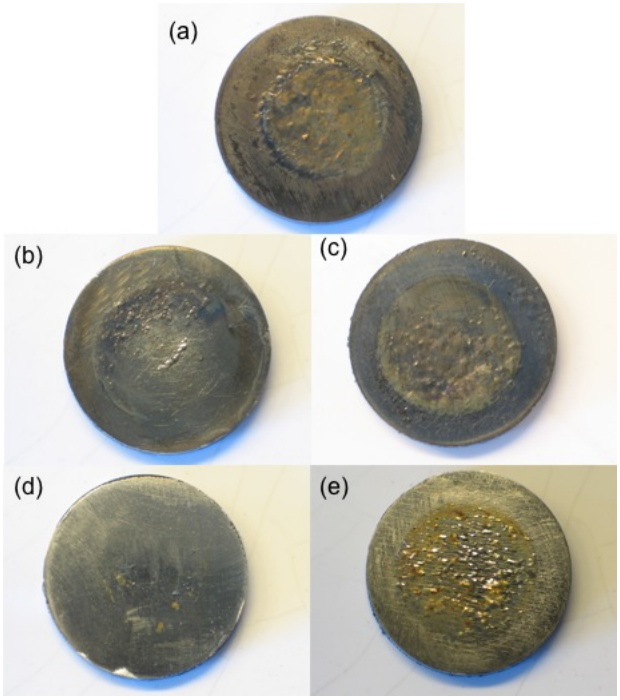

Figure 3.28: Optical micrographs of the post-electrochemical test (for open circuit porosity) surfaces (deposited on XC100 steel): (a) Cr:W = 4:1, (b) Cr:W = 3:1, (c) Cr:W = 2:1, (d) Cr:W = 1.5:1, and (e) Cr:W = 1:1.

While the multiple phases may be undesirable for some applications, the nanoscale domain sizes are typically advantageous for high hardness. However, in the case of the Cr:W = 1:1 coating, this may not hold true. Using nanoindentation, the Hardness (H) and Young's Modulus (E) for the samples are obtained using the Oliver-Pharr method [64]. To avoid substrate effects, H and E are evaluated at 5 % of the film thickness, as shown in Fig. 3.31. For the low-Cr content sample, i.e. Cr:W = 1:1, the coating H is 6.8 GPa and E is 134 GPa; the fracture toughness is proportional to H^3/E^2 which is 0.02 for this coating. This is actually more consistent with an oxide coating, such as TiO_2, than a metallic coating, such as TiN (see Tables 1.1 and 1.2).

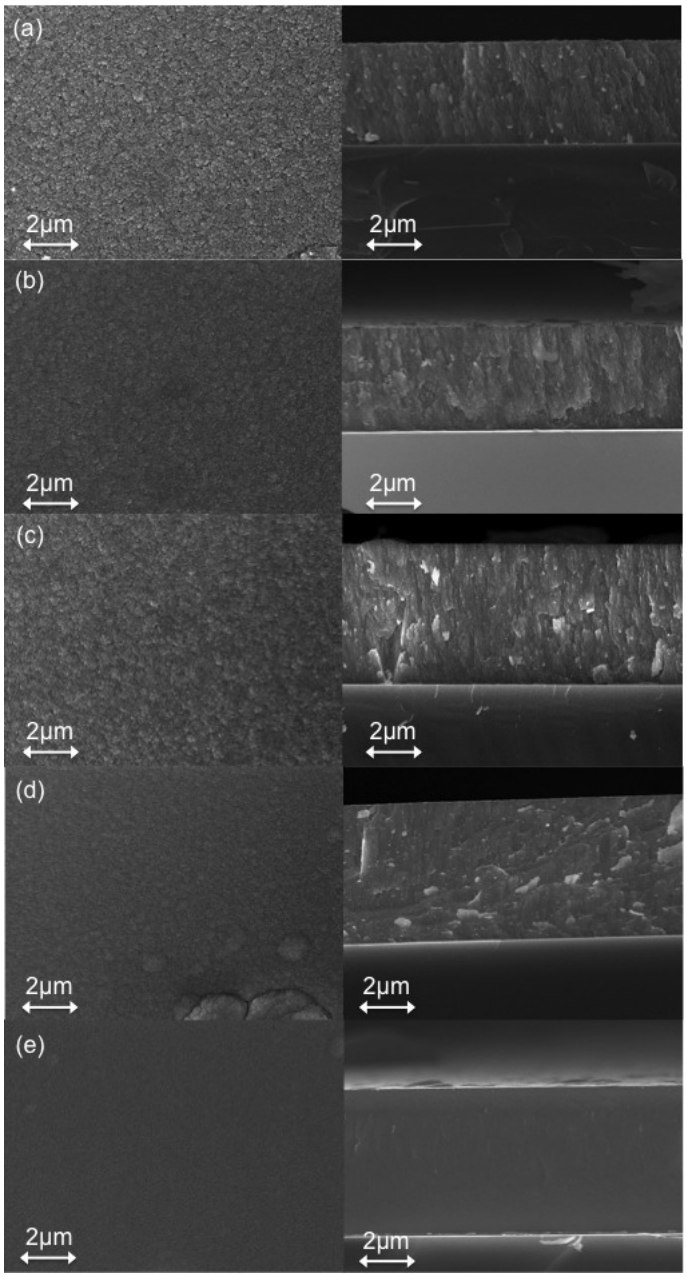

Figure 3.29: Surface topography and cross-sectional HR-SEM micrographs of the (a) Cr:W = 4:1, (b) Cr:W = 3:1, (c) Cr:W = 2:1, (d) Cr:W = 1.5:1, and (e) Cr:W = 1:1 samples developed at a fixed gas mixture and deposited on Si.

One possible explanation is the wide range of domain sizes below the threshold for normal Hall-Petch hardening. As noted in Sec. 3.2.1, the critical size for the transition from normal Hall-Petch hardening to the inverse Hall-Petch effect is $\sim$ 10-20 nm. From the XRD results, the Cr:W = 1:1 sample has a distribution of

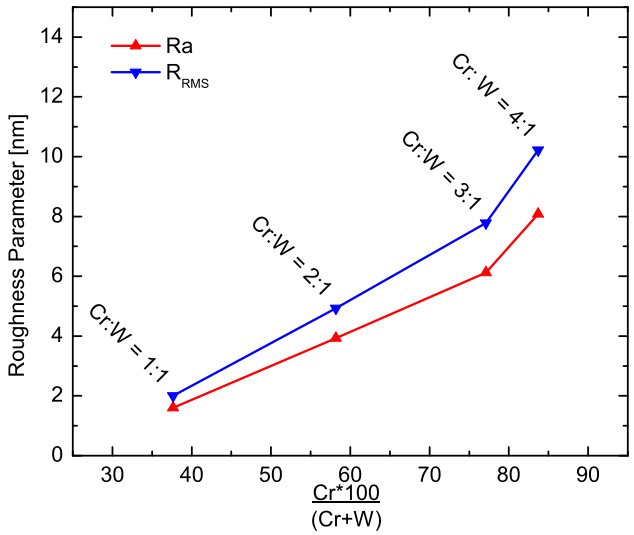

Figure 3.30: Using a 5 × 5 μm^2 scan, AFM determined the surface roughness of the CrN-WC coatings developed at a fixed gas mixture and deposited on Si.

grain sizes well below the critical size. This would have a clear and detrimental effect on the system's mechanical properties. Additionally, the film shows low compressive stress (-0.4502 ± 0.0003 GPa). Stress has been shown to have a dramatic effect on the hardness of various films [211]. Here, the lack of significant stress may also affect the observed mechanical properties.

Further addition of Cr results in a significant rearrangement of the crystalline structure. From the single broad peak of WCN and low-Cr content CrN-WC, the structure transforms and the (111), (200), and (220) peaks appear, see Fig. 3.21. This is the typical peak arrangement for a B1 (NaCl) crystal structure [45, 154, 202]. However, using the TREOR program within CMPR [173], the indexing of this sample leads to a tetragonal crystal structure; the lattice parameter of the basal plane is 0.3 nm and 0.42 for the c-axis. Additionally, it is easily noted that the peaks for the Cr:W = 1.5:1 are significantly narrower, with an FWHM of 0.91°. Using the most intense peak and assuming a single crystalline phase, the average size of the coherent scattering domains is 10.9 nm.

Moving onto the XPS, the changes are observable, but not as dramatic. As

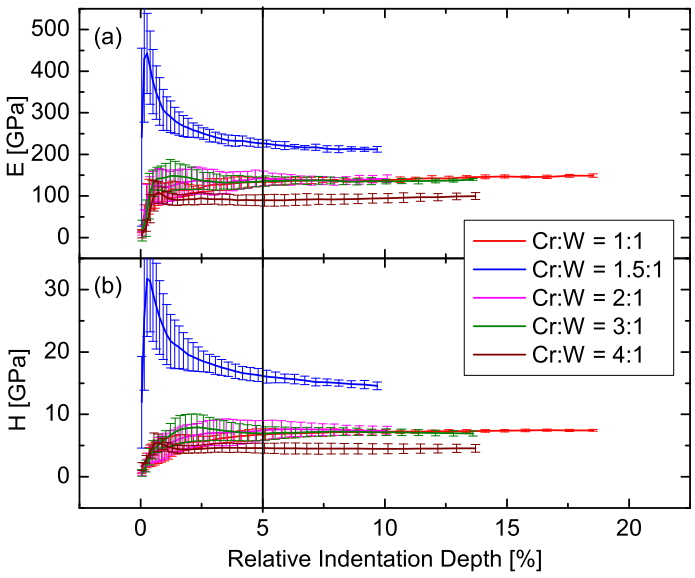

Figure 3.31: Nanoindentation results for the (a) Young's modulus and (b) Hardness for the CrN-WC coatings developed with a constant gas mixture and deposited on Si.

Fig. 3.22(d) shows the W4f is in a single carbide state at 29.9 eV for the $4f^{7/2}$ orbital. The C1s, Fig. 3.23(d), is in three states a predominant peak at 281.4 eV, and two much smaller peaks at 283.1 eV and 284.9 eV. There are also three states in the Cr2p spectrum, Fig. 3.24(d), at 572.6 eV, 573.4 eV, and 575.4 eV for the $2p^{3/2}$ orbital. N1s has a single peak at 395.7 eV. Unfortunately, the binding energies for WN and CrN are very similar. However, since the W4f is clearly in one state, and Cr-N bonds are more energetically favorable, it is reasonable to deduce the N1s spectrum shows a Cr-N bond. O1s (Fig. 3.26(d)) yields two states at 528.7 eV and 529.9 eV, both metal oxides; these are most probably Cr-O bonds. In summary, the Cr:W = 1.5:1 coating contains W-C, Cr-N, Cr-O, and some free carbon[10].

It should be noted that XPS yields information about chemical bonds, and XRD yields information about crystal structure. In other words, one cannot tell the other what is going on. With these coatings, there may be only one crystalline

[10]The presence of free carbon has been confirmed by Raman spectroscopy, with a broad peak at 1600 cm^{-1}.

phase coexisting with several x-ray amorphous phases. Using the peak-fitting protocol of OriginPro 8.51, the best fit yields a single crystalline phase.

As such, it is reasonable to assume the CrN-WC coating (with the metal ratio of Cr:W = 1.5:1) is a nanocomposite. It consists of several phases, with nanoscale domains. This deduction is based on combining the nature of the XRD, the multiple chemical bonds present in the XPS spectra, and the limited solubility of Cr into WC [155].

Moving onto the surface topography, the HR-SEM micrograph (Fig. 3.29(d)) show a smooth coating, but not quite as smooth as the low-Cr content coating. This is probably due to the higher crystallinity of this sample, and the columnar growth mode, as shown in the cross-sectional HR-SEM. Additionally, the coating thickness is 4.8 μm; deposition rate is 10.8 nm/min. It is interesting to note that the columnar growth mode of this Cr:W = 1.5:1 sample does not significantly change the film porosity from the Cr:W = 1:1 sample. In both cases, the open circuit porosity yields 0.3 % (Fig. 3.27). However, looking at Fig. 3.28(d), the 1.5:1 sample shows the best adhesion after the corrosion test for determining the porosity. Scratch tests were not performed on this sample to determine the critical loads.

Typically, nanocomposite coatings show higher than expected hardness, modulus, and fracture toughness compared to "normal" coatings. As explained in Section 1.3.3.2, this is usually attributed to a change in the dislocation nucleation and movement. In materials with larger grains, the dislocations nucleate and propagate within the grain, and through the grain boundary (without significant scattering). However, when the grain size is nanoscale, the dislocations will nucleate in both the grains, and grain boundaries. This inhibits their propagation, and leads to improved mechanical properties. With this Cr:W = 1.5:1 coating, the H is 16.1 GPa, the E is 223 GPa, and $H^3/E^2 = 0.084$. This is comparable to a single-phase, binary coatings, but it is much lower than expected for a nanocomposite coating.

Once again, the inverse Hall-Petch effect may be rearing its head. The exact mechanism through which this effect is acting (i.e. diffusional creep, dislocation transfer, grain boundary sliding, or a combination of these) has yet to be resolved for simple binary systems, let alone a complex, multi-phase system such as a nanocomposite.

Further increase in the chromium content of the films does not significant alter the crystallographic structure. While each increase in Cr content produces a slight shift to higher Bragg angles, the FWHM is approximately the same for Cr:W = 1.5:1 and all remaining coatings (Cr:W = 2:1, 3:1, and 4:1). However, indexing the peaks does show a slight transformation from the tetragonal phase to a cubic structure; here, all lattice parameters settle at 0.42 nm. This may be due to stress relaxation and/or additional phase segregation between the amorphous and the crystalline components.

XPS results for the W4f spectra (Fig. 3.22) for the high-Cr content samples are similar to each other, but different from the Cr:W = 1.5:1 sample. The high-Cr content seems to develop two states at 29.5 eV and 30.1 eV. These are most likely the carbide and an oxide bond, respectively, shifted by 1.6 eV. Moving to the C1s spectra (Fig. 3.23) three states are observed in each of the three samples: $\sim$ 282.7 eV, $\sim$ 284.6 eV, and $\sim$ 284.9 eV. However, the relative amounts of each bond are different. In the case of Cr:W = 2:1 (Fig. 3.23(c)), there deconvoluted peaks are approximately the same intensity. Figure 3.23(b) shows the Cr:W = 3:1 sample with 284.6 eV as the predominant bond, 282.7 eV is next, with 284.9 eV showing the least amount of bonding. These peak locations correspond to graphitic carbon, carbide, and free carbon bonds, respectively. In the remaining sample (Fig. 3.23(a)), the intensity structure is the same as the 3:1 sample.

Figure 3.29(a-c) show the surface topography and cross-sectional HR-SEM micrographs of the Cr:W = 4:1, 3:1, and 2:1 samples, respectively. There are no

significant differences in the cross-sections; all samples clearly show columnar growth. Similar to Sec. 3.2.1, the cross-sections yield coating thicknesses (deposition rates) of 3.4 μm (15.3 nm/min), 3.6 μm (16.2 nm/min), and 4.9 μm (12.3 nm/min). With regards to the surface, the films remain relatively smooth, but there is a clear trend of increasing surface roughness with increasing Cr-content, as shown in Fig. 3.30. There is no ready explanation for this effect. The crystallite size remains approximately the same, as does the observed grains in the micrographs of Fig. 3.29(a-c). Additionally, porosity cannot be a major factor, as there is no trend in the data (Fig. 3.27).

Finally, the mechanical properties offer an interesting picture. While it is weak, there is a trend of decreasing hardness (and increasing Young's modulus) with increasing Cr-content. H (E) results yield 4.6 GPa (90 GPa), 7.0 GPa (134 GPa), 7.3 GPa (142 GPa) for Cr:W = 4:1, 3:1, 2:1, respectively. These opposing trends negate any trend in the fracture toughness, H^3/E^2 = 0.012, 0.02, and 0.02 for Cr:W = 4:1, 3:1, and 2:1, respectively; these nanoindentation results are lower than those of XC100 (H = 10.4 GPa; E = 234 GPa; H^3/E^2 = 0.021), taken under similar conditions. Also, this weak trend does not extend to the 1.5:1 and 1:1 sample which show 16.12 GPa (223 GPa) and 6.8 GPa (134 GPa), respectively[11].

Of course, these lower than expected results beg the question why. There are several possibilities, such as grain-size effects (which were discussed in Sec. 3.2.1), significant oxygen contamination, the presence of amorphous carbon, and the low stress states of the coatings. In all three high-Cr content coatings, the oxygen content ranges for 6-7 at. %. XPS results show this oxygen is typically bonded, forming metal oxides which may affect the coating mechanical properties the same as described in Sec. 3.2.1. The additional impurity of a soft carbon phase would also reduce the composite hardness of the coatings.

[11] According to the EDS results of Table 3.5, the 1.5:1 sample actually has a higher Cr content (at 1.6:1) than the 2:1 sample (at 1.4:1).

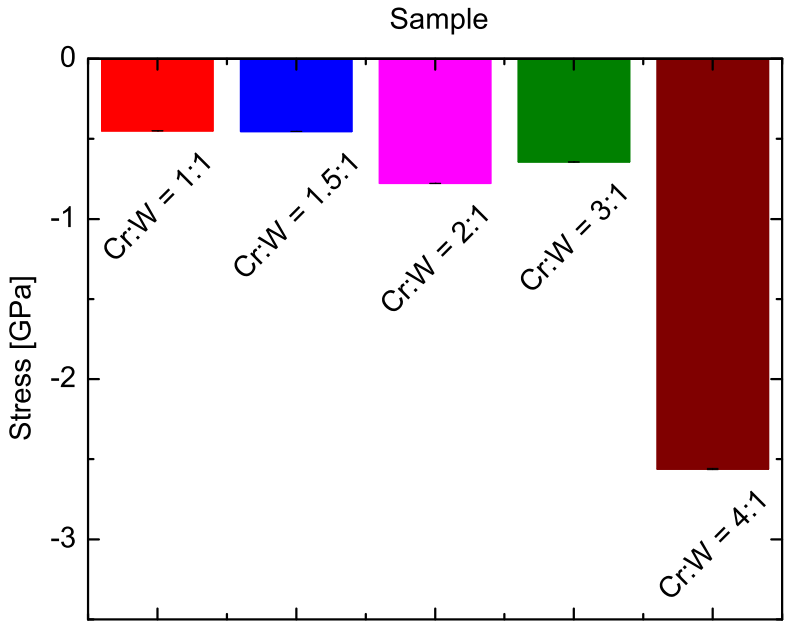

Figure 3.32: Compressive stress of CrN-WC samples deposited on Si, at low fixed Ar/N_2 ratio and low deposition temperature.

Wafer curvature measurements with an optical profilometer yield -2.561 ± 0.004 GPa, -0.6445 ± 0.0005 GPa, -0.7778 ± 0.0005 GPa, -0.4537 ± 0.0002 GPa, and -0.4502 ± 0.0003 GPa for the Cr:W = 4:1, 3:1, 2:1, 1.5:1, and 1:1 samples, respectively. This lack of a trend in the stress values can be observed in Fig. 3.32. The low stresses of the Cr:W = 3:1, 2:1, and 1:1 samples could easily affect the mechanical properties of the coatings [211]. However, this line of reasoning does not seem to apply to the remaining samples. The 4:1 sample has the highest Cr-content and the highest stress, but lowest hardness. And the 1.5:1 sample has low-stress and an intermediate Cr-content, but shows the highest hardness.

Additionally, porosity may be playing a role in the low mechanical properties of the samples. However, the relationship is not clear cut; the porosity values does not trend with any measured film property. For the Cr:W = 4:1, 3:1, 2:1, 1.5:1, and 1:1, the values are 0.8 %, 0.2 %, 2.3 %, 0.3 %, and 0.3 %, respectively (see Fig. 3.27). Looking at the post-corrosion test sample surface (Fig. 3.28), it is easy

to note the film lift-off for the majority of samples. Only the Cr:W = 1.5:1 appears to have survived relatively unscathed. Since there appears to be little correlation between the measured film porosity and the amount of surface damage, this damage is probably due to poor film adhesion and possible pin-hole defects in the film surface. In all likelihood, the lower than desired mechanical properties are due to a combination of low-stress, high-oxygen contamination, low adhesion, and multiple grain sizes below the threshold for normal Hall-Petch hardening.

3.2.3 Summary for the low-temperature deposition of CrN-WC coatings

Two studies were completed for CrN-WC coatings, deposited at low-temperature. With the first, the applied target power was kept constant (with a targeted Cr:W ratio of 2:1), as the Ar/N_2 gas mixture was varied: 80/20, 60/40, and 40/60. For the second study, the gas mixture was fixed at $Ar/N_2 = 60/40$ while the applied target power was varied. This resulted in changes in the Cr:W ratio. Five different compositions were created to study the relationship between the coating composition and the resulting properties.

Varying Gas Mixture

- Changing the nitrogen partial pressure does not seem to have an affect on the types of bonding present.
  - From EDS (Table 3.3), nitrogen incorporation was maxed out at the intermediate gas mixture of $Ar/N_2 = 60/40$.
  - XRD (Fig. 3.16) support this. At low-nitrogen content, the preferred orientation for the coating is (200). However, above saturation (i.e. maximum nitrogen incorporation), the preferred orientation is (111). This appears to be logical. Low-nitrogen incorporation should produce denser films; (200) planes have a higher packing density than (111) planes.

  - Surface roughness is also correlated (Fig. 3.19): the low-nitrogen coating has significantly higher surface roughness than the other two samples (both at maximum nitrogen content).

- An additional affect of changing the nitrogen concentration is observed in the deposition rate, and the growth mode.

  - Unexpectedly, the low-nitrogen partial pressure has the slowest growth
  - Fig. 3.17 shows large, but ordered grains in the low-nitrogen sample. The larger grains indicate higher adatom mobility, and this may also explain the lower deposition rate (i.e. low adatom lifetimes).
  - At higher nitrogen incorporation (i.e. saturation), the growth rates were both reasonable at 12.3 nm/min and 13.2 nm/min for the intermediate- and high-nitrogen partial pressure samples, respectively. This is may be the result of decreased adatom mobility, i.e. longer adatom lifetimes, as compared to the low-nitrogen sample.
  - Despite nitrogen saturation in both the intermediate- and high-nitrogen samples, there is a difference in the growth mode of these two coatings.
    * The intermediate-nitrogen sample seems to have a growth mode near the boundary between zones 2 and 3 in the extended MDT model. This sample does appear to suffer from significant voids, i.e. high porosity.
    * The high-nitrogen sample appears to fall at the other end of the zone, at the boundary between zone T and zone 2. And this sample appears to be fairly dense, with low porosity ($\sim$ 0.3 %).

- The only clear trends are

  - decreasing surface roughness with increased nitrogen partial pressure;

  - increased deposition rates with increased nitrogen partial pressure.

- The intermediate gas mixture was chosen to continue the experiments in the next phase: varying the applied sputtering power. This should maximize the chances of a reasonable deposition rate, with low surface roughness and decent mechanical properties.

Varying Sputtering Power

- At low Cr-content, a "solid-solution" forms with a single broad peak, across several different phases.

- At higher Cr-content, the film appears to form a nanocomposite structure. However, despite XRD and XPS results, it is unclear if this nanocomposite consists of multiple nanocrystalline phases, or a combination of a nanocrystalline phase and an amorphous phase.

- Very few trends with changing composition

  - Mechanical properties decrease with increased Cr-content, with exception of Cr:W = 1.5:1 coating.

  - Increased surface roughness with increased Cr-content

- All films show compressive stress, but no obvious relationship between the stress development and the chemical composition.

- Optical micrography of post-corrosion test surfaces show significant damage to the coatings, Fig. 3.28. Only the Cr:W = 1.5:1 sample seems to have survived without delamination.

- Lower than expected mechanical properties, based on results of Sec. 3.1. This may be due to a combination of factors, such as:

- Low stress state
- Poor film adhesion
- High oxygen contamination

The primary target of the remaining study (i.e. coating growth at high temperature) is improved coating mechanical properties via improved film adhesion, lower oxygen contamination, and increased film stress. An additional bonus from substrate heating is the improvement in adatom mobility which should assist in phase segregation.

3.3 Variation of Deposition Conditions of CrN-WC Films at High Deposition Temperature

As stated in the above summary for Sec. 3.2, the targeted goal for coating growth at increased deposition temperature is improved mechanical properties through improved adhesion, stress development, reduced contamination, and increased phase segregation of the constituent compounds. Additionally, there is still the desire to develop these CrN-WC coatings as an intermediate layer for nanocrystalline-Diamond (nc-D) growth. In order to achieve these goals, the high temperature study was broken down into two sections:

- Thin film deposition at variable growth temperature;
- Coating development at a fixed deposition temperature.

The first part of the study investigates the variation of the film properties with different growth temperatures. In addition, these thin films are subjected to nc-D growth conditions, via Microwave Plasma Chemical Vapor Deposition (MPCVD). The second part of the study investigates the variation of film properties with changes in composition, while at an elevated growth temperature. The deposition

conditions for these two studies are listed in Table 3.6. For all coatings, the working pressure was 0.1 Pa, with an Ar/N_2 gas mixture of 60/40.

Table 3.6: Deposition conditions for the high deposition temperature study of CrN-WC coatings.

Sample	Composition	P, Cr [W]	P, WC-Co [W]	t [min]	T [°C]
Variable Temperature					
H1001	CrN-WC	200	100	64	66 (No External Heating (NEH))
H1002	CrN-WC	200	500	31	75 (NEH)
H1003	CrN-WC	200	100	64	185
H1004	CrN-WC	200	500	31	270
H1005	CrN-WC	200	100	64	260
H1006	CrN-WC	200	500	31	170
H1007	CrN-WC	200	100	52	400
H1008	CrN-WC	200	500	31	390
Fixed Temperature					
D201	CrN	100	100	180	400
E201	WC-Co	100	100	180	400
G201	WCN-Co	100	100	180	400
H201	CrN-WC	100	100	180	400
H202	CrN-WC	100	100	180	400
H203	CrN-WC	100	100	180	400
H204	CrN-WC	100	100	180	400
H205	CrN-WC	100	100	180	400
H206	CrN-WC	100	100	180	400

3.3.1 Thin films at Variable Temperature

For this part of the study, two different compositions (Cr:W = 0.5:1, 3:1)[12] of CrN-WC coatings were deposited at four different temperatures: plasma temperature, 180 °C, 270 °C, and 400 °C. Suitable deposition times were chosen to keep film thickness $\sim$ 500 nm. After deposition and initial characterization, these coatings were subjected to nc-D deposition in the MPCVD chamber at UAB.

Table 3.7 lists the EDS results for these coatings. The low-Cr samples are significantly closer to the desired Cr:W ratio than the high-Cr content samples. However, there is relative consistency within each group. In both groups, the oxygen contamination is significantly less than most of the samples produced in Sec. 3.2. Yet, there does not seem to be a clear trend between the contamination and the deposition conditions. There does appear to be a significant decrease in the films' Co-content[13] with increased Cr-content and increased temperature. But, this is not the case; the reduced Co-content is consistent with the reduced W and C content.

[12]These two compositions were chosen based on the results in Sec. 3.2.2. The low-Cr content (Cr:W = 0.5:1) samples should be below the threshold, and form "solid-solutions." The high-Cr content (Cr:W = 3:1) samples are well above the structural transformation.

[13]In prior studies, a pure WC target was used to deposit the coatings. However, for this part of the study a composite WC-Co target was used. This composite target contained 6 wt. % of cobalt.

Table 3.7: EDS results of the CrN-WC thin films created by varying the growth temperature, deposited on Si.

Sample ID	T_{growth} [°C]	Target Cr:W Ratio	Actual Cr:W Ratio	Cr	W	C	Co	N	O
Low-Cr content									
H1001	66	0.5:1	0.4:1	9.4	24.1	8.2	10.4	44.5	3.4
H1003	180		0.5:1	12.6	24.9	5.2	9.5	45.2	2.5
H1005	250		0.35:1	9.4	27	6.5	8.3	45.2	3.7
H1007	400		0.75: 1	18	23.9	4.3	7.7	44.3	1.9
High-Cr content									
H1002	75	3:1	4.2:1	33.1	7.9	5.5	3.7	46.5	3.3
H1006	170		5:1	34.7	6.9	3.7	3	48.4	3.4
H1004	270		4.1:1	34.1	8.31	3.5	3.6	46.7	3.8
H1008	390		4.9:1	36.2	7.4	1.8	3	48.4	3.2

Continuing with the examination of the chemical composition, these coatings were subjected to examination via XPS[14]. Looking at Fig. 3.33, there are obvious differences between the samples grown at different temperatures. While the types of bonds present do not significantly change, there are changes in the relative amounts of bonds present in the samples. This occurs for both high- and low-Cr content films.

Moving onto the tungsten spectra (Fig. 3.34), there are no significant differences between the samples grown at different temperatures. However, there is some differences between the two sets of samples. At low-Cr content, there appears to be two different carbide states (W_2C and WC), with relatively equal amounts of bonding. However, with the high-Cr samples, the two carbides remain, but one (WC) is significantly stronger than the other (W_2C). In other words, at low-Cr, there are two carbides present in equal amounts; at high-Cr, the two carbides are still there, but there is more of the one than the other. There is no significant evidence of other bonding states in the tungsten spectra.

Within Fig. 3.35, the types of Cr bonds do not vary; primarily, chromium is bonded to nitrogen and oxygen. However, there are some changes in the relative amounts. At low-Cr content (Fig. 3.35(a)-(d)), most of the chromium is bound in two different nitride states; this is most likely CrN and Cr_2N. At high-Cr content, the chromium nitrides remain, but an oxide is added to the mix. This can be confirmed with the N1s (Fig. 3.36) and O1s (Fig. 3.37).

In summary, the low-Cr content samples have primarily WC, W_2C, CrN, and Cr_2N bonds. There is some evidence of metal oxide (probably CrO_x) and possibly some free-carbon, but these are relatively minor. At high-Cr content, the tungsten bonding moves primarily to WC. Chromium remains with two nitrides, but the oxide bonding becomes much more significant. And, as with the low-Cr samples.

[14]All spectra were taken after 3 min of surface cleaning via 1kV Ar-ion sputter-etching.

There does not appear to be any free-carbon in these high-Cr samples. From these results, temperature does not seem to significantly affect the bonding structure of the thin films. The primary driver for changes is the relative amounts of material present.

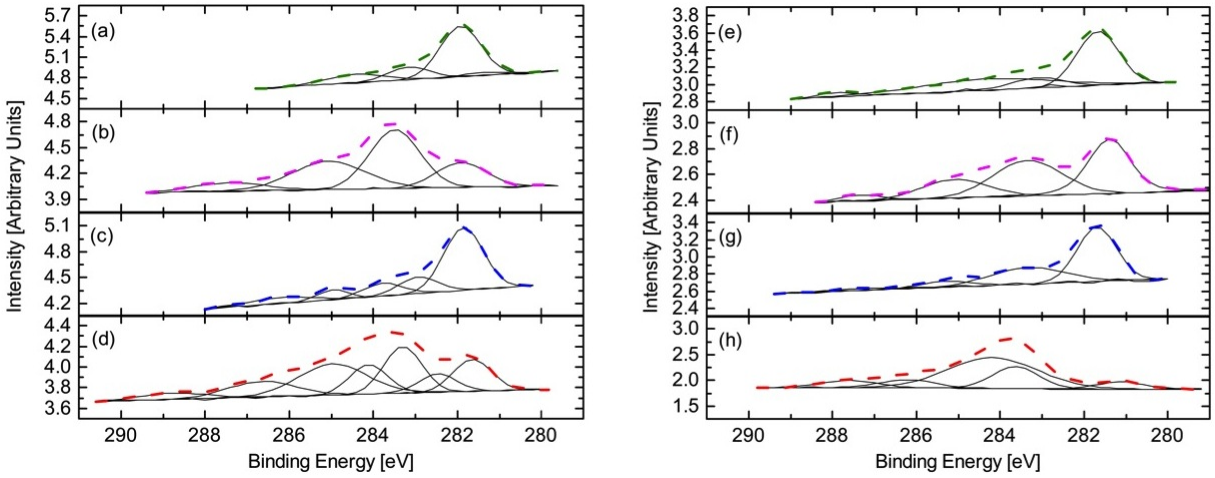

Figure 3.33: C1s spectra for the CrN-WC coatings deposited at various temperature. The spectra on the left are from the Cr:W = 0.5:1 samples, with (a) 400 °C, (b) 250 °C, (c) 180 °C, and (d) No External Heating (NEH). Similarly, the spectra on the right are from the Cr:W = 3:1 samples, with (e) 390 °C, (f) 270 °C, (g) 170 °C, and (h) NEH. The solid lines are the deconvoluted peaks used for fitting the original data (dashed lines).

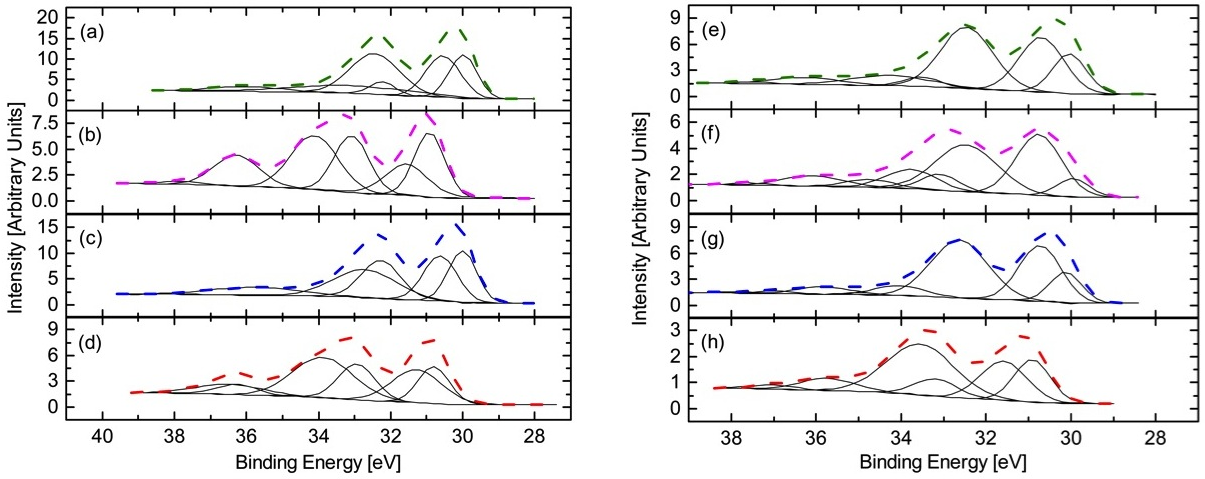

Figure 3.34: W4f spectra for the CrN-WC coatings deposited at various temperature. The spectra on the left are from the Cr:W = 0.5:1 samples, with (a) 400 °C, (b) 250 °C, (c) 180 °C, and (d) NEH. Similarly, the spectra on the right are from the Cr:W = 3:1 samples, with (e) 390 °C, (f) 270 °C, (g) 170 °C, and (h) NEH. The solid lines are the deconvoluted peaks used for fitting the original data (dashed lines).

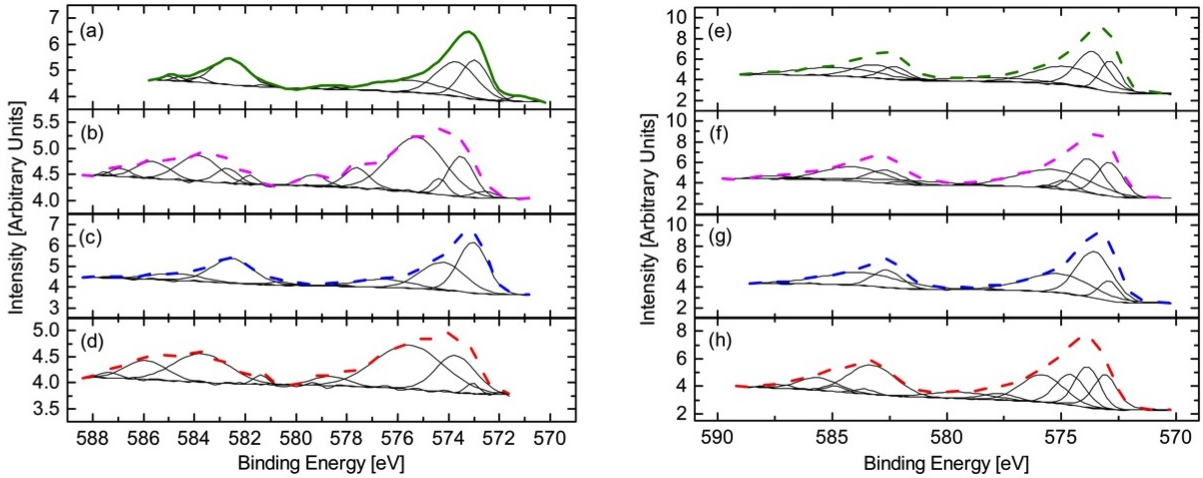

Figure 3.35: Cr2p spectra for the CrN-WC coatings deposited at various temperature. The spectra on the left are from the Cr:W = 0.5:1 samples, with (a) 400 °C, (b) 250 °C, (c) 180 °C, and (d) NEH. Similarly, the spectra on the right are from the Cr:W = 3:1 samples, with (e) 390 °C, (f) 270 °C, (g) 170 °C, and (h) NEH. The solid lines are the deconvoluted peaks used for fitting the original data (dashed lines).

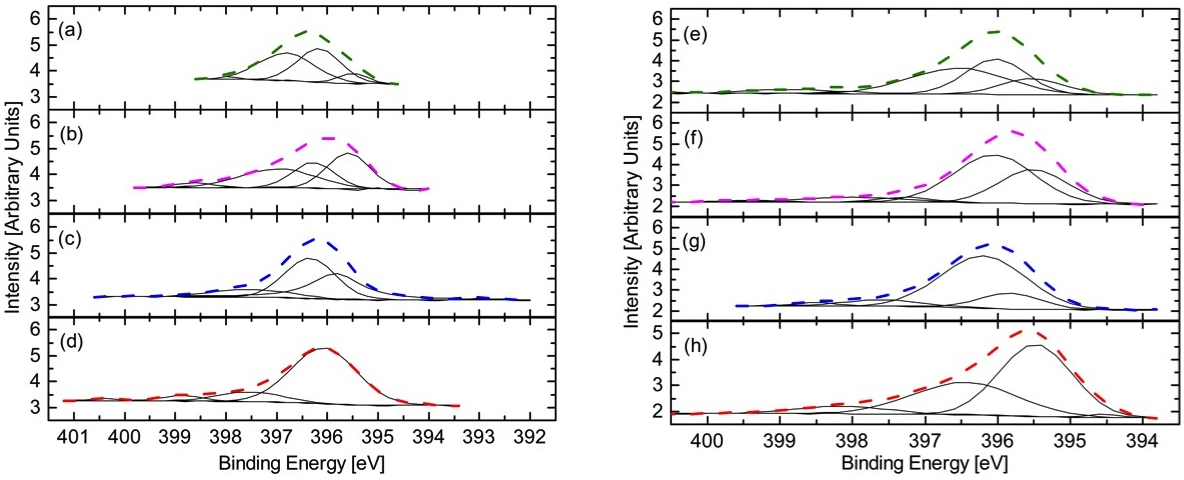

Figure 3.36: N1s spectra for the CrN-WC coatings deposited at various temperature. The spectra on the left are from the Cr:W = 0.5:1 samples, with (a) 400 °C, (b) 250 °C, (c) 180 °C, and (d) NEH. Similarly, the spectra on the right are from the Cr:W = 3:1 samples, with (e) 390 °C, (f) 270 °C, (g) 170 °C, and (h) NEH. The solid lines are the deconvoluted peaks used for fitting the original data (dashed lines).

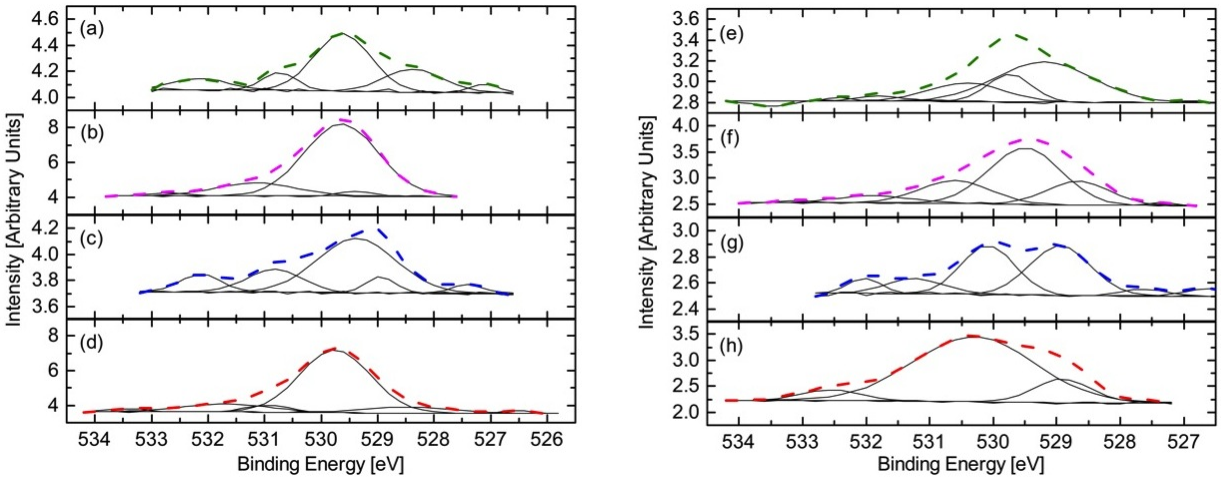

Figure 3.37: O1s spectra for the CrN-WC coatings deposited at various temperature. The spectra on the left are from the Cr:W = 0.5:1 samples, with (a) 400 °C, (b) 250 °C, (c) 180 °C, and (d) NEH. Similarly, the spectra on the right are from the Cr:W = 3:1 samples, with (e) 390 °C, (f) 270 °C, (g) 170 °C, and (h) NEH. The solid lines are the deconvoluted peaks used for fitting the original data (dashed lines).

With the changes in the chemical structure clearly explained, crystallographic structure is next up. XRD results for the various coatings are shown in Fig. 3.38. Quantitative data cannot be extracted from this spectra; the peaks are too weak, and relatively wide. However, there is some qualitative information to be gleaned.

With the low-Cr content films (Fig. 3.38(a)-(d)), there appears to be a temperature related structural transformation. At low deposition temperature, the diffractogram is as expected: a broad WCN-like peak (similar to the low-Cr coating in Fig. 3.21(e)). However, with elevated growth temperature, this broad peak sharpens and a secondary peak at $\sim 42^{\circ}$ appears. This pattern is more consistent with higher Cr-content films, and may be evidence of the transformation from "solid-solution" to nanocomposite structure.

High-Cr content films (Fig. 3.38(e)-(h)) show the nanocomposite structure (as observed in Fig. 3.21(a)-(d)). However, there does seem to be a shift in the preferred orientation. At low temperature, the main peak (i.e. sharpest, with highest intensity) is consistent with (111) orientation. As temperature increases, this peak weakens and appears to broaden. In contrast, the (200) peak grows in intensity and sharpness. This may be indicative of densification. (200) crystallites have a higher packing density than (111) crystallites.

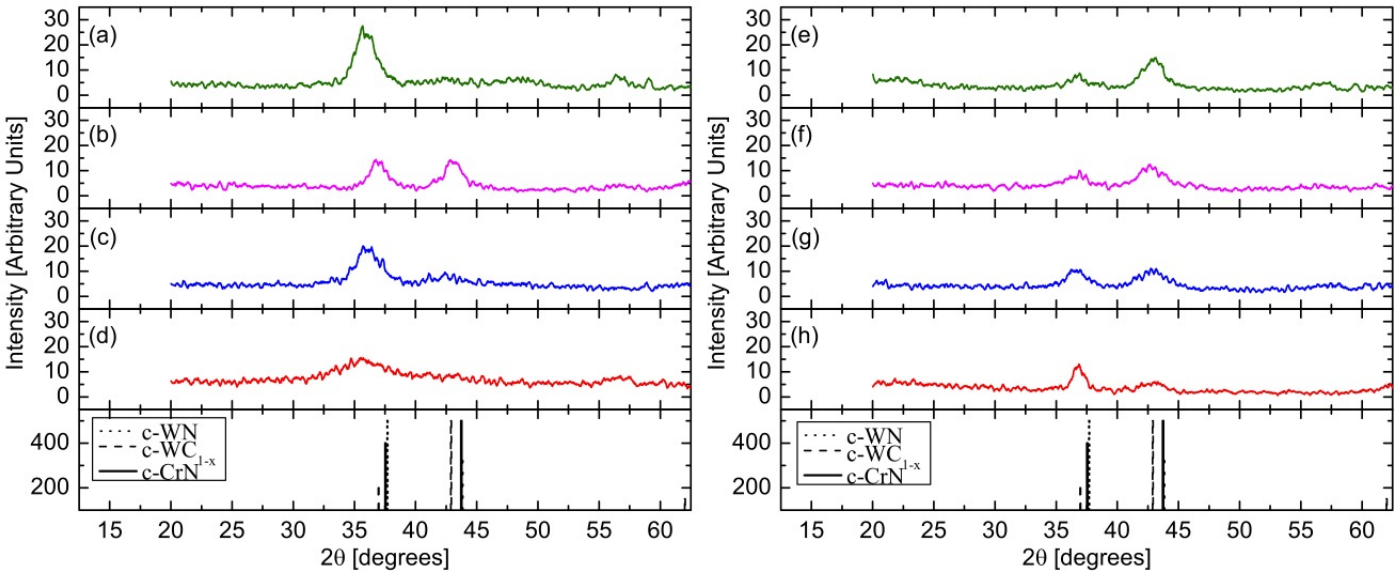

Figure 3.38: XRD spectra of the CrN-WC thin films deposited at different growth temperatures onto Si substrates. The low-Cr content samples were deposited at (a) 400 °C, (b) 250 °C, (c) 180 °C, and (d) NEH. The corresponding high-Cr content samples are (e) 390 °C, (f) 270 °C, (g) 170 °C, and (h) No External Heating (NEH).

Moving onto the microstructure of the coatings. There are several bits of information that can be gleaned from Fig. 3.39. For example, the film thicknesses can be determined from the cross-sectional HR-SEM micrographs (insets within the figure); these are listed in Table 3.8. All coatings are less than 500 nm thick. The most significant deviations occur at higher temperatures. This is related to the increased adatom mobility, and shorter lifetimes, which occur at higher temperatures compared to low temperature deposition[15].

Table 3.8: Thickness of CrN-WC thin films created by varying the growth temperature, deposited on Si.

Sample ID	T_{growth} [°C]	Thickness [nm]	R_a [nm]	R_{RMS} [nm]
Low-Cr content				
H1001	66	469	4.9	6.1
H1003	180	362	7.8	9.6
H1005	250	346	5.0	6.6
H1007	400	226	1.9	2.4
High-Cr content				
H1002	75	464	4.6	5.3
H1006	170	381	5.3	6.7
H1004	270	307	7.2	8.5
H1008	390	329	2.6	3.3

[15]The deposition rates were initially calibrated at low temperature.

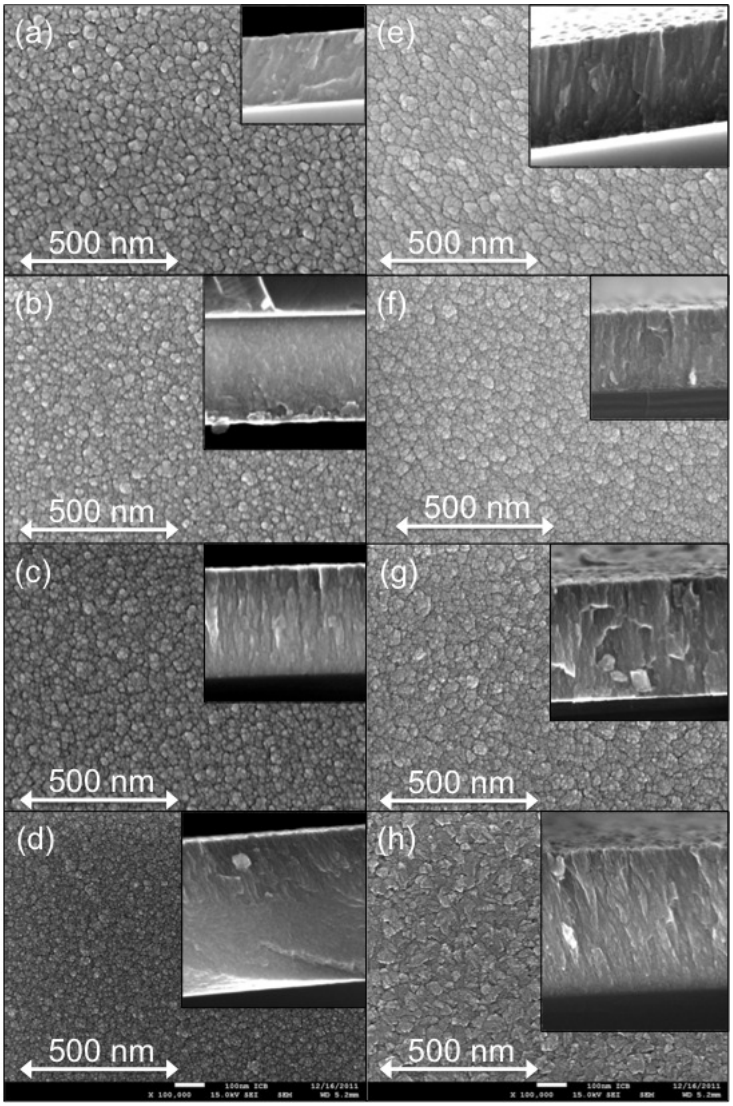

Figure 3.39: HR-SEM micrographs of the CrN-WC surfaces (with insets of the cross-sections), deposited at different growth temperatures onto Si substrates. The low-Cr content samples were deposited at (a) 400 °C, (b) 250 °C, (c) 180 °C, and (d) NEH. The corresponding high-Cr content samples are (e) 390 °C, (f) 270 °C, (g) 170 °C, and (h) No External Heating (NEH).

Looking at the surface morphology, there are no significant differences within the groups, i.e. all the low-Cr content samples have a similar surface morphology. The same can be said for the high-Cr samples. However, when comparing the two groups, there is an observable difference: the high-Cr samples appear to have a more faceted surface compared to their low-Cr counterparts. This may be due to different

growth modes for the two sets of samples. For low-Cr power, it is expected there would be less ion-effects than at high-Cr power. This appears to correspond to the observed microstructure in the cross-sectional HR-SEM insets. At low-Cr power, the films appear denser, with less defined columnar growth than at high-Cr content. Grains also appear larger in the high-Cr films. Relating this to the extended MDT structural zone model, the low-Cr content films are clearly within zone 2. The high-Cr coatings appear to be at or near the transition to zone 3. The grains are larger, with some amount of faceting on the surface. Additionally, the AFM results (Fig. 3.40) are listed in Table 3.8. For the low-Cr samples, there seems to be a trend of decreasing roughness after the intermediary temperature of 180 °C. With the high-Cr samples, the trend is opposite. Roughness increases until an intermediary temperature of 270 °C, and then drops. In both cases, the lowest roughness parameters are reached at maximum growth temperature ($\sim$ 400 °C).

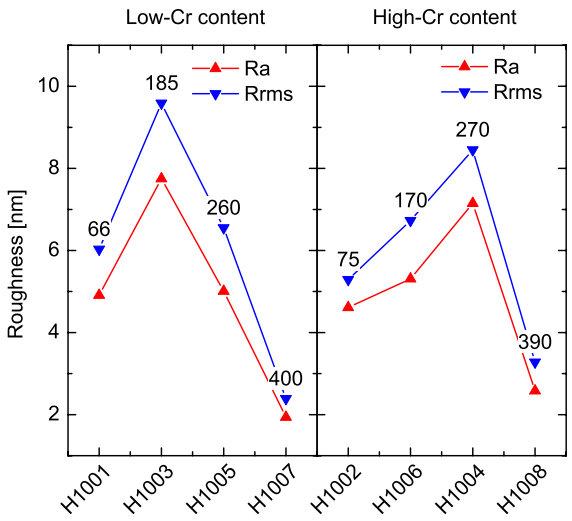

Figure 3.40: Surface roughness parameters of the CrN-WC thin films, as measured across a 5 x 5 μm^2 area by AFM.

Changing gears to stress measurements, Fig. 3.41 shows the stress development across the different coatings. While there are no obvious trends in the data (for either case), it is clear that the stress state is significantly more advanced

than the coatings developed at low deposition temperature. However, it is difficult to make a direct comparison of the stress states in these thin films to the stress states of the coatings developed at low deposition temperature. The average stress within a coating can be significantly affected by the coating thickness. The thickness of these thin films is only $\sim$ 10 % of the coatings grown at low-deposition temperature. However, it is still desirable for the higher stress states of the CrN-WC coatings deposited at high-temperature to carry over to the nanoindentation results.

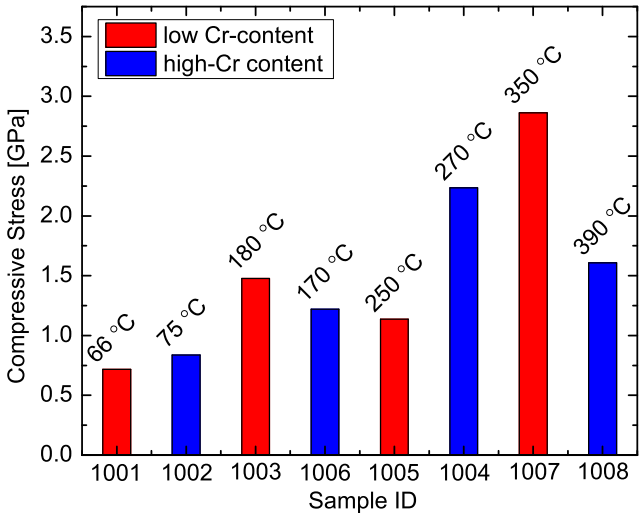

Figure 3.41: Stress results obtained by wafer curvature for the CrN-WC thin films deposited at various temperatures.

Using nanoindentation, Fig. 3.42, the mechanical properties are measured. Once again, there is no clear cut trend. For the low-Cr coating, the H (E) values are 11.3 GPa (267 GPa), 15.2 GPa (236 GPa), 15.6 GPa (265 GPa), and 12 GPa (190 GPa) for the 400 °C, 250 °C, 180 °C, and NEH samples, respectively. For the low-Cr content samples, H^3/E^2 hovers around 0.046 GPa; this is similar to NbB_2 in Table 1.1. However, the moduli of these CrN-WC coatings indicate a significantly more ductile coating. The high-Cr coating values of H (E) are 13.7 GPa (253 GPa), 14.1 GPa (246 GPa), 11.8 GPa (214 GPa), and 12.6 GPa (212 GPa) for the 390 °C,

270 °C, 170 °C, and NEH samples, respectively. H^3/E^2 is approximately 0.04 GPa for the high-Cr samples; for comparison, Cr_3C_2 has $H^3/E^2 \sim 0.04$ GPa (Table 1.1). In either case, the results are lower than the values obtained for the CrN-WC coating in the Viability study, Sec. 3.1. Additionally, the fracture toughness (which is proportional to H^3/E^2) is significantly less than several nanocomposites listed in Table 1.3.

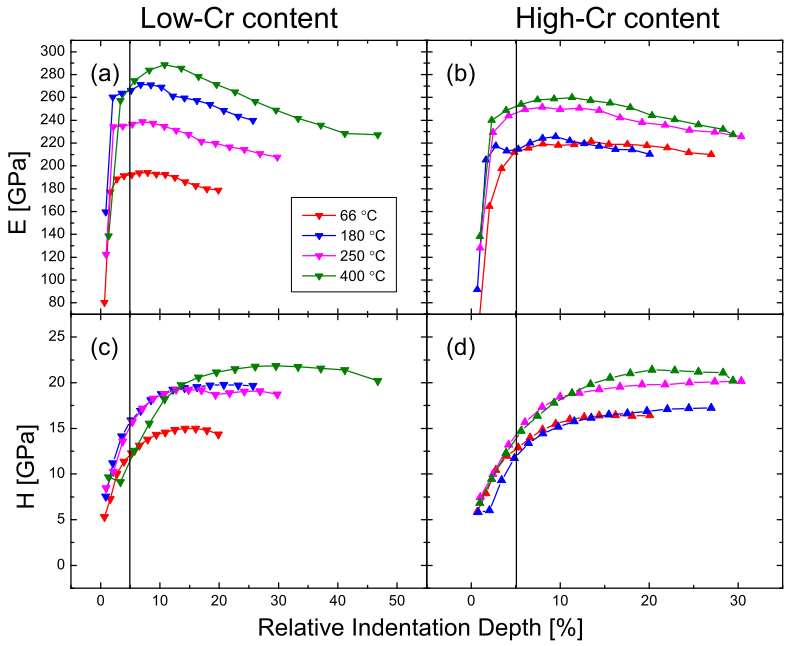

Figure 3.42: Mechanical property results from nanoindentation of the CrN-WC thin films. Panels (a) and (b) show the E for the low-Cr and high-Cr, respectively. Similarly, panels (c) and (d) are the H results for the low-Cr and high-Cr thin films, respectively. To avoid substrate effects, the Hardness and Young's Modulus are evaluated at 5 % of the sample thickness.

3.3.2 Nanocrystalline Diamond Deposition on CrN-WC Thin Films

Using the same deposition parameters as the viability study (see Table 2.1), growth of nanocrystalline-Diamond (nc-D) coatings was attempted on the CrN-WC thin films, grown at various temperatures. As seen in HR-SEM micrographs of

Fig. 3.43, there was some success. However, of the eight thin films grown at various temperatures, only three high-Cr content samples showed any nc-D growth. Additionally, only the middle temperature coating at 270 °C developed a complete coating. The other two samples (deposited at 390 °C and NEH), show nc-D growth, but very little. Raman spectroscopy was used to confirm the presence of nanocrystalline-Diamond, Fig. 3.44.

While not the traditional Raman spectra (as shown in Fig. 3.9), there are certain features which indicate the presence of nc-D. Specifically, the peaks at 1125 cm^{-1} and 1442 cm^{-1} are associated with polyacetylene chain fragments [199, 200], and are typical in a nc-D spectrum. Additionally, the peaks in the vicinity of 1380 cm^{-1} may be due to distorted sp^2-bonded clusters [201]. However, it is key to note that all these peak locations are shifted to lower wavenumbers. This may be due to internal tensile stress in the nc-D "film."

It is not clear why the nc-D does not nucleate on these CrN-WC thin films as well as it did during the viability study, Sec. 3.1.2. One possible answer is the inclusion of cobalt in the coating from the composite WC-Co sputtering target. This may explain why the growth only occurred on high-Cr samples; low-Cr samples have a higher amount of Co incorporation (Table 3.7). Cobalt is a known catalyst for graphitic carbon growth. But, while the Raman spectra does show graphitic elements (i.e. the peak at $\sim$ 1590 cm^{-1}), no complete carbon film is observed. The HR-SEM images of Fig. 3.43 clearly show the plasma-etched surface of the CrN-WC coating under the nanodiamond particles.

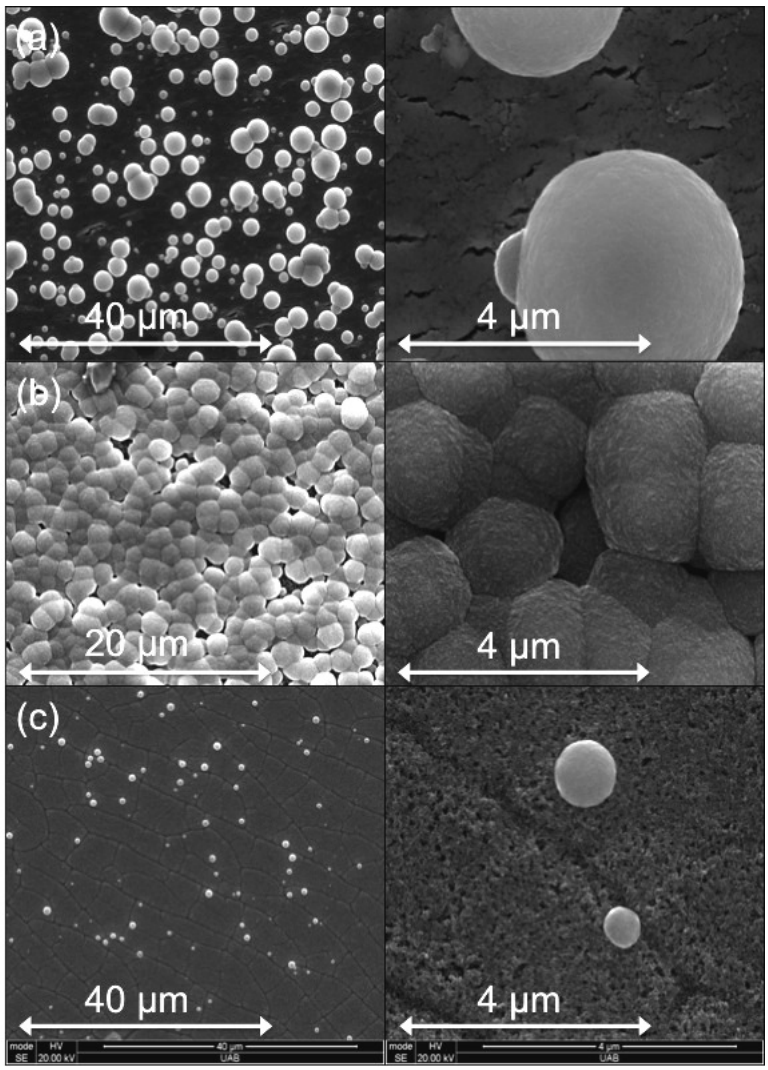

Figure 3.43: All CrN-WC thin films were subjected to MPCVD of nc-D. However, only the high-Cr sample grown at (a) 390 °C, (b) 270 °C, and (c) NEH show any appreciable nc-D growth. These HR-SEM micrographs were taken using the FEI Quanta 650, at low- (left) and high-magnification (right).

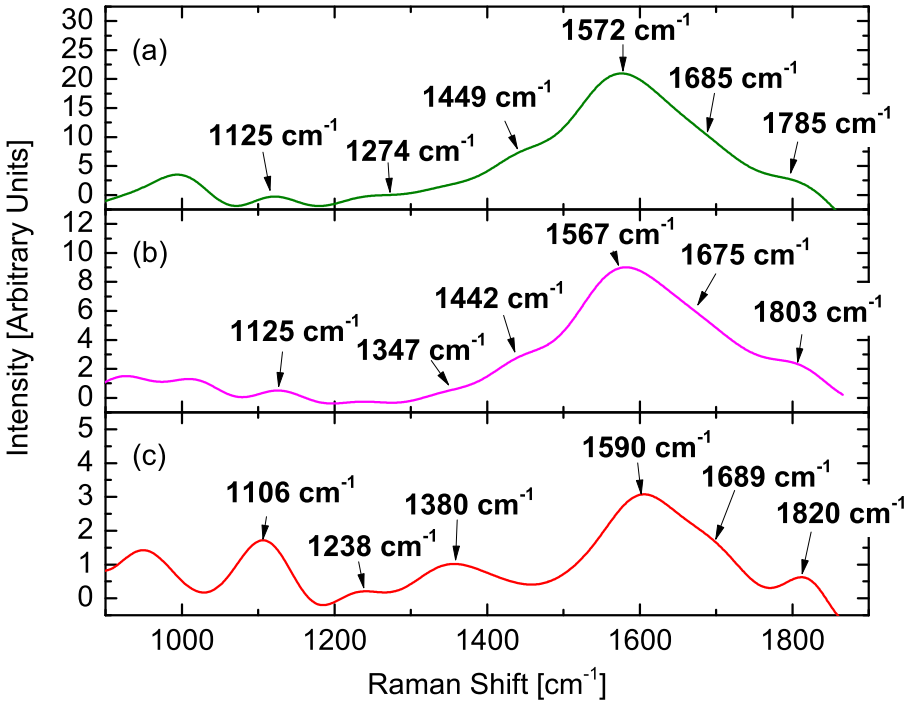

Figure 3.44: Raman spectroscopy results from nc-D coatings grown on three high-Cr content samples: (a) 390 °C, (b) 270 °C, and (c) No External Heating (NEH).

3.3.3 Coatings at High Temperature

From the variable temperature study described in Sec. 3.3.1, it was decided to use the maximum growth temperature for subsequent coatings (thickness ~ 1 μm). For this part, three constituent coatings (CrN, WC, and WCN) were grown to study the effects of high-temperature growth on these standard materials. Afterwards, six different compositions of CrN-WC were grown at the same high temperature. The deposition conditions are listed in Table 3.6, and the chemical composition (as determined by EDS) is listed in Table 3.9.

Looking at the constituent coatings, it is very easy to see that the atomic concentration of Cr is twice that of N in the CrN coating; this may indicate that Cr_2N as the primary phase. A true WC coating would have equal atomic concentrations of W and C. However, that is not the case here. Here, W:C is ~ 1.5. Typically, this would lead to the choice of W_2C as the primary phase. However, it may be possible for multiple phases of WC (such as WC_{1-x}, WC_x, and W_xC) may be present in either crystalline or amorphous form.

With regards to the WCN coating, the total atomic concentration of C and N is equivalent to the amount of W in the system. Therefore, this system could be either a solid solution of W-C-N, or a composite of W-N and W-C bonds. EDS analysis does not reveal any information on the bonding structure of the coating.

Moving onto the CrN-WC coatings, there are some significant differences between the targeted and actual Cr:W ratio for many of the CrN-WC coatings. In the previous investigation of samples deposited at low-temperature (Sec. 3.2), the actual Cr:W ratios were relatively close to the target Cr:W ratios. More importantly, the order of low-Cr to high-Cr coatings was not changed. Here, the actual Cr:W ratios are significantly different, AND the order from low-Cr to high-Cr content is skewed. As such, if the samples were referenced by their target Cr:W rather than their actual Cr:W (as was done in Sec. 3.2), there may be some

confusion and it is possible important trends in the data may be missed. Therefore, for this section (Sec. 3.3.3), the samples will be identified by their actual Cr:W ratios.

Table 3.9: EDS results of the CrN-WC coatings created by varying the growth temperature, deposited on Si.

Composition	Target Cr:W Ratio	Actual Cr:W Ratio	Cr	W	C	Co	N	O
Constituent Coatings								
CrN			63.1				31.5	5.4
WC				50.5	33.6	12.5		3.35
WCN				44.2	24	8.25	20.2	3.35
CrN-WC Compositions								
CrN-WC	0.6:1	0.75:1	20.2	27.1	4.8	5.6	42.4	
CrN-WC	0.75:1	0.34:1	11.8	35	9.2	7.5	36.6	
CrN-WC	1:1	1.4:1	26.4	19.2	2.0	3.9	48.7	
CrN-WC	1.25	0.5:1	15.5	31.3	7.9	7	38.3	
CrN-WC	1.5:1	0.74:1	19.7	26.7	5.4	5.8	42.5	
CrN-WC	2:1	1.1:1	25.8	23.7	7.9	5.8	37.1	

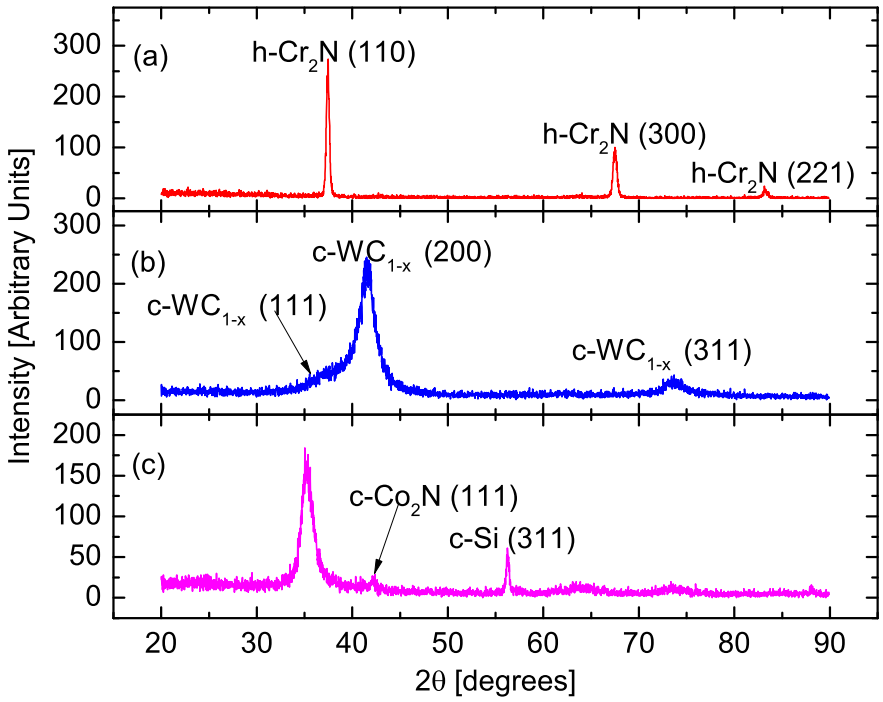

Figure 3.45: X-ray diffractogram for the constituent coatings of the CrN-WC system, grown at high temperature: (a) CrN, (b) WC, and (c) WCN.

Previously, at low-temperature, only the WC and WCN constituent coatings were deposited, during the viability study (Sec. 3.1). Looking back to Fig. 3.1, there are some obvious differences in the crystallographic nature of the high-temperature coatings compared to the low-temperature coatings. At low-temperature (Fig. 3.1), the WC coating showed a broad (111) peak at 41.8°, a sharper (200) peak at 45.3°, and a small, broader (311) peak at 73.3°; Debye-Scherrer analysis (Eqn. 2.6) yields an average crystallite size of 4.2 nm. With the high-temperature WC coating (Fig. 3.45(b)), the overall shape is very similar, with the (111), (200), and (311) peaks at 38.7°, 41.6°, and 74.4°, respectively. These are relatively significant shifts to lower diffraction angles. This may be due to stress. Additionally, the peak widths are narrower which leads to an average crystallite size of 6.2 nm. While this analysis

assumes a single-phase, it is possible there are multiple crystalline phases in this sample. One possibility is a combination of c-WC_{1-x} and c-W_2C. As such, the peak widths would be narrower, and the average crystallite size would be larger.

However, the most striking change is found when comparing WCN coatings. At low temperature (Fig. 3.1(c)), WCN showed only a broad peak centered $\sim 35°$. This coating may have consisted of several nanocrystalline phases. However, subsequent XPS analysis revealed a primarily WCN structure. As such, the average grain size was ~ 1.6 nm. Using an elevated growth temperature of ~ 400 °C, the WCN coating transforms from a nearly amorphous structure, with a single, broad peak to a crystalline structure, with multiple peaks at 35.1°, 63.4°, and 73.2°. Here, the average crystallite size is 9.3 nm. As with the WC structure in Fig. 3.45(b), it is possible there are multiple crystalline phases present in this sample. One glaring phase is crystalline Co_2N, with a peak located at 42.5°.

While it is not possible to compare the high-temperature CrN peak to a low-temperature cousin, deposited in the same UHV chamber, useful information can still be gleaned from the diffractogram (Fig. 3.45(a)). The main peaks correspond to h-Cr_2N. The (110), (300), and (221) peaks are located at 37.4°, 67.5°, and 83.6°. The sharp peaks indicate an average grain size significantly larger ($\sim$ 62.6 nm) than the other constituent coatings (b) WC and (c) WCN.

In Fig. 3.46, the diffractograms for the various CrN-WC coatings are presented. Despite the proximity of their Cr:W ratios, there are some notable differences. Starting with the highest Cr-content, Cr:W = 1.4:1, shown in Fig. 3.46(a), there are discernible peaks at 36.2°, 42.5°, 61.6°, and 73.5° which correspond to the (111), (200), (220), and (311) peaks, respectively. There is significant overlap between c-WC_{1-x} and CrN. As such, it is impossible to properly index the structure. Still, this particular set of peaks is typical of the B1 (NaCl) fcc structure. Additionally, the overlap prevents proper estimation of the grain size.

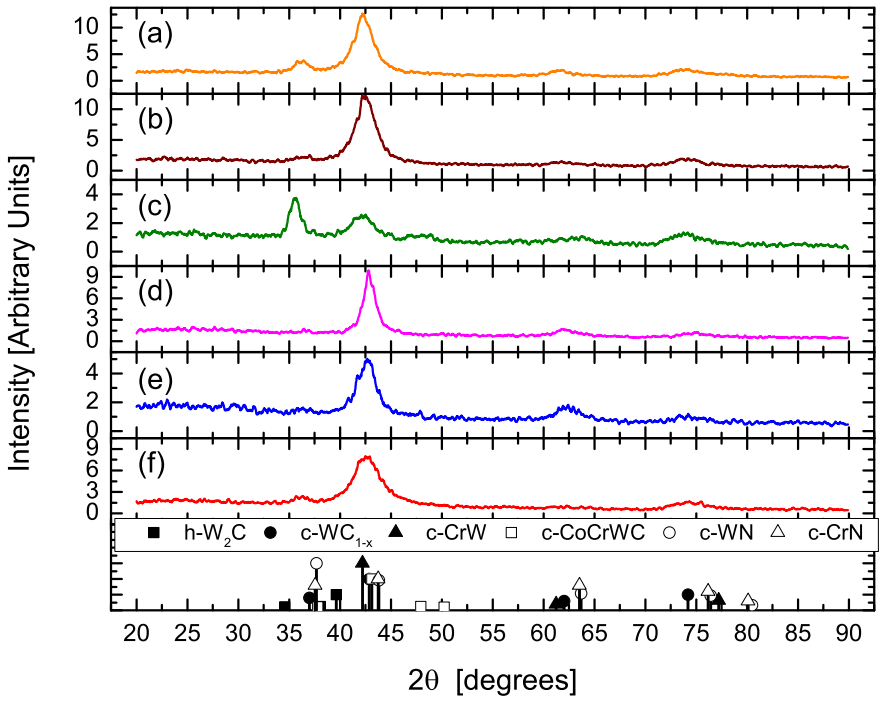

Figure 3.46: X-ray diffractogram for the CrN-WC system, grown at high temperature. The panels are Cr:W = (a) 1.4:1, (b) 1.1:1, (c) 0.75:1, (d) 0.74:1, (e) 0.5:1, and (e) 0.34:1.

However, using the (200) peak, it is possible to set a lower limit on the grain size[16]. As such, the FWHM is 2.72°, and the lower limit on the grain size is 4.2 nm.

Continuing down from high-Cr to low-Cr, the next sample is Cr:W = 1.1:1, Fig. 3.46(b). The only significant difference between this spectra and the higher Cr content sample is the weakening of the peak $\sim 36.5°$. The next diffraction pattern (Fig. 3.46(c)) is significantly different from the prior two spectra. While the peak positions do not significantly change, there is a change in the relative intensities. For the 1.4:1 sample, the (111) peak at 36.5° is only about 1/4 the size of the (200) peak at 42.5°. Here, with the 0.75:1 sample, the (111) peak is now stronger, and narrower, than the (200) peak. In addition, there is now a weak, broad peak at 48°. This may be the result of the Co-binder in the WC target.

[16]If the peak consists of multiple phases, these constituent phases would necessary have smaller peak widths. The smaller the FWHM, the larger the grain size.

With the next sample, the Cr:W ratio is very similar to the previous sample, but the diffraction pattern is very different. With the Cr:W = 0.75:1 sample in Fig. 3.46(c) there is a very strong (111) peak, which is dominate over the (200). Here, with the Cr:W = 0.74:1 sample in Fig. 3.46(d), the (111) peak is practically nonexistent and the (200) dominates. Looking at the entire collection of diffractograms, it is possible the 0.75:1 sample (Fig. 3.46(c)) is an outlier. This is supported by plotting (111)/(200) against the composition, Fig. 3.47.

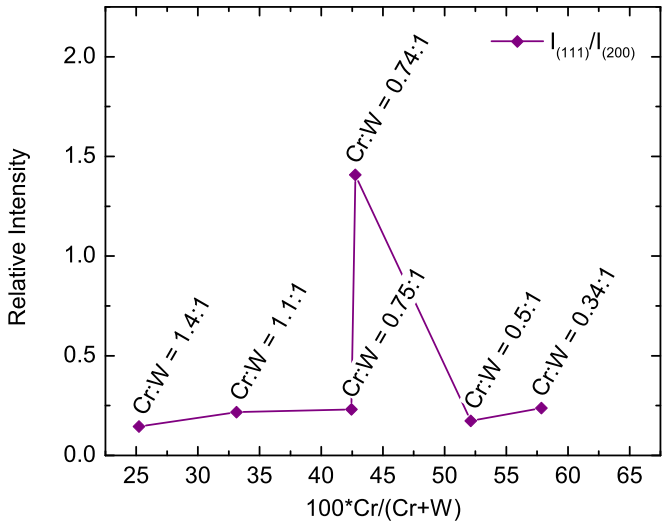

Figure 3.47: Relative intensities of the (111) and (200) peaks against the composition of the CrN-WC coatings, deposited at high-temperature.

With treating the 0.75:1 sample as an outlier, a trend does emerge. As the Cr-content decreases, the (111) peak becomes *slightly* stronger compared to the (200) peak. This appears to be the only clear trend in the XRD data. Closer examination of the remaining samples, Cr:W = 0.5:1 (Fig. 3.46(e)) and Cr:W = 0.34:1 (Fig. 3.46(f)), does not reveal any additional information.

Obviously, XRD does not tell the whole story. Another component to this tale is the coating microstructure. As before, the constituent components come first, Fig. 3.48. Each of the three samples have three images; starting on the right is a

secondary electron image of the surface. This is followed by a secondary electron image of the cross-section. The final image is also of the cross-section, but it is collected via back-scattered electrons. This offers another glimpse into the microstructure, and is very useful for dense samples which may not show much detail with secondary electrons.

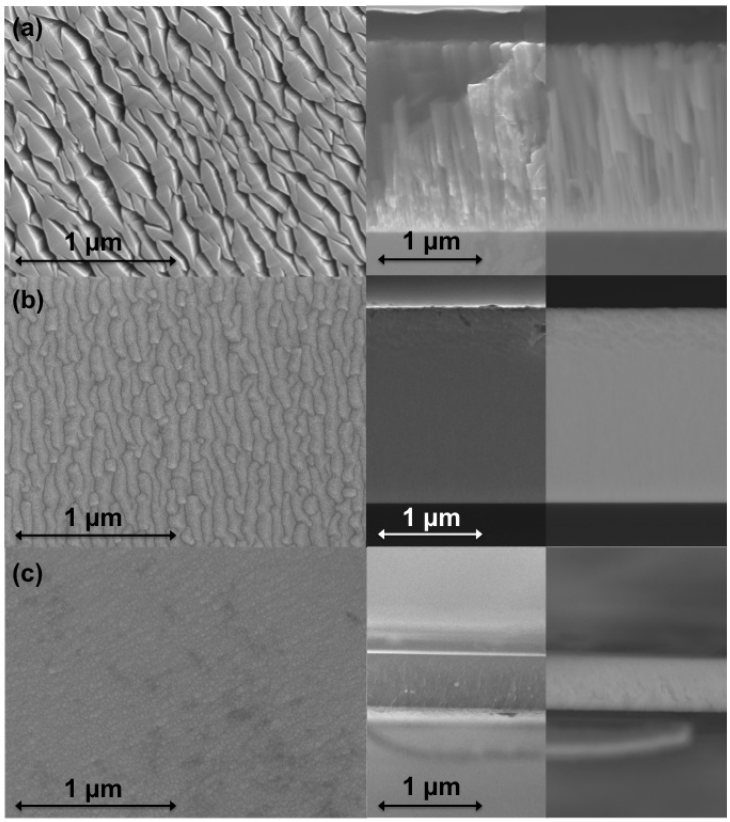

Figure 3.48: HR-SEM micrographs of the constituent coatings: (a) CrN, (b) WC, and (c) WCN. Moving across, from left to right, the samples' microstructure is revealed via secondary electron images of the surface topography and the cross-section. An additional back-scattered image further illuminates the sample cross-sections.

The CrN coating (Fig. 3.48(a)) appears with a relatively porous microstructure. The growth is columnar, traversing the full thickness of the coating. However, the columns do appear to taper. Additionally, the grains are relatively large and have flat tops, as evidenced by the cross-sectional images. With a growth temperature of $\sim$ 400 °C, the generalized temperature is $\sim$ 0.32. Despite this, the

growth comes across as zone 1 growth. Another feature of zone 1 growth is tensile stress. As shown in Fig. 3.49, this CrN coating shows tensile stress, albeit at a very low value (32 ± 1 MPa).

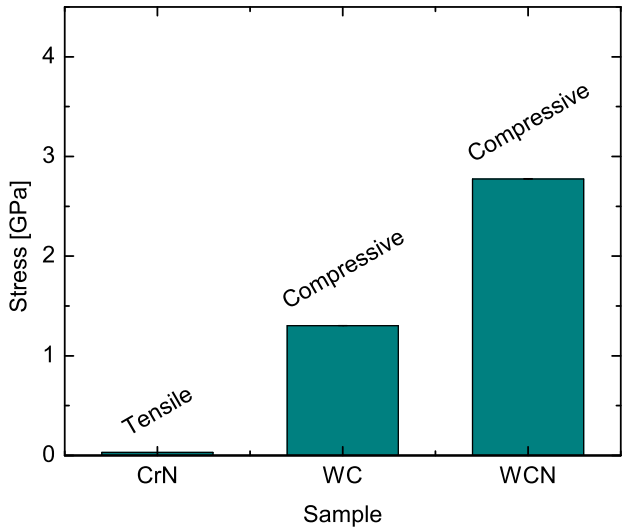

Figure 3.49: Stress within the constituent films. The CrN coating shows tensile stress, while the stress within the WC and WCN coatings is compressive.

Moving to Fig. 3.48(b), the WC coating has much smaller grains, and significantly fewer voids. This matches well with the very dense microstructure presented in the cross-sectional views. The melting temperature of WC is significantly higher than that of CrN. As a result, the generalized temperature is reduced to ~ 0.12. Combining this with the dense film observed in the cross-sectional images, the growth mode falls within zone T. As expected with zone T (and higher) growth, the stress (Fig. 3.49) becomes compressive.

Also, it may be interesting to note that there is a change in the microstructure near the surface of the coating (within ~ 500 nm of the surface). It appears to have more structure than the majority of the coating. It may be due to a change in the phase (i.e. formation of an additional phase in the coating, such as W_2C), and/or increased porosity. In this regard, the micrographs are inconclusive.

The final set of micrographs (Fig. 3.48(c)) completes the set of constituent coatings: WCN. This coating is the thinnest of all the coatings produced during this part of the study. It is a direct result of WC target poisoning. However, despite the relative thinness of the coating, the surface topography is fairly smooth with a significant decrease in the observable grain size. This holds true in the cross-sectional images as well. While dense, there is some evidence of columnar growth, but with smaller grain sizes. Assuming a similar generalized temperature as WC, this coating is also in zone T. However, the evidence of columnar growth places it closer to the transition between zone T and zone 2 than the WC coating.

While it is relatively certain that the coating microstructure affects the stress development, there is no clear correlation between stress development and film growth modes within the extended MDT model. In other words, despite the higher compressive stress level within the WCN coating and the higher energy growth mode, it may be inappropriate to draw a correlation between the compressive stress level and the MDT structural zone model.

This analysis can be continued with the CrN-WC coatings, with their micrographs presented in Fig. 3.50 and 3.51. The first group (Fig. 3.50) are the Cr:W = 1.4:1, 1.1:1, and 0.75:1 coatings[17]. The second group (Fig. 3.51) consists of the Cr:W = 0.74:1, 0.5:1 and 0.34:1 coatings.

Similar to Sec. 3.2.1, the melting point of CrN is used to determine the generalized temperature ($T^* \sim 0.32$). As such, zone 2 type growth is expected for these coatings. However, the first coating (Cr:W = 1.4:1, Fig. 3.50(a)), does not seem to want to cooperate. There is obvious signs of columnar growth, and the surface is as expected for zone 2 growth. But, there seems to be some evidence of recrystallization in the upper part of the coating, shown in both the secondary electron and back-scattering image of the cross-section. However, while this is a

[17]This is the "outlier" coating examined in Fig. 3.46(c)

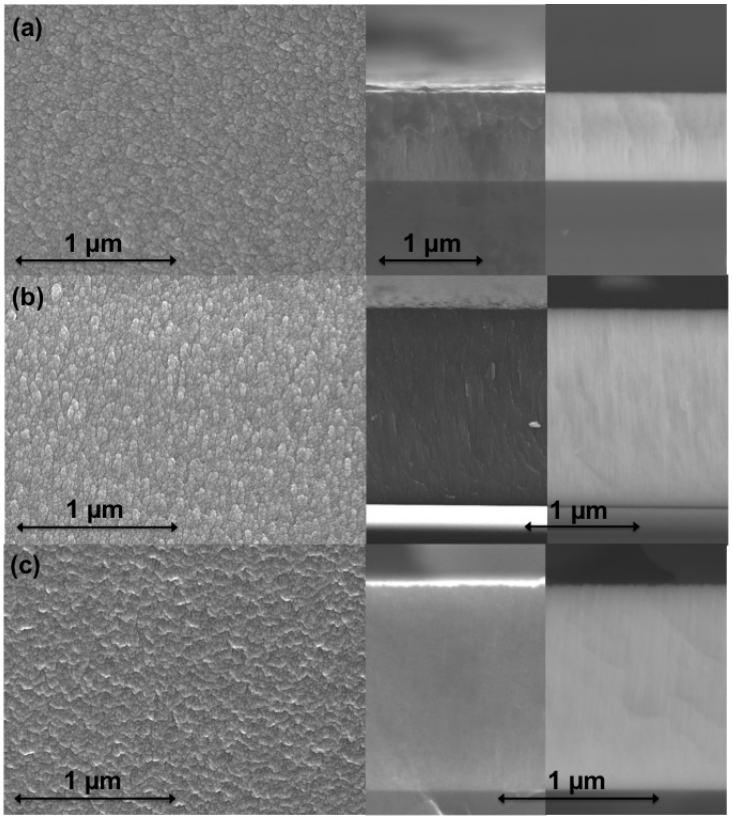

Figure 3.50: HR-SEM micrographs of the high-Cr content CrN-WC coatings, with Cr:W = (a) 1.4:1, (b) 1.1:1, and (c) 0.75:1. Moving across, from left to right, the samples' microstructure is revealed via secondary electron images of the surface topography and the cross-section. An additional back-scattered image further illuminates the sample cross-sections.

typical zone 3 feature, the other features are clearly zone 2. As such, this coating appears to be approaching the transition boundary between zone 2 and zone 3.

The next sample, Cr:W = 1.1:1 (Fig. 3.50(b)) is clearly within zone 2. The columns are dense, and extend the full thickness of the coating. There does not appear to be any evidence of recrystallization. However, the remaining sample of this set (Cr:W = 0.75:1) appears to fall in zone T. The columns extend the full thickness, and the surface is as expected, but the grain size is relatively small and the film appears more densely packed than a zone 2 coating.

Similarly, the first sample (Cr:W = 0.74:1) of Fig. 3.51(a) also appears to fall in the T zone: dense, fibrous grains. Moving to the Cr:W = 0.5:1 sample

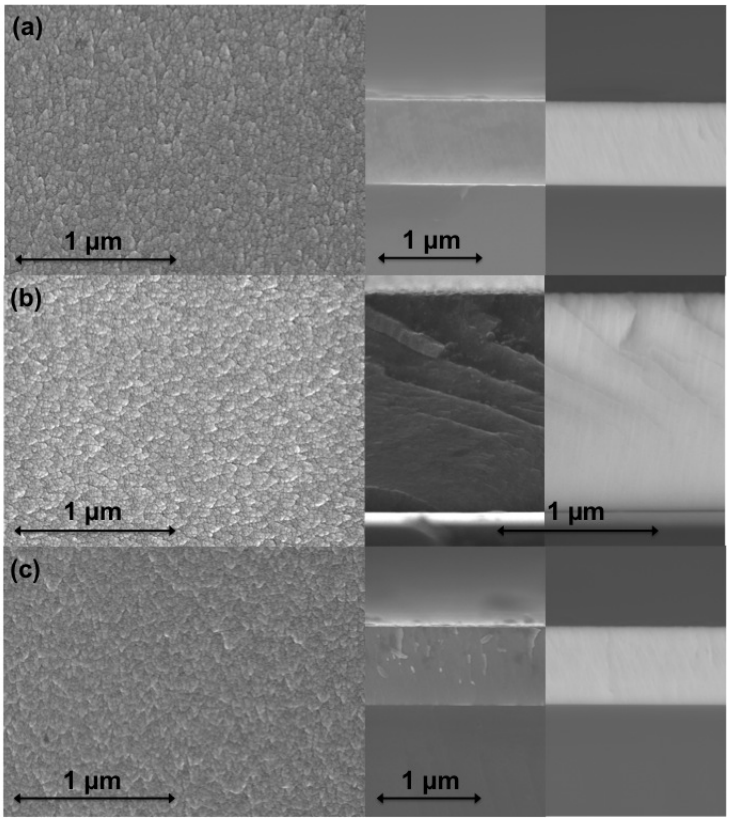

Figure 3.51: HR-SEM micrographs of the low-Cr content CrN-WC coatings, with Cr:W = (a) 0.74:1, (b) 0.5:1, and (c) 0.34:1. Moving across, from left to right, the samples' microstructure is revealed via secondary electron images of the surface topography and the cross-section. An additional back-scattered image further illuminates the sample cross-sections.

(Fig. 3.51(b)), the structure also appears dense, with fibrous grains visible in the back-scattered image. However, there is some structure visible in both the secondary and back-scattered electron images that does not clearly fall within the purview of the MDT model[18]. These appear to be breaks in the growth.

Finally, the remaining set of HR-SEM micrographs (Fig. 3.51(c)) which show the structure of the Cr:W = 0.34:1 coating. Once again, dense, fibrous grains are visible in the back-scattered image. However, there does appear to be the beginnings of normal columnar growth; specifically, this is visible in the upper part (area $\sim$ 650

[18]As stated earlier, the model is more of a guideline for predicting/analyzing growth rather than an exact model.

nm from the surface) of the secondary electron image of the cross-section. This sample may fall in the lower part of the boundary region between zone T and zone 2.

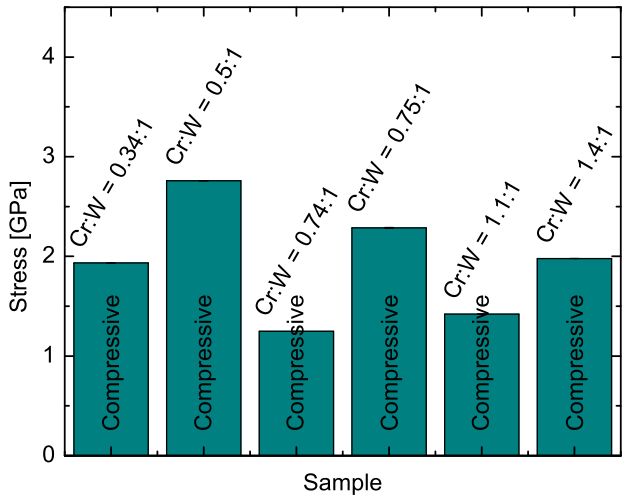

Figure 3.52: Stress within the CrN-WC coatings. While all six coatings show compressive stress, there is no clear trend between stress and composition.

With the conclusion of microstructural analysis, it is necessary to complete the stress analysis of the CrN-WC coatings. In Fig. 3.52, the compressive stresses of the different coatings are plotted for each coating. There is no obvious trend between the coating composition and the stress level. Additionally, this provides some justification for the hesitancy to link stress and growth mode. If there were a link, the highest stress would be expected to occur in the Cr:W = 1.4:1 coating. This coating was positioned near the boundary between zones 2 and 3. And the lowest stress would likewise be expected in the Cr:W = 0.75:1 coating. However, the greatest stress is found in the Cr:W = 0.5:1 coating (-2.758 ± 0.003 GPa); the lowest stress level is found in the Cr:W = 0.74:1 coating (-1.248 ± 0.001 GPa).

Finally, after discussing the coatings' chemical, crystallographic, microstructure, and stress states, the all-important mechanical properties will be exposed. As always, starting with the constituents (Fig. 3.53). The hardest film is

WCN at H $\sim$ 32.4 GPa (E $\sim$ 403 GPa). Using H^3/E^2 as an estimate of fracture toughness, this coating is also tops at 0.21. This is similar to c-BC (see Table 1.2). Moving along in order of reduced hardness is the WC coating at H $\sim$ 23.1 GPa (E $\sim$ 320 GPa); $H^3/E^2 \sim 0.12$. Within the same table (Table 1.2) is a compound with very similar numbers: SiB_6. Looking back to Table 1.1, the H (E) is reported as 23.5 GPa (720 GPa). The significant reduction in Young's Modulus may be due to the inclusion of the Co-binder within the coating.

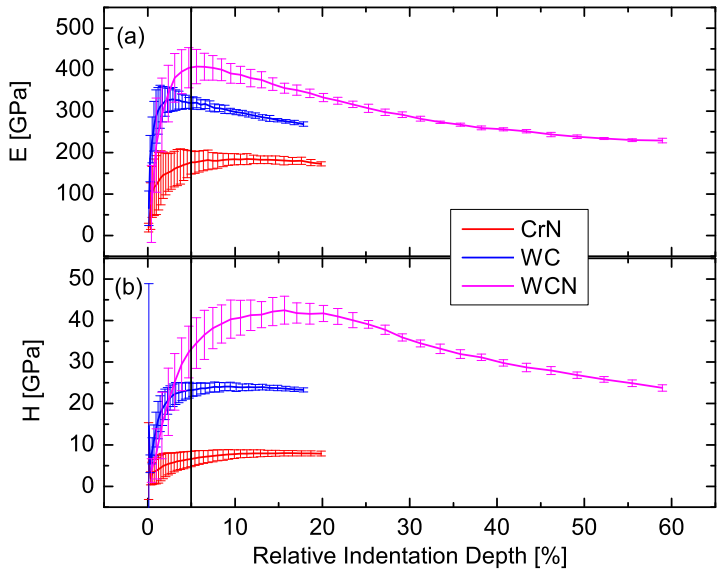

Figure 3.53: (a) Young's Modulus and (b) Hardness results for the constituent coatings deposited at high temperature. In order to avoid substrate effects, H and E were evaluated at 5 % of the total coating thickness.

Rounding out the constituent films is CrN. This coating has a H of 6.5 GPa, with a E of 175 GPa; $H^3/E^2 \sim 0.01$. These are significantly reduced from the reported values in Table 1.1. However, the lower than expected mechanical properties of the CrN coating may be explained by a combination of the stress state (tensile and low, see Fig. 3.49) and the observed high porosity (see Fig. 3.48(a)).

Nanoindentation was also carried out on the CrN-WC coatings; the results are presented in Fig. 3.54. Five out of the six coatings have very similar results. In fact, they are statistically equivalent, with H = 21.2 ± 1.3 GPa and E = 307 ± 8

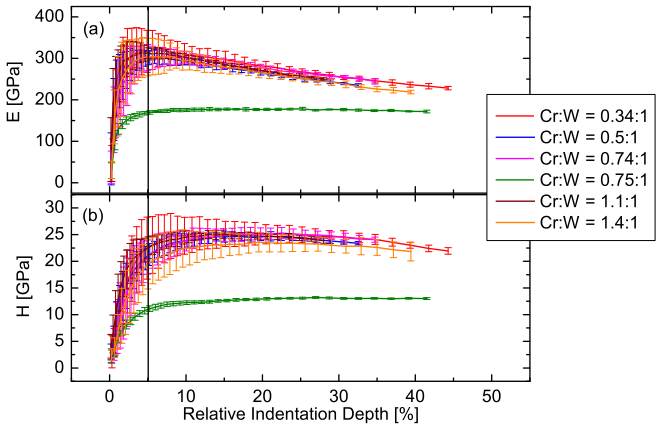

Figure 3.54: (a) Young's Modulus and (b) Hardness results for the CrN-WC coatings deposited at high temperature. In order to avoid substrate effects, H and E were evaluated at 5 % of the total coating thickness.

GPa; $H^3/E^2 \sim 0.10$ GPa. Looking back to Table 1.3, these values are very similar to nc-ZrC. The outlier is the Cr:W = 0.75:1 sample with a Hardness and Young's Modulus of 10.8 GPa and 167 GPa, respectively. This same sample was the outlier in the crystallographic structure (Fig. 3.47).

These results are a significant improvement over the H and E results from the low-temperature depositions (Fig. 3.31). Without heating, the average results were $\sim$ 6.4 GPa for H and $\sim$ 125 GPa for E[19]. An uncoated XC100 (AISI 1095) steel substrate has better mechanical properties, H $\sim$ 10 GPa and E $\sim$ 234 GPa. By adding heat to the process, the average values improved by $\sim$ 330 % for the Hardness and by $\sim$ 265 % for the Young's Modulus. The high-temperature deposition samples are hard, and relatively ductile. But they still well-below the state of the art in nanocomposite coatings (see Table 1.3).

Scratch Hardness (H_s) is another check on the mechanical properties of the system. If the measurement and calculation can avoid substrate effects, the H_s should be very similar to the substrate-independent H measured via

[19]Here, the outlier is the Cr:W = 1.5:1 sample. But, this sample is an improvement over the other four samples.

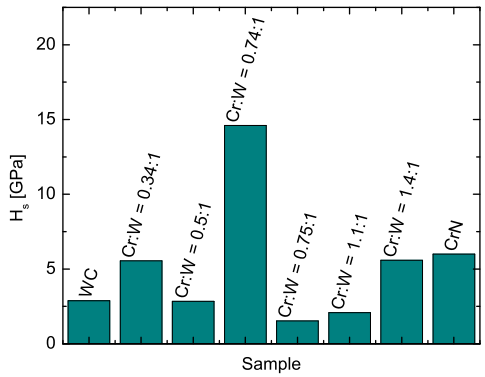

Figure 3.55: Scratch hardness for the high-temperature coatings. This calculation was based on the track profile obtained at L_{C1}.

nanoindentation. As stated in Sec. 2.3.9, the key parameter is the width of the scratch track. For consistency between the coatings, all widths were measured at the first critical load. While not shown here, optical micrographs confirm the existence of complete coatings at this point. From this measurement, the H_s is calculated using Eqn. 2.17. The results are presented in Fig. 3.55 and listed in Table 3.10.

Table 3.10: Scratch test results of the CrN-WC coatings, grown at high temperature on Si substrates.

Composition	L_{C1} [N]	L_{C2} [N]	L_{C3} [N]	H_s [GPa]
Constituent				
CrN	3.4	8.5		6.0
WC	2.6	9.5	16.8	2.9
WCN	2.4	25.8		
CrN-WC				
1.4:1	9.2	17.1	25.8	5.6
1.1:1	3.2	11.9	18.3	2.1
0.75:1	1.8	12.7	23.5	1.5
0.74:1	7.9	17.63		14.6
0.5:1	3.0	22.3		2.8
0.34:1	6.0	18.6		5.5

The determined values of H_s are significantly less than those obtained via nanoindentation. This is probably due to the influence of the substrate. Even at

L_{C1}, the depth profiles for the scratch track was deeper than the thickness of the coating. Since there was no coating delamination at this point during the scratch, both the coating and the substrate must have undergone significant plastic deformation. Also, as a side note, there does not seem to be any trend in the data.

Using a combination of experiment and simulation, Schwarzer, et al. [218] have shown the influence of the scratch tip size on the measurement of coating properties. According to their work, scratches using the traditional Rockwell C indenter (i.e. 300 μm radius) will not accurately measure the coating parameters. The stress fields developed under the tip will encompass both the coating and parts of the substrate. With these tips, it is nearly impossible to separate out the coating parameters. Only small radius tips ($\leq$ 50 nm), used at small loads ($\leq$ 20 N)[20], will be able to adequately measure the coating's scratch properties.

These same substrate effects will influence the measured critical loads (Table 3.10). Rather than obtaining the intrinsic failure loads of the coating, these results are significantly skewed by the steel substrate.

3.3.4 Summary for the high-temperature deposition of CrN-WC coatings

As stated at the beginning of this section, the high-temperature study was split into two complimentary components. In the first part of the study, CrN-WC thin films were deposited onto silicon, without a buffer layer. Two different compositions (Cr:W = 0.5:1, 3:1) were deposited at four different temperatures (400 °C, 270 °C, 180 °C, and with No External Heating (NEH)). The second study investigates the changes in mechanical properties as a function of chemical composition. Six different coatings, with target Cr:W ratios of 2:1, 1.5:1, 1.25:1, 1:1, 0.75:1, and 0.6:1, were deposited at 400 °C.

[20]The upper value for this load will depend on the sample under study. An *ab initio* study of the stress field will be required to accurately determine the upper load limit. Another thing to consider is tip damage. With a smaller tip radius, larger loads have the potential to significantly damage the tip.

CrN-WC thin films at variable temperature

- Chemical structure was determined by EDS and XPS:
  - The low-Cr coatings primarily consist of WC, W_2C, CrN, and Cr_2N. There is some evidence of CrO_x and free-carbon, but their signatures are weak.
  - The high-Cr films primarily consist of WC, CrN, Cr_2N, and CrO_x. There does not appear to be any free-carbon in these samples.
  - In both cases, the oxygen contamination was significantly less than most of the coatings deposited in the prior study at low deposition temperature, Sec. 3.2.
  - Also, there was a clear trend to lower Co content within the high-Cr content films at higher temperatures.
- Surface roughness measurements indicate relatively smooth films, with the best results from high-temperature deposition.
- From HR-SEM investigation, the growth modes were either within zone 2, or near the transition from zone 2 to 3
- No clear trend from the mechanical characterization
- In addition to normal characterization methods, these CrN-WC thin films were subjected to MPCVD-based nc-D deposition.
  - Most samples did not show any nc-D deposition.
  - Three high-Cr films did show nc-D deposition
    * High Cr-content reduces Co-concentration within the coatings. Cobalt is a known catalyst for carbon nanotube growth. This would significantly affect growth and adhesion of nc-D films.

    * Only one sample showed (high-Cr film, grown at 270 °C) a near complete nc-D film. However, it is unclear why this film succeeded where all others failed.
    * Other than the addition of Co, there appears to be very little reason for the success of nc-D deposition in Sec. 3.1, and rather weak nucleation in this study.

High-temperature CrN-WC coatings

- Constituent coatings: CrN, WC, and WCN coatings were deposited at high-temperature
  - EDS and XRD results confirm the deposition of Cr_2N, WC_{1-x}, and WCN coatings with average grain sizes of 62 nm, 6.2 nm, and 9.3 nm, respectively.
  - Examination of the microstructure yields a very porous CrN coating, with tapered columnar growth. Zone 1 growth is confirmed by the presence of tensile stress. The WC and WCN coatings are both dense, zone T structures, with compressive stress profiles.
  - Nanoindentation results yield hard WCN (32.4 GPa) and WC (23.1 GPa) coatings, but a very soft CrN (6.5 GPa) coating. This is probably related to the microstructures of the three coatings.
  - Scratch Hardness and critical loads are significantly affected by the substrate, and may have significantly lower values than the intrinsic coating values.
- CrN-WC coatings: six different compositions of CrN-WC coatings were deposited at high-temperature

- EDS results confirm the deposition of six different CrN-WC compositions, but their Cr:W ratios are *significantly* different from the target ratios.
- XRD results are relatively similar, and show a slight trend (when compared to the (200) peak, the (111) peak intensity increases with decreased Cr-content). However, there is outlier (Cr:W = 0.75:1).
- No surprises in examining the HR-SEM micrographs of the various CrN-WC coatings. The growth features fall either in zone 2, or near the boundary between zones 2 and 3.
- All CrN-WC coatings show compressive stress, but there is no correlation of the stress state with either the composition or the microstructure.
- Five out of the six CrN-WC coatings have statistically significant hardnesses and Young's moduli (H $\sim$ 21.2 GPa; E $\sim$ 307 GPa). The outlier has significantly lower values, and is the same coating as the outlier in the XRD data.
- Scratch Hardness and critical loads are significantly affected by the substrate, and may have significantly lower values than the intrinsic coating values.

CHAPTER IV

CONCLUSIONS AND PERSPECTIVES

This research project consisted of three phases to elucidate the composition-property relationship for coatings based on WC-Cr-N. The first phase was a viability study to determine initial parameters for the follow-on investigations. After this phase, another study began the investigation of composition-property relationships. This part was subdivided into two sections. First, the composition was varied by changing the amount of nitrogen in the working gas mixture. Then, the coating composition was further varied by changing the amount of power applied to the two sputtering targets (Cr and WC). All this was completed without external heating. The final phase added substrate heating.

4.1 Summary of the Viability Study

Using reactive RF magnetron sputtering, Cr-WC-N based coatings were successfully deposited onto both Si and Ti substrates. The binary WC coating was superhard (H $\sim$ 47 GPa), despite a grain size significantly smaller ($\sim$ 3 nm) than the typical critical grain size for Hall-Petch hardening. This may be due to the presence of both WC_{1-x} and W_2C phases. Additionally, the coatings were very smooth, with an $R_{RMS} \sim$ 1.1 nm. Unfortunately, these films partially delaminated from both the Si and Ti substrates. Ternary Cr-WC films also have high hardness (H $\sim$ 19 GPa), but with good adhesion. This coating probably consists of WC_{1-x} and Cr_7C_3 phases. While the mechanical results are promising, neither the WC nor the Cr-WC coating survived Microwave Plasma Chemical Vapor Deposition (MPCVD) process for nanocrystalline-Diamond (nc-D) deposition.

Introducing nitrogen into the working gas significantly reduced the deposition rate of WC, resulting in a WCN coating of only 0.9 μm. Chemical and structural characterization suggest a primarily WCN composition, with small amounts of metal oxide and free carbon. The combination of low thickness and multiple phases in a nearly amorphous structure may explain the measured mechanical properties (H $\sim$ 12 GPa; E $\sim$ 246 GPa). However, these coatings were still adherent after plasma treatment, and did support nc-D growth via MPCVD. However, the surface roughness of the nc-D coatings was significantly higher than desired. This may be the result of relatively low nucleation density and enhanced secondary nucleation during growth of the nc-D coating.

While not as hard as the WC coating, the CrN-WC coatings showed a much higher hardness than either the WCN or the Cr-WC coatings; H $\sim$ 30 GPa. This may be due to the formation of a nanocomposite of CrN and WC, as supported by XPS and XRD. However, it is unclear if the nanocomposite is formed by multiple nanocrystalline phases, or by a nanocrystalline/amorphous structure. The CrN-WC also survived plasma treatment, and nanocrystalline diamond films were successfully deposited. The nc-D coatings on CrN-WC were deposited under the same conditions as the nc-D films on WCN. As such, the nc-D coatings on CrN-WC also showed significantly increased the surface roughness.

Overall, the viability study was successful and showed the promise of combining CrN and WC phases in a single coating.

4.2 Summary for the low-temperature deposition of CrN-WC coatings

4.2.1 Varying the reactive gas mixture

Low temperature deposition of CrN-WC coatings was completed in two phases. In the first, the applied target power was kept constant, as the gas mixture was varied to study the impact of increasing N_2 concentration in the working gas.

Here, the target metal (Cr:W) ratio was 2:1 and the Ar/N_2 ratio was varied: 80/20, 60/40, and 40/60. Changing the nitrogen partial pressure does not seem to have an effect on the types of bonds. Also, according to the EDS results, nitrogen incorporation was maxed out at the intermediate gas mixture of $Ar/N_2 = 60/40$. This seems to correlate with the XRD results. At low-nitrogen content, the preferred orientation for the coating is (200). However, above saturation (i.e. maximum nitrogen incorporation), the preferred orientation is (111). This situation also correlates with the surface roughness of the samples: the low-nitrogen coating has significantly higher surface roughness than the other two samples (both at maximum nitrogen content).

An additional effect of changing the nitrogen concentration is observed in the deposition rate, and the growth mode. Unexpectedly, the low-nitrogen partial pressure has the slowest growth. The expected metallic sputtering mode should have demonstrated the highest deposition rates, but it did not. Looking at the HR-SEM micrographs, this low-nitrogen sample has ordered, but larger, grains. The larger grains indicate higher adatom mobility, which may explain the lower deposition rate (i.e. low adatom lifetimes). This may also explain the higher level of compressive stress in this coating compared to the other coatings; with a high adatom mobility/short adatom lifetime, there may be insufficient time for relaxation processes to occur.

At higher nitrogen incorporation (i.e. saturation), the growth rates were both reasonable at 12.3 nm/min and 13.2 nm/min for the intermediate- and high-nitrogen partial pressures, respectively. Increasing the nitrogen partial pressure may decrease the adatom mobility, i.e. longer adatom lifetimes, as compared to the low-nitrogen sample.

Despite nitrogen saturation in both the intermediate- and high-nitrogen samples, there is a difference in the growth mode of these two coatings. The

intermediate-nitrogen partial pressure sample seems to be subject to a higher amount of ion impacts, resulting in pushing the growth mode towards the boundary between zone 2 and zone 3 in the extended MDT model. Unfortunately, this sample does appear to suffer from significant voids, i.e. high porosity. The high-nitrogen sample appears to fall at the other end of the zone, at the boundary between zone T and zone 2. And this sample appears to be fairly dense, with low porosity (~ 0.3 %).

Overall, this study on the effects of changing the nitrogen partial pressure was very interesting. There were clear trends of decreasing surface roughness with increased nitrogen partial pressure; and, unexpectedly, increased deposition rates with increased nitrogen partial pressure. Despite the increased porosity, the intermediate gas mixture was chosen to continue the experiments in the next phase: varying the applied sputtering power. This was done to maximize the chances of a reasonable deposition rate, with low surface roughness and decent mechanical properties.

4.2.2 Varying the applied sputtering power

In the second study, the gas mixture was fixed at $Ar/N_2 = 60/40$ while the applied target power was varied. This resulted in changes to the Cr:W ratio. Five different compositions were created to study further the composition-property relationships.

At low Cr content, the coatings appear to exhibit a single broad peak, across several different phases. Once past a threshold value in the Cr-concentration, the diffractograms indicate a distorted fcc B1 (NaCl)-type structure. This structural transformation may be indicative of nanocomposite formation. XPS supports this possibility, with clear Cr-N and W-C bonding. However, XRD and XPS cannot determine the exact nature of this nanocomposite. It may consist of multiple nanocrystalline phases, or a combination of a nanocrystalline phase and an

amorphous phase.

With the exception of the Cr:W = 1.5:1 and the Cr:W = 1:1 samples, the mechanical properties are statistically equivalent. There may be a very weak trend of reduced mechanical properties with increased Cr, but this variation falls within the error in the experiment. As for the "outliers," the Cr:W = 1:1 sample has the lowest H (E) and the Cr:W = 1.5:1 sample has the highest. The low values from the Cr:W =1:1 sample may be due the amorphous nature of the sample. As for the Cr:W =1.5:1 nanocomposite, the main differentiation from the other nanocomposite compositions is oxygen contamination. The Cr:W = 4:1, 3:1, and 2:1 samples have an average of $\sim$ 6.5 at. % oxygen. The Cr:W = 1.5:1 sample has only $\sim$ 3.5 at. % oxygen. The advantages of low oxygen contamination are also demonstrated in the open circuit porosity tests. While the porosity of the Cr:W = 1.5:1 coating is not significantly different than the other CrN-WC coatings, optical micrographs of the post-test surface show significantly higher adhesion compared to the Cr:W = 4:1, 3:1, and 2:1 samples.

As such, it may be able to improve the results. Substrate heating may improve the mechanical properties of the coatings. By elevating the growth temperature, the resultant films would have improved film adhesion, lower porosity, less oxygen contamination, and improved stress development. In addition, prior literature on nanocomposites (as introduced in Sec. 1.3.3.2) indicate the best results are with completely separate phases. This spinodal decomposition is a thermodynamically-driven process, and would be enhanced by elevated growth temperatures.

4.3 Summary for the high-temperature deposition of CrN-WC coatings

4.3.1 High-temperature CrN-WC thin films

The high-temperature phase of the project was split into two complimentary components. First, CrN-WC thin films were deposited onto silicon, without a buffer layer. These films and the subsequent coatings (Sec. 3.3.3) were deposited with a pure Cr target and a cemented carbide (WC-6 % Co) target. Two different compositions (Cr:W = 0.5:1, 3:1) were deposited at four different temperatures (400 °C, 300 °C, 200 °C, and without external heating (NEH)). Deposition times were kept short, with the goal of films $\leq$ 500 nm thick.

The chemical structure of these eight samples was characterized by EDS and XPS. The chemical structure of the low-Cr thin films consist of WC, W_2C, CrN, and Cr_2N phases. Additionally, there is some evidence of CrO_x and free-carbon, but their signatures are weak. The high-Cr thin films have a similar structure, but the W_2C phase is replaced with a CrO_x phase; there is no evidence of free-carbon. EDS also reveals significantly reduced oxygen contamination compared to the samples deposited without external heating, Sec. 3.2.

Using HR-SEM, both the film thicknesses and the growth modes are easily determined. All coatings are less than 500 nm thick, but the thinnest films occur at high temperature deposition. Typically, this is related to high adatom mobility, and shorter surface residence times.

Low-Cr samples are denser, and have less well-defined columnar growth than their high-Cr counterparts. Combining this with the surface morphology, the low-Cr content samples fall within zone 2 of the extended MDT model. High-Cr samples also fall within zone 2, but their more well-developed columnar structure places them closer to the boundary region between zones 2 and 3. Surface roughness measurements cannot be correlated with the microstructure. Luckily, all films are

relatively smooth, but the best results are with high-temperature deposition. Similarly, there does not seem to be a clear correlation of stress development with microstructure, composition, or even deposition temperature.

While the mechanical properties of the thin films do change with temperature, there is no clear trend. The only real observation is an increase in sample stiffness, and some hardness enhancement at higher temperatures. This may be related to the higher thermal stress states produced at higher deposition temperatures. This holds true for both the low- and high-Cr samples. However, the actual values are significantly less than the CrN-WC coating deposited in the viability study, Sec. 3.1.

In addition to normal characterization methods, these CrN-WC thin films were subjected to MPCVD-based nc-D deposition. While all sample survived the plasma treatment and deposition process, most did not show evidence of nc-D deposition. Only three of the eight samples show significant nc-D deposition. These three samples were the high-Cr films deposited at 390 °C, 270 °C, and No External Heating (NEH). However, only one of these samples (deposited at 270 °C) seemed to have a complete coating. The other two samples show evidence of nc-D growth, but not complete coverage. While there is no ready explanation of the temperature effects on the nc-D nucleation, there may be an explanation on why only the high-Cr samples nucleated nc-D. As stated earlier, EDS results indicated a trend of reduced Co incorporation for the high-Cr samples deposited at high temperature. Since cobalt is a known catalyst for carbon nanotube growth and promotes other non-diamond carbon growth, its presence may explain the lack of nc-D nucleation.

4.3.2 High-temperature CrN-WC coatings

The second study investigates the changes in mechanical properties as a function of chemical composition. Six different coatings, with target Cr:W ratios of

2:1, 1.5:1, 1.25:1, 1:1, 0.75:1, and 0.6:1, were deposited at 400 °C. Additional coatings of CrN, WC, and WCN were also deposited at high temperature to study the effects of high-temperature growth on the constituents of CrN-WC coatings.

After deposition, one of the first techniques for characterization is EDS for the discovery of the chemical structure of the coating systems. For the constituent WC and WCN coatings, there are no significant surprises in the EDS results. However, the XRD patterns hold a significant change for the WCN coating. During the viability study, a WCN coating was deposited. The XRD pattern for this coating was a single, broad peak (FWHM $\sim 6.1°$). While the XRD pattern implied there may be multiple phases, XPS results indicated only one bonding state: WC_xN_y. Therefore, this coating was nearly amorphous.

Fast forward to the present study, with WCN coating deposition at high-temperature. The resulting XRD pattern consists of multiple peaks, with a much narrower FWHM. For all appearances, this seems to be a single WCN phase, with more defined crystals. An additional surprise came from the CrN coating. The EDS results indicate a Cr_2N film rather than CrN (as was expected from the deposition conditions). This has been confirmed by XRD.

In the case of CrN-WC coatings deposited at high-temperature, EDS reveals significant differences between the target Cr:W ratio and the actual Cr:W ratio. If these coatings were deposited at low-temperature, many of them would probably form solid-solutions (similar to the Cr:W = 1:1 coating in Sec. 3.2). However, the use of substrate heating has improved the phase segregation, and as XRD shows, these coatings do not show the typical solid-solution diffractogram.

Looking at the HR-SEM micrographs, CrN has a surprisingly porous structure with tapered columns. While the generalized temperature would place the growth mode clearly in zone 2, the actual result is a coating with zone 1 features. This is supported by the tensile stress state of the CrN coating. Both the WC and

WCN coatings show zone T features, with the WCN coating approaching the boundary region between zones T and 2. The CrN-WC coatings offer no significant surprises, and all have relatively dense microstructures with clear zone T, zone 2, and even some zone 3 features. Additionally, the stress states for all CrN-WC coatings is compressive. Still, there does not seem to be any correlation between either the stress state and the composition or the stress state and the microstructure.

All that remains to discuss are the mechanical properties. These properties were elucidated by two different techniques: nanoindentation and scratch testing. Nanoindentation provides both H and E while scratch testing yields critical loads (for deformation and damage) and the H_s.

From the nanoindentation of the constituent coatings, the WCN coating is the hardest and the CrN coating is the softest. This is expected from their relative microstructures. WCN is a dense, single-phase coating. CrN is very porous, with a tapered columnar structure. Moving onto the CrN-WC coatings, the big surprise is the lack of diversification in the results. Five out of the six coatings are statistically equivalent ($H \sim 21.2$ GPa; $E \sim 307$ GPa). While this is a significant improvement over the mechanical properties of the low-temperature coatings deposited in Sec. 3.2, it is still well-below the state of the art in industrial hard coatings (as demonstrated by the nc-TiN/a-SiN nanocomposite).

Additionally, the Scratch Hardness (H_s) results are far from enlightening. On average, the values are significantly less than the nanoindentation results. H_s should be relatively close to nanoindentation H. However, substrate effects can be significant, as they are here. On average, the depth of the scratch profile at the first critical load is deeper than the coating thickness. Since there is no evidence of delamination at this load, the scar must be accommodated by significant plastic deformation in both the coating and the substrate. This adversely affects the H_s

results. The only proper way to reveal the scratch hardness is through the use of a significantly smaller indenter tip at lower loads. This keeps the stress field contained to the sample, and eliminates substrate effects on the Scratch Hardness.

The same problem occurs with the critical loads. Rather than investigating the plastic deformation points of the coating, these results are for the coating-substrate system; and they are substrate-heavy. As such, the values for both the first critical load (onset of conformal cracking), the second critical load (onset of coating delamination via spalling), and the final critical load (onset of complete coating failure) may be significantly reduced from their intrinsic coating values.

4.4 Perspectives

4.4.1 Further tests on the current material: CrN-WC

Initial results from the viability study were very promising. However, the follow-on study of varying the actual composition suffered from oxygen contamination problems, low adhesion, low stress states, and high porosity. As such, it was never able to reproduce the intial success of a very hard CrN-WC coating. The addition of substrate heating during deposition significantly improved the mechanical properties of the coatings. While not the high hardness of the viability study, CrN-WC coatings produced with substrate heating were reasonable hard and ductile.

Developing CrN-WC hard coatings has been full of challenges, but the end result has been the establishment of a possible pathway to a hard and ductile coating system that may be useful in several different areas. However, complete elaboration of such a coating system, for specific applications, is beyond the scope of this work. There is still a plethora of work to be completed before CrN-WC system can be realized as a functional coating system.

For example, a rather immediate need exists for cross-sectional

High-Resolution Transmission Electron Microscope (HR-TEM) measurements of the CrN-WC samples deposited at various substrate temperatures. This study would provide direct confirmation of the nanocomposite structure, and the optimal growth temperature for phase segregation. If Electron Back-Scatter Diffraction (EBSD) is simultaneously measured, the type of nanocomposite can also be directly determined, i.e formed by multiple nanocrystalline phases, or a single nanocrystalline phase in an amorphous matrix. Additionally, HR-TEM micrographs would yield precise measurements of the crystallite grain sizes and the grain boundary thicknesses. Depending on these results, the lack of variability in the mechanical properties of the CrN-WC coatings, deposited at low and high substrate temperatures in the present work, may be explained.

Another area of exploration with the current set of samples is tribology. One of the possible uses for these coatings is as a protective layer for wood-cutting tools. High adhesion, low coefficients of friction, and high wear resistance are vital to the success of any protective coating on a cutting tool. Reciprocating and pin-on-disc studies of coatings against standard and unique counterparts (such as wood) can provide valuable insight into these properties, and the viability of these coatings as protective layers for cutting tools. Additionally, corrosion tests (in alkaline, neutral, and acidic solutions) would investigate the surface reactions between the coating and the "juices" produced during wood-cutting operations. If successful, additional tests (such as tribo-corrosion and cutting tests under operating conditions) would yield additional understanding.

Similar tests should also be completed after MPCVD treatment when uniform and complete nc-D coatings are observed.

4.4.2 Improving the current material: CrN-WC

However, it is possible that the current set of samples are not up to snuff, and cannot effectively function as protective coatings. However, before the final conclusions on the feasibility of CrN-WC nanocomposites as a protective coating, additional variations in the deposition process should be explored. For example, the HR-TEM micrographs may show nanocomposite samples with a wide range of crystallite size distributions, or thick grain boundaries. Either of these could adversely affect the mechanical properties of the coating system. Controlling the grain size (and its distribution) may supply improved mechanical properties. A well-known method for controlling grain size is through controlling the ion bombardment during the deposition. This could be accomplished via Unbalanced Magnetron Sputtering, Plasma-Enhanced Magnetron Sputtering, HIgh Power Impulse Magnetron Sputtering, or with a hybrid Ion Beam-Magnetron Sputtering system. Additional control can be achieved with sample biasing.

Another variation in the deposition conditions may be related to the sputtering targets themselves. In this study, the coatings were deposited by co-sputtering a pure Cr target and a compound WC target in an Ar/N_2 atmosphere. It may be possible to use elemental Cr and W targets in an $Ar/N_2/CH_4$ (or $Ar/N_2/C_2H_2$) atmosphere. This could provide additional control over the grain boundary thickness. However, it should be noted that there is a very narrow window for the use of a carbon source in reactive sputtering. Excess carbon precursor can easily lead to the development of graphitic carbon within the coating [219]. Another major concern is coating embrittlement via H incorporation.

Finally, the above techniques could be combined with changing the reactive gas mixture and the deposition temperature. Improvements in the gas delivery system and the substrate heater could open the door to additional investigations. As shown in Table 4.1, only a small portion of the possible deposition conditions

have been explored to date.

Table 4.1: Possible deposition conditions for investigating the CrN-WC coating system. Only those coatings marked (X) have been created and characterized.

	Temperature [°C]									
	100	200	300	400	500	600	700	800	900	1000
Ar/N_2										
90/10										
80/20	X									
70/30										
60/40	X	X	X	X						
50/50										
40/60	X									
30/70										

4.4.3 Towards other materials of interest

As stated in Sec. 1.4, the vast majority of research into nanocomposite protective coatings has focused on nitride/nitride, nitride/metal, nitride/a-C, carbide/metal, and carbide/a-C combinations. And while this study has started to fill the gap on carbide/nitride nanostructured systems, it is only a small piece of the overall puzzle. Other systems should be explored.

Initially, candidates can be identified via binary phase diagrams of the constituent metals. For example, at temperatures below 1400 °C, chromium and tungsten have a large miscibility gap[1]. Similarly, aluminum and silicon have a large miscibility gap at formation temperatures below 570 °C. Another system may be chromium and molybdenum, with a wide ranging miscibility gap below 450 °C; silicon and zinc also have a wide miscibility gap, under 450 °C. Other possible systems (with smaller compositional ranges) of interest are titanium-tungsten, silicon-tantalum, silicon-vanadium, aluminum-vanadium, aluminum-tungsten, and aluminum-zirconium.

[1]Binary phase diagrams from the CRC Handbook [205] and calculated by the Scientific Group Thermodata Europe [220] were examined for possible candidates.

Looking at metallic binary phase diagrams is only an initial step in identifying possible nanocomposite-forming compounds. Another important step is involved in the process: further computation. When compounds are formed, the Gibbs free energy is inherently different than the constituent elements. As such, the compound would behave differently than the metallic phase.

Therefore, it becomes necessary to calculate the phase diagrams of ternary and quaternary blends based on the constituent binary compounds, such as Cr-N and W-C. A miscibility gap in this phase diagram is essential for proper nanocomposite formation. Luckily, thermodynamic simulation software has come quite a long way, and there are packages available, such as MTDATA [221], to assist with these calculations.

Using the obtained computational results, it is necessary to identify possible applications for the use of these coatings. This information would further cull the field of possible candidates. For example, within hard protective coatings, SiN-TaC may be a promising candidate. Silicon nitride is a covalent ceramic, with relatively good mechanical properties. Tantalum carbide is a brittle metalloid, but it is a refractory compound with one of the highest known melting points. Additionally, the formation of passivation films (TaO_x and SiO_x) make these promising candidates for high temperature, corrosive environments. However, it should be noted that the miscibility gap is not complete. Below 0.33 mole of Ta, Si and $TaSi_2$ phases are present. A second 'gap' exists above 0.75 mole of Ta, with Ta and Ta_3Si present. It is possible that using a Si and TaC target in an Ar/N_2 environment may expand this miscibility gap. Another attractive material set is based on yttrium and zirconium. This set of materials has a wide miscibility gap, across both composition and temperature. With respect to the possible constituents, both ZrN and ZrC are used in the cutting tool industry due to their good mechanical properties, corrosion resistance, and low wear rates. Additionally, ZrC can bear high

temperature loading. Elemental yttrium has been used to control the grain size in different metallic compounds, such as ZrN. And YN is very similar to TiN, with respect to its mechanical properties. Finally, as before with SiN-TaC, both Zr and Y form very stable metal oxides which act as passivation layers. This study has demonstrated the feasibility of nitride/carbide nanocomposite structures. And while superhardness was not attained, the resultant CrN-WC coatings were hard and ductile. Additional studies and variations in the deposition conditions may yet produce superhard coatings. However, this system is just a start in the process of filling in the knowledge gap left by nitride/carbide nanocomposite coatings. Combining the power of computational methods with well-planned experiments on other possible coating systems, such as SiN-TaC or YN-ZrC, would further our understanding.

LIST OF REFERENCES

[1] S.P. McPherron, Z. Alemseged, C.W. Marean, J.G. Wynn, D. Reed, D. Geraads, R. Bobe, H.A. Béarat, Nature **466**(7308), 857 (2010). DOI 10.1038/nature09248

[2] S. Semaw, M.J. Rogers, J. Quade, P.R. Renne, R.F. Butler, M. Dominguez-Rodrigo, D. Stout, W.S. Hart, T. Pickering, S.W. Simpson, Journal of Human Evolution **45**(2), 169 (2003). DOI 10.1016/S0047-2484(03)00093-9

[3] L. Wadley, Current Anthropology **51**(S1), S111 (2010). DOI 10.1086/649836

[4] M. Lombard, Journal of Archaeological Science **35**(1), 26 (2008). DOI 10.1016/j.jas.2007.02.021

[5] K.S. Brown, C.W. Marean, A.I.R. Herries, Z. Jacobs, C. Tribolo, D. Braun, D.L. Roberts, M.C. Meyer, J. Bernatchez, Science **325**(5942), 859 (2009). DOI 10.1126/science.1175028

[6] D.E. Miller, N.J.V.D. Merwe, The Journal of African History **35**(1), 1 (1994)

[7] M. Radivojević, T. Rehren, E. Pernicka, D. Šljivar, M. Brauns, D. Borić, Journal of Archaeological Science **37**(11), 2775 (2010). DOI 10.1016/j.jas.2010.06.012

[8] R. Tewari, Antiquity **77**(297), 536 (2003)

[9] S.B. Alpern, History in Africa **32**(1), 41 (2005). DOI 10.1353/hia.2005.0003

[10] T. Stech-Wheeler, J.D. Muhly, K.R. Maxwell-Hyslop, R. Maddin, American Journal of Archaeology **85**(3), 245 (1981)

[11] H. Bessemer. United States Patent 51,398 (1855)

[12] R.F. Bunshah, Journal of Vacuum Science and Technology **11**(4), 814 (1974)

[13] R.F. Bunshah, A.H. Shabaik, R. Nimmagadda, J. Covy, Thin Solid Films **45**(3), 453 (1977)

[14] R.R. Nimmagadda, H.J. Doerr, R.F. Bunshah, Thin Solid Films **84**(3), 303 (1981)

[15] K.H. Kloss, E. Broszeit, H.M. Gabriel, Thin Solid Films **80**(1-3), 307 (1981)

[16] H. Holleck, Journal of Vacuum Science & Technology A: Vacuum, Surfaces, and Films **4**(6), 2661 (1986). DOI doi:10.1116/1.573700

[17] D.S..S. Stone, Journal of Vacuum Science & Technology A: Vacuum, Surfaces, and Films **9**(4), 2543 (1991). DOI 10.1116/1.577270

[18] H.C. Barshilia, K.S. Rajam, Journal of Materials Research **19**(11), 3196 (2004). DOI 10.1557/JMR.2004.0444

[19] J. Jagielski, A.S. Khanna, J. Kucinski, D.S. Mishra, P. Racolta, P. Sioshansi, E. Tobin, J. Thereska, V. Uglov, T. Vilaithong, Applied surface science **156**(1-4), 47 (2000)

[20] S. Han, J.H. Lin, S.H. Tsai, S.C. Chung, D.Y. Wang, F.H. Lu, H.C. Shih, Surface and Coatings Technology **133**, 460 (2000)

[21] C.S. Lin, C.S. Ke, H. Peng, Surface and Coatings Technology **146**, 168 (2001)

[22] I.E. Paulauskas, M.P. Brady, H.M. Meyer III, R.A. Buchanan, L.R. Walker, Corrosion Science **48**(10), 3157 (2006). DOI 10.1016/j.corsci.2005.10.019

[23] J. Lin, W.D. Sproul, J.J. Moore, S. Lee, S. Myers, Surface and Coatings Technology **205**(10), 3226 (2011). DOI 10.1016/j.surfcoat.2010.11.039

[24] T. Hurkmans, D.B. Lewis, J.S. Brooks, W.D. Münz, Surface and Coatings Technology **86**, 192 (1996)

[25] G. Bertrand, C. Savall, C. Meunier, Surface and Coatings Technology **96**(2-3), 323 (1997)

[26] S. Han, J.H. Lin, J.J. Kuo, J.L. He, H.C. Shih, Surface and Coatings Technology **161**(1), 20 (2002)

[27] P. Hones, N. Martin, M. Regula, F. Levy, Journal of Physics D: Applied Physics **36**(8), 1023 (2003)

[28] Y. Zou, The microstructure, mechanical properties, and thermal stability of ternary $Cr_{1-x}Mo_xN_y$ thin-films. Ph.D. thesis, University of Alabama at Birmingham, Birmingham, AL (2012)

[29] W. Brandl, C. Gendig, Thin Solid Films **290**, 343 (1996)

[30] J. Creus, H. Idrissi, H. Mazille, F. Sanchette, P. Jacquot, Surface and Coatings Technology **107**(2-3), 183 (1998)

[31] A. Warren, A. Nylund, I. Olefjord, International Journal of Refractory Metals and Hard Materials **14**(5-6), 345 (1996). DOI 10.1016/S0263-4368(96)00027-3

[32] Y. Li, Y. Gao, B. Xiao, T. Min, Z. Fan, S. Ma, L. Xu, Journal of Alloys and Compounds **502**(1), 28 (2010). DOI 10.1016/j.jallcom.2010.04.184

[33] W. Acchar, U.U. Gomes, W.A. Kaysser, J. Goring, Materials Characterization **43**(1), 27 (1999). DOI 10.1016/S1044-5803(98)00056-4

[34] R.I. Blombery, C.M. Perrot, P.M. Robinson, Materials Science and Engineering **13**(2), 93 (1974). DOI 10.1016/0025-5416(74)90176-1

[35] J.A. Bailey, A.M..M. Bayoumi, J.S. Stewart, Wear **85**(1), 69 (1983). DOI 10.1016/0043-1648(83)90336-8

[36] A.J. Gant, M.G. Gee, Wear **251**(1-12), 908 (2001). DOI 10.1016/S0043-1648(01)00749-9

[37] J.S. Becker, R.G. Gordon, Applied Physics Letters **82**(14), 2239 (2003)

[38] C. Shi, X.F. Yang, A.M. Zhu, C.T. Au, Catalysis Today **93**, 819 (2004). DOI 10.1016/j.cattod.2004.06.102

[39] T. Polcar, N.M.G. Parreira, A. Cavaleiro, Wear **265**(3-4), 319 (2008). DOI 10.1016/j.wear.2007.10.011

[40] J. Yan, X. Ma, W. Zhao, H. Tang, C. Zhu, S. Cai, Materials Science and Engineering B **117**(3), 321 (2005). DOI 10.1016/j.mseb.2004.12.063

[41] G.D. Suetin, I.R. Shein, A.L. Ivanovskii, Russian Journal of Inorganic Chemistry **54**(9), 1433 (2009). DOI 10.1134/S0036023609090150

[42] E. Principe, B. Shaw, Corrosion **53**(9), 675 (1997)

[43] K.S. Weil, P.N. Kumta, Journal of Solid State Chemistry **128**(2), 185 (1997)

[44] P. Hones, M. Diserens, R. Sanjines, F. Levy, Journal of Vacuum Science & Technology B: Microelectronics and Nanometer Structures **18**, 2851 (2000)

[45] P. Hones, R. Consiglio, N. Randall, F. Lvy, Surface and Coatings Technology **125**(1-3), 179 (2000). DOI 10.1016/S0257-8972(99)00541-1

[46] T. Polcar, A. Cavaleiro, Materials Chemistry and Physics **129**(1-2), 195 (2011). DOI 10.1016/j.matchemphys.2011.03.078

[47] J. Lin, J.J. Moore, W.C. Moerbe, M. Pinkas, B. Mishra, G.L. Doll, W.D. Sproul, International Journal of Refractory Metals and Hard Materials **28**(1), 2 (2010). DOI 10.1016/j.ijrmhm.2009.07.012

[48] K. Ho Kim, E. Young Choi, S. Gyun Hong, B. Gyu Park, J. Hong Yoon, J. Hae Yong, Surface and Coatings Technology **201**(7), 4068 (2006). DOI 10.1016/j.surfcoat.2006.08.098

[49] F. Monteverde, A. Bellosi, Corrosion Science **44**(9), 1967 (2002)

[50] A. Bellosi, R. Calzavarini, M.G. Faga, F. Monteverde, C. Zancol, G.E. D'Errico, Journal of Materials Processing Technology **143**, 527 (2003)

[51] A.P. Umanskii, V.A. Lavrenko, S.S. Chuprov, V.P. Konoval, Refractories and Industrial Ceramics **47**(4), 246 (2006)

[52] F. Vaz, L. Rebouta, M. Andritschky, M.F. da Silva, J.C. Soares, Journal of Materials Processing Technology **92**, 169 (1999)

[53] J. Musil, H. Hrubý, Thin Solid Films **365**(1), 104 (2000). DOI 10.1016/S0040-6090(00)00653-2

[54] A.E. Santana, A. Karimi, V.H. Derflinger, A. Schutze, Tribology Letters **17**(4), 689 (2004)

[55] D. Rafaja, C. Wüstefeld, C. Baehtz, V. Klemm, M. Dopita, M. Motylenko, C. Michotte, M. Kathrein, Metallurgical and Materials Transactions A pp. 1–11 (2010). DOI 10.1007/s11661-010-0204-8

[56] J. Vetter, E. Lugscheider, S.S. Guerreiro, Surface and Coatings Technology **98**(1), 1233 (1998)

[57] I.W. Park, D.S. Kang, J.J. Moore, S.C. Kwon, J.J. Rha, K.H. Kim, Surface and Coatings Technology **201**(9-11), 5223 (2007). DOI 10.1016/j.surfcoat.2006.07.118

[58] Y. Benlatreche, C. Nouveau, H. Aknouche, L. Imhoff, N. Martin, J. Gavoille, C. Rousselot, J.Y..Y. Rauch, D. Pilloud, Plasma Processes and Polymers **6**(S1), S113 (2009). DOI 10.1002/ppap.200930407

[59] H.C. Barshilia, M.S. Prakash, A. Jain, K.S. Rajam, Vacuum **77**(2), 169 (2005). DOI 10.1016/j.vacuum.2004.08.020

[60] U. Helmersson, S. Todorova, S.A. Barnett, J.E. Sundgren, L.C. Markert, J.E. Greene, Journal of Applied Physics **62**(2), 481 (1987)

[61] J.K. Park, Y.J. Baik, Surface and Coatings Technology **200**(5-6), 1519 (2005). DOI 10.1016/j.surfcoat.2005.08.099

[62] J. Musil, Surface and Coatings Technology **125**(1-3), 322 (2000). DOI 10.1016/S0257-8972(99)00586-1

[63] S.M. Gorbatkin, R.L. Rhoades, T.Y. Tsui, W.C. Oliver, Applied Physics Letters **65**(21), 2672 (1994)

[64] W.C. Oliver, G.M. Pharr, Journal of Materials Research **7**(6), 1564 (1992)

[65] A.A. Voevodin, J.S. Zabinski, Diamond and Related Materials **7**(2-5), 463 (1998)

[66] T.Y. Tsui, G.M. Pharr, W.C. Oliver, C.S. Bhatia, R.L. White, S. Anders, A. Anders, I.G. Brown, MRS Symposium Proceedings **383**, 447 (1995)

[67] C.S. Chen, C.P. Liu, C.Y.A. Tsao, Thin Solid Films **479**(1-2), 130 (2005). DOI 10.1016/j.tsf.2004.11.196

[68] F.B. Wu, S.K. Tien, J.G. Duh, J.W. Lee, Journal of Electronic Materials **34**(12), 1533 (2005)

[69] J. Romero, E. Martínez, J. Esteve, A. Lousa, Surface and Coatings Technology **180-181**, 335 (2004). DOI 10.1016/j.surfcoat.2003.10.082

[70] S. Veprek, Thin Solid Films **317**(1-2), 449 (1998)

[71] S. Veprek, P. Nesladek, A. Niederhofer, F. Glatz, M. Jilek, Surface and Coatings Technology **108**(1-3), 138 (1998)

[72] S. Veprek, Thin Solid Films **297**(1-2), 145 (1997)

[73] M. Benda, J. Musil, Vacuum **55**(2), 171 (1999)

[74] S. Zhang, Y. He, M. Li, Y. He, S. Kwon, J. Yoon, T. Cho, Thin Solid Films **518**(18), 5227 (2010). DOI 10.1016/j.tsf.2010.05.053. URL http://www.sciencedirect.com/science/article/pii/S0040609010007212

[75] J.S. Koehler, Physical review B **2**(2), 547 (1970)

[76] S.L..L. Lehoczky, Journal of Applied Physics **49**(11), 5479 (1978). DOI 10.1063/1.324518

[77] X. Chu, S.A. Barnett, Journal of Applied Physics **77**(9), 4403 (1995)

[78] M. Shinn, S.A..A. Barnett, Applied Physics Letters **64**(1), 61 (1994). DOI 10.1063/1.110922

[79] Q. Yang, C. He, L.R. Zhao, J.P. Immarigeon, Scripta materialia **46**(4), 293 (2002)

[80] X. Junhua, L. Geyang, G. Mingyuan, Thin Solid Films **370**(1), 45 (2000)

[81] J.W. Gahn, Acta Metallurgica **11**(12), 1275 (1963). DOI 10.1016/0001-6160(63)90022-1

[82] P.C. Yashar, W.D. Sproul, Vacuum **55**(3-4), 179 (1999)

[83] F.H. Mei, N. Shao, J.W. Dai, G.Y. Li, Materials Letters **58**(27-28), 3477 (2004). DOI 10.1016/j.matlet.2004.07.005

[84] Q. Yang, L.R. Zhao, R. McKellar, P.C. Patnaik, Vacuum **81**(1), 101 (2006). DOI 10.1016/j.vacuum.2006.03.002

[85] R. Haubner, S. Kubelka, B. Lux, M. Griesser, M. Grasserbauer, Journal de Physique IV **5**(C5), 753 (1995)

[86] N.M. Everitt, R.F. Silva, J. Vieira, C.A. Rego, C.R. Henderson, P.W. May, Diamond and Related Materials **4**(5-6), 730 (1995). DOI 10.1016/0925-9635(94)05298-0

[87] N. Toprani, S.A. Catledge, Y.K. Vohra, R. Thompson, Journal of Materials Research **15**(5), 1052 (2000)

[88] F.H. Sun, Z.M. Zhang, M. Chen, H.S. Shen, Diamond and Related Materials **12**(3-7), 711 (2003). DOI 10.1016/S0925-9635(02)00345-X

[89] F. Álvarez, M. Reinoso, H. Huck, M. Rosenbusch, Applied Surface Science **256**(12), 3962 (2010). DOI 10.1016/j.apsusc.2010.01.056

[90] A. Kumar, Q. You, J.S. Kapat, A. Mangiaracina, A. Catletge, Y. Vohra, Thin Solid Films **308-309**, 209 (1997). DOI 10.1016/S0040-6090(97)00669-X

[91] Y. Lifshitz, C.H. Lee, Y. Wu, W.J. Zhang, I. Bello, S.T. Lee, Applied Physics Letters **88**(24), 243114 (2006). DOI doi:10.1063/1.2213019

[92] S. Christiansen, M. Albrecht, H.P. Strunk, S. Veprek, Journal of Vacuum Science & Technology B: Microelectronics and Nanometer Structures **16**(1), 19 (1998)

[93] E.O. Hall, Proceedings of the Physical Society. Section B **64**, 747 (1951)

[94] N.J. Petch, Journal of the Iron and Steel Institute **174**, 25 (1953)

[95] D. Tabor, Proceedings of the Royal Society of London. Series A, Mathematical and Physical Sciences **192**(1029), 247 (1948)

[96] J.R. Weertman, Materials Science and Engineering: A **166**(1-2), 161 (1993)

[97] Z.B. Qi, P. Sun, F.P. Zhu, Z.C. Wang, D.L. Peng, C.H. Wu, Surface and Coatings Technology (2011). DOI 10.1016/j.surfcoat.2011.01.021

[98] A.H. Chokshi, A. Rosen, J. Karch, H. Gleiter, Scripta Metallurgica **23**(10), 1679 (1989)

[99] R.A. Masumura, P.M. Hazzledine, C.S. Pande, Acta Materialia **46**(13), 4527 (1998)

[100] B. Jiang, G.J. Weng, Metallurgical and Materials Transactions A **34**(3), 765 (2003)

[101] X. Qing, G. Xingming, International Journal of Solids and Structures **43**(25-26), 7793 (2006). DOI 10.1016/j.ijsolstr.2006.04.015

[102] P.H. Mayrhofer, D. Music, J.M. Schneider, Applied Physics Letters **88**(7), 071922 (2006). DOI 10.1063/1.2177630

[103] C. Mitterer, P.H. Mayrhofer, M. Beschliesser, P. Losbichler, P. Warbichler, F. Hofer, P.N. Gibson, W. Gissler, H. Hruby, J. Musil, Surface and Coatings Technology **120**, 405 (1999)

[104] P. Zeman, R. Čerstvý, P.H. Mayrhofer, C. Mitterer, J. Musil, Materials Science and Engineering: A **289**(1), 189 (2000)

[105] J. Musil, P. Karvankova, J. Kasl, Surface and Coatings Technology **139**(1), 101 (2001)

[106] P.H. Mayrhofer, C. Mitterer, L. Hultman, H. Clemens, Progress in Materials Science **51**(8), 1032 (2006). DOI 10.1016/j.pmatsci.2006.02.002

[107] S. Hao, B. Delley, S. Veprek, C. Stampfl, Physical Review Letters **97**(8), 86102 (2006). DOI 10.1103/PhysRevLett.97.086102

[108] R.F. Zhang, A.S. Argon, S. Veprek, Physical Review Letters **102**(1), 15503 (2009). DOI 10.1103/PhysRevLett.102.015503

[109] R.F. Zhang, A.S. Argon, S. Veprek, Physical Review B **79**(24), 245426 (2009). DOI 10.1103/PhysRevB.79.245426

[110] S. Veprek, A. Niederhofer, K. Moto, T. Bolom, H.D. Männling, P. Nesladek, G. Dollinger, A. Bergmaier, Surface and Coatings Technology **133**, 152 (2000)

[111] S. Veprek, S. Reiprich, Thin Solid Films **268**(1-2), 64 (1995)

[112] V.V. Brazhkin, A.G. Lyapin, R.J. Hemley, Philosophical Magazine A **82**(2), 231 (2002)

[113] S. Veprek, M.G.J. Veprek-Heijman, P. Karvankova, J. Prochazka, Thin Solid Films **476**(1), 1 (2005). DOI 10.1016/j.tsf.2004.10.053

[114] S. Veprek, H.D. Männling, A. Niederhofer, D. Ma, S. Mukherjee, Journal of Vacuum Science & Technology B: Microelectronics and Nanometer Structures **22**, L5 (2004)

[115] S. Veprek, A.S. Argon, R.F. Zhang, Philosophical Magazine **90**(31), 4101 (2010). DOI 10.1080/14786430903365294

[116] A.A. Voevodin, J.M. Schneider, C. Rebholz, A. Matthews, Tribology International **29**(7), 559 (1996). DOI 10.1016/0301-679X(95)00121-J

[117] A.A. Voevodin, S.V. Prasad, J.S. Zabinski, Journal of Applied Physics **82**, 855 (1997)

[118] J.C. Sánchez-López, D. Martínez-Martínez, M.D. Abad, A. Fernández, Surface and Coatings Technology **204**(6-7), 947 (2009). DOI 10.1016/j.surfcoat.2009.05.038

[119] D. Martínez-Martínez, C. López-Cartés, R. Gago, A. Fernández, J.C. Sánchez-López, Plasma Processes and Polymers **6**(S1), S462 (2009). DOI 10.1002/ppap.200931002

[120] A.A. Voevodin, J.P. ONeill, S.V. Prasad, J.S. Zabinski, Journal of Vacuum Science and Technology A: Vacuum, Surfaces, and Films **17**, 986 (1999)

[121] A.A. Voevodin, J.P. O'Neill, J.S. Zabinski, Thin Solid Films **342**(1-2), 194 (1999). DOI 10.1016/S0040-6090(98)01456-4

[122] M.D. Abad, M.A. Muñoz-Márquez, S. El Mrabet, A. Justo, J.C. Sánchez-López, Surface and Coatings Technology **204**(21), 3490 (2010). DOI 10.1016/j.surfcoat.2010.04.019

[123] Y.T. Pei, D. Galvan, J.T.M. De Hosson, Journal of Vacuum Science and Technology A: Vacuum, Surfaces, and Films **24**, 1448 (2006)

[124] T. Vasco Boutos, R. Sanjines, A. Karimi, Surface and Coatings Technology **188**, 409 (2004). DOI 10.1016/j.surfcoat.2004.08.039

[125] D. Chen, X.L. Ma, Y.M. Wang, Acta Materialia **53**(19), 5223 (2005). DOI 10.1016/j.actamat.2005.08.003

[126] H.D. Männling, D.S. Patil, K. Moto, M. Jilek, S. Veprek, Surface and Coatings Technology **146**, 263 (2001)

[127] R.A. Andrievski, Surface and Coatings Technology **201**(13), 6112 (2007). DOI 10.1016/j.surfcoat.2006.08.119

[128] A.D. Korotaev, D.P. Borisov, V.Y. Moshkov, S.V. Ovchinnikov, K.V. Oskomov, Y.P. Pinzhin, V.M. Savostikov, A.N. Tymentsev, Russian Physics Journal **50**(10), 969 (2007)

[129] Y. Qiu, S. Zhang, B. Li, Y. Wang, J.W..W. Lee, F. Li, D. Zhao, Surface and Coatings Technology (2012). DOI 10.1016/j.surfcoat.2012.03.010

[130] J. Musil, H. Hruby, P. Zeman, H. Zeman, R. Čerstvy, P.H. Mayrhofer, C. Mitterer, Surface and Coatings Technology **142**, 603 (2001)

[131] Y.J. Kim, T.J. Byun, H.Y. Lee, J.G. Han, Surface and Coatings Technology **202**(22-23), 5508 (2008). DOI 10.1016/j.surfcoat.2008.06.028

[132] P.L. Sun, C.Y..Y. Su, T.P..P. Liou, C.H..H. Hsu, C.K..K. Lin, Journal of Alloys and Compounds **509**(6), 3197 (2011). DOI 10.1016/j.jallcom.2010.12.057

[133] P. Angerer, J.M. Lackner, M. Wiessner, G.A. Maier, International Journal of Refractory Metals and Hard Materials (2012). DOI 10.1016/j.ijrmhm.2012.07.008

[134] H.C. Barshilia, S. Prakash, P. Aithu, K.S. Rajam, Transactions of the Institute of Metal Finishing **82**(4), 1 (2004)

[135] H.C. Barshilia, M.S. Prakash, D.V. Sridhara Rao, K.S. Rajam, Surface and Coatings Technology **195**(2-3), 147 (2005). DOI 10.1016/j.surfcoat.2004.09.035

[136] H. Liao, B. Normand, C. Coddet, Surface and Coatings Technology **124**(2-3), 235 (2000). DOI 10.1016/S0257-8972(99)00653-2

[137] C. Rincón, G. Zambrano, A. Carvajal, P. Prieto, H. Galindo, E.M.a. accent]nez, A. Lousa, J. Esteve, Surface and Coatings Technology **148**(2-3), 277 (2001). DOI 10.1016/S0257-8972(01)01360-3

[138] B.R. Pujada, F.D. Tichelaar, G. Janssen, Surface and Coatings Technology **203**(5-7), 562 (2008). DOI 10.1016/j.surfcoat.2008.05.051

[139] S.H. Ahn, J.H. Yoo, J.G. Kim, J.G. Han, Surface and Coatings Technology **163**, 611 (2003)

[140] D.B.B. Lee, Journal of Nanoscience and Nanotechnology **9**(12), 7416 (2009)

[141] G.D. Mohan, B.E. Klamecki, Wear **74**(1), 85 (1981)

[142] V.A. Pugsley, G. Korn, S. Luyckx, H.G. Sockel, W. Heinrich, M. Wolf, H. Feld, R. Schulte, International Journal of Refractory Metals and Hard Materials **19**(4), 311 (2001)

[143] B. Porankiewicz, J. Sandak, C. Tanaka, Wood Science and Technology **39**(3), 225 (2005). DOI 10.1007/s00226-004-0282-0

[144] M. Gauvent, E. Rocca, P.J. Meausoone, P. Brenot, Wear **261**(9), 1051 (2006). DOI 10.1016/j.wear.2006.03.036

[145] J.Y. Sheikh-Ahmad, J.A. Bailey, Journal of Wood Science **45**(6), 445 (1999)

[146] J. Ratnasingam, T. Pew Ma, G. Ramasamy, Journal of Applied Sciences **10**(22), 2881 (2010). DOI 10.3923/jas.2010.2881.2886

[147] J.P. Manaud, A. Poulon, S. Gomez, Y.L. Petitcorps, Surface and Coatings Technology **202**(2), 222 (2007). DOI 10.1016/j.surfcoat.2007.05.024

[148] R. Polini, M. Barletta, G. Cristofanilli, Thin Solid Films **519**, 1629 (2010). DOI 10.1016/j.tsf.2010.07.128

[149] Q. Wei, Z. Yu, L. Ma, D. Yin, International Journal of Modern Physics B **23**, 1676 (2009)

[150] Q. Wei, Z.M. Yu, M.N.R. Ashfold, L. Ma, Z. Chen, Diamond and Related Materials **19**, 1144 (2010). DOI 10.1016/j.diamond.2010.04.004

[151] P. Lu, X. Xiao, M. Lukitsch, A. Sachdev, Y.K. Chou, Surface and Coatings Technology **206**(7), 1860 (2011). DOI 10.1016/j.surfcoat.2011.08.022

[152] S.V.N. Naidu, A.M. Sriramamurthy, P.R. Rao, Journal of Phase Equilibria **5**(3), 289 (1984)

[153] Z.A. Hamid, I.M. Ghayad, K.M. Ibrahim, Surface and Interface Analysis **37**(6), 573 (2005). DOI 10.1002/sia.2052

[154] B.S. Yau, C.W. Chu, D. Lin, W. Lee, J.G. Duh, C.H. Lin, Thin Solid Films **516**(8), 1877 (2008). DOI 10.1016/j.tsf.2007.10.007

[155] M. Brieseck, M. Bohn, W. Lengauer, Journal of Alloys and Compounds **489**(2), 408 (2010). DOI 10.1016/j.jallcom.2009.09.137

[156] S. Maniv, W.D. Westwood. United States Patent 4,392,931 (1983)

[157] C.F. Morrison, Jr. United States Patent 4,162,954 (1979)

[158] R. Nishikawa, S. Satoyama, Y. Ito, H. Jyo. United States Patent 4,441,974 (1984)

[159] H.M. Lin, J.G. Duh, R. Wei, C. Rincon, J.W. Lee, Surface and Coatings Technology **2-5**, 1460 (2010). DOI 10.1016/j.surfcoat.2010.07.070

[160] V. Kouznetsov, K. Macak, J.M. Scheider, U. Helmsesrsson, I. Petrov, Surface and Coatings Technology **122**(2), 290 (1999)

[161] Y. Liu, E. Koep, M. Liu, Chemistry of Materials **17**(15), 3997 (2005)

[162] Y. Zhang, Y. Liu, M. Liu, Chemistry of Materials **18**(19), 4643 (2006)

[163] C. Worsch, C. Rüssel, Thin Solid Films **518**(17), 4798 (2010). DOI 10.1016/j.tsf.2010.01.032

[164] B.P. Dhonge, T. Mathews, S.T. Sundari, M. Kamruddin, S. Dash, A.K. Tyagi, Surface and Coatings Technology **205**(7), 1838 (2010). DOI 10.1016/j.surfcoat.2010.08.026

[165] T. Struppert, A. Heft, B. Grünler, Thin Solid Films (2011)

[166] S.A. Catledge, Y.K. Vohra, Journal of Applied Physics **84**(11), 6469 (1998). DOI doi:10.1063/1.368975

[167] J.A. Thornton, Journal of Vacuum Science & Technology A: Vacuum, Surfaces, and Films **11**(4), 666 (1974)

[168] J.A. Thornton, Journal of Vacuum Science & Technology A: Vacuum, Surfaces, and Films **4**(6), 3059 (1986). DOI 10.1116/1.573628

[169] A. Anders, Thin Solid Films **518**(15), 4087 (2010). DOI 10.1016/j.tsf.2009.10.145

[170] Schematic for scanning electron microscopy column (2003). URL http://www-archive.mse.iastate.edu/microscopy/path2.html

[171] JEOL JSM 6400F (2012). URL http://www.gentechscientific.com/jeol-jsm-6400f-sem

[172] FEI Quanta 650 (2012). URL http://www.uab.edu/metals/facilities/58-characteequip

[173] B.H. Toby, Journal of Applied Crystallography **38**(6), 1040 (2005)

[174] S. Kabekkodu (ed.), *Powder Diffraction File* (International Center for Diffraction Data, Newtown Square, Pennsylvania, 2007)

[175] K.M.B. Siegbahn, E.F. Barnett. United States Patent 3,617,741 (1971)

[176] K.M.B. Seigbahn. United States Patent 3,567,926 (1971)

[177] J.F. Moulder, W.F. Stickle, P.E. Sobol, K.D. Bomben, *Handbook of X-ray Photoelectron Spectroscopy* (ULVAC-PHI, Inc., Chigasaki, Japan, 1995)

[178] G.G. Stoney, Proceedings of the Royal Society of London. Series A, Containing Papers of a Mathematical and Physical Character pp. 172–175 (1909)

[179] M.A..A. Moram, M.E..E. Vickers, Reports on Progress in Physics **72**(3), 036502 (2009). DOI 10.1088/0034-4885/72/3/036502

[180] C.B. Masters, N.J. Salamon, International journal of engineering science **31**(6), 915 (1993)

[181] Optical interferometry fringes (2012). URL http://zemetrics.com/optical-profilers-about.shtml

[182] Gwyddion SPM Data Visualization and Analysis software (2004). URL http://gwyddion.net

[183] X. Chen, J.J. Vlassak, Journal of Materials Research **16**(10), 2974 (2001)

[184] J. Ahn, K.L. Mittal, R.H. MacQueen, ASTM Special Technical Publications **640**, 134 (1978). DOI 10.1520/STP38630S

[185] D. Beegan, S. Chowdhury, M.T. Laugier, Surface and Coatings Technology **201**(12), 5804 (2007). DOI 10.1016/j.surfcoat.2006.10.031

[186] J. Creus, H. Mazille, H. Idrissi, Surface and Coatings Technology **130**(2-3), 224 (2000)

[187] K. Fuchs, P. Rödhammer, E. Bertel, F.P. Netzer, E. Gornik, Thin Solid Films **151**(3), 383 (1987). DOI 10.1016/0040-6090(87)90137-4

[188] A. Fischer-Cripps, *Introduction to Contact Mechanics*, 2nd edn. (Springer Science, New York, 2007)

[189] *NIST X-ray Photoelectron Spectroscopy Database, Version 3.5* (National Institute of Standards and Technology, Gaithersburg, MD, 2003). URL http://srdata.nist.gov/xps/

[190] Y. Li, Y. Gao, B. Xiao, T. Min, Y. Yang, S. Ma, D. Yi, Journal of Alloys and Compounds **509**(17), 5242 (2011). DOI 10.1016/j.jallcom.2011.02.009

[191] B. Xiao, J.D..D. Xing, J. Feng, C.T..T. Zhou, Y.F..F. Li, W. Su, X.J..J. Xie, Y.H..H. Cheng, Journal of Physics D: Applied Physics **42**(11), 115415 (2009). DOI 10.1088/0022-3727/42/11/115415

[192] B. Xiao, J. Feng, C.T. Zhou, J.D. Xing, X.J. Xie, Y.H. Chen, Chemical Physics Letters **459**(1-6), 129 (2008). DOI 10.1016/j.cplett.2008.05.072

[193] C. Jiang, Applied Physics Letters **92**(4), 041909 (2008). DOI 10.1063/1.2838345

[194] S.I. Kim, C.W. Lee, Physica Status Solidi (c) **4**(12), 4475 (2007). DOI 10.1002/pssc.200777240

[195] X. Chen, J.J. Vlassak, Journal of Materials Research **16**(10), 2974 (2001)

[196] Q. Liang, S.A. Catledge, Y.K. Vohra, Applied Physics Letters **83**(24), 5047 (2003). DOI 10.1063/1.1633972

[197] Q. Liang, A. Stanishevsky, Y.K. Vohra, Thin Solid Films **517**(2), 800 (2009). DOI 10.1016/j.tsf.2008.08.171

[198] S. Chowdhury, J. Borham, S.A. Catledge, A.W. Eberhardt, P.S. Johnson, Y.K. Vohra, Diamond and Related Materials **17**(4-5), 419 (2008). DOI 10.1016/j.diamond.2007.08.041

[199] C. Castiglioni, M. Tommasini, G. Zerbi, Philosophical Transactions of the Royal Society A: Mathematical, Physical, and Engineering Sciences **362**(1824), 2425 (2004). DOI 10.1098/rsta.2004.1448

[200] A.C. Ferrari, J. Robertson, Physical Review B **63**(12), 121405 (2001). DOI 10.1103/PhysRevB.63.121405

[201] A.C. Ferrari, J. Robertson, Philosophical Transactions of the Royal Society A: Mathematical, Physical, and Engineering Sciences **362**(1824), 2477 (2004). DOI 10.1098/rsta.2004.1452

[202] A. Lousa, J. Romero, E. Martinez, J. Esteve, F. Montalà, L. Carreras, Surface and Coatings Technology **146**, 268 (2001)

[203] O. Renault, Journal of The Electrochemical Society **146**(10), 3731 (1999). DOI 10.1149/1.1392541

[204] J.F..F. Whitacre, Z.U..U. Rek, J.C..C. Bilello, S.M..M. Yalisove, Journal of Applied Physics **84**(3), 1346 (1998). DOI 10.1063/1.368204

[205] D.R. Lide (ed.), *CRC Handbook of Chemistry and Physics*, 83rd edn. (CRC Press, Boca Raton, FL, 2002)

[206] P.H. Mayrhofer, G. Tischler, C. Mitterer, Surface and Coatings Technology **142**, 78 (2001)

[207] C.E. Carlton, P.J. Ferreira, Acta Materialia **55**(11), 3749 (2007). DOI 10.1016/j.actamat.2007.02.021

[208] J. Schiøtz, F.D. Di Tolla, K.W. Jacobsen, Nature **391**(6667), 561 (1998). DOI 10.1038/35328

[209] P. Barai, G.J. Weng, International Journal of Plasticity **25**(12), 2410 (2009). DOI 10.1016/j.ijplas.2009.04.001

[210] C.S. Pande, K.P. Cooper, Progress in Materials Science **54**(6), 689 (2009). DOI 10.1016/j.pmatsci.2009.03.008

[211] C. Lu, Y.W. Mai, Y.G. Shen, Journal of Materials Science **41**(3), 937 (2006). DOI 10.1007/s10853-006-6577-9

[212] J. Luo, R. Stevens, Ceramics International **25**(3), 281 (1999)

[213] Y.V. Milman, S.I. Chugunova, I.V. Goncharova, T. Chudoba, W. Lojkowski, W. Gooch, International Journal of Refractory Metals and Hard Materials **17**(5), 361 (1999)

[214] N.M.G. Parreira, N.J.M. Carvalho, A. Cavaleiro, Thin Solid Films **510**(1-2), 191 (2006). DOI 10.1016/j.tsf.2005.12.299

[215] N.M.G. Parreira, N.J.M. Carvalho, F. Vaz, A. Cavaleiro, Surface and Coatings Technology **200**(22-23), 6511 (2006). DOI 10.1016/j.surfcoat.2005.11.020

[216] H.C. Barshilia, K.S. Rajam, Applied Surface Science **255**(5), 2925 (2008). DOI 10.1016/j.apsusc.2008.08.057

[217] P. Hones, M. Diserens, F. Lévy, Surface and Coatings Technology **120-121**, 277 (1999). DOI 10.1016/S0257-8972(99)00384-9

[218] N. Schwarzer, Q.H..H. Duong, N. Bierwisch, G. Favaro, M. Fuchs, P. Kempe, B. Widrig, J. Ramm, Surface and Coatings Technology **206**(6), 1327 (2011). DOI 10.1016/j.surfcoat.2011.08.051

[219] N. Radić, B. Gržeta, O. Milat, J. Ivkov, M. Stubičar, Thin Solid Films **320**(2), 192 (1998). DOI 10.1016/S0040-6090(97)00758-X

[220] SGTE Binary Alloy Phase Diagrams (2012). URL http://www.sgte.org/fact/documentation/SGTE/SGTE_Figs.htm

[221] R.H. Davies, A.T. Dinsdale, J.A. Gisby, J.A.J. Robinson, S.M. Martin, Calphad **26**(2), 229 (2002)

APPENDIX A

Résumé en français

Résumé

Lors de ce projet, des revêtements de CrN-WC ont été étudiés en tant que matériaux hybrides durs et résistants. Lassociation d'un carbure et dun nitrure résistant bien à la corrosion et obtenus dans des conditions optimales de dépôt permettra davoir des matériaux de protection contre lusure, la corrosion mais aussi des dépôts servant de couches tampon à du diamant nanocristallin dont ladhérence est mauvaise. Tout dabord nous avons déterminé la faisabilité du système CrN-WC et son utilisation comme couche intermédiaire pour du diamant nanocristallin. En faisant varier les paramètres de dépôt, nous avons optimisé la microstructure, les caractéristiques chimiques, mécaniques et tribologiques de nos couches. Si le système CrN-WC adhère relativement bien sur silicium, ce ne fut pas le cas sur acier. Les propriétés mécaniques de ces dépôts ont été par ailleurs plus faibles que celles que nous attendions. Nous avons ensuite étudié linfluence de la température sur nos dépôts de CrN-WC. En effet, le fait de chauffer lors du dépôt permet d'augmenter l'adhérence des couches et daméliorer leurs propriétés mécaniques. Les revêtements obtenus à haute température ont bien montré une nette amélioration de leurs diverses caractéristiques par rapport aux dépôts obtenus sans chauffage.

A.1 Introduction

Depuis l'âge de pierre [1], les outils de coupe sont des éléments omniprésents dans la société. Ils ont joué un rôle clé dans notre développement en tant qu'espèce et en tant que civilisation [2]. Bien que les outils de pierre et d'os aient été la technique utilisée pendant plus de 3 millions d'années, l'homme a cherché à améliorer en permanence celle-ci. Par exemple, des poignées ou manches ont été ajoutées pour améliorer la facilité d'utilisation de ces outils et leur efficacité [3, 4]. La cuisson des outils de pierre a augmenté leur durabilité [5]. Toutefois, après 8000

ans et l'avènement de l'âge de bronze, la métallurgie a été développée [6, 7]. Cela a débuté avec le cuivre, suivi peu après par le bronze, l'homme a alors réussi à exploiter les outils métalliques pour la première fois. Cette étape de développement a duré tout au long des périodes dynastiques de l'Egypte.

Cependant, vers 1800 avant J.-C., la métallurgie du fer a été développée [8, 9]], suivie par la fabrication de l'acier [10]. Toutefois, les premiers procédés de fabrication de l'acier étaient difficiles et coteux. Lacier n'est devenu omniprésent quau milieu du $19^{\text{ème}}$ siècle grâce au procédé de Bessemer [11]. Des améliorations dans le processus de fabrication de l'acier ont rapidement conduit à l'introduction de composés plus exotiques, tels que les carbures cémentés. Mais même ces outils modernes montrent des défauts: ils s'usent et peuvent être coteux à remplacer.

Lusure de l'outil et la corrosion sont principalement axées sur les processus de surface. Par conséquent, il existe deux méthodes pour prolonger la vie de ces outils: développer de nouveaux matériaux pour le corps de l'outil et / ou développer des systèmes de protection de surface, tels que les revêtements. En appliquant un traitement de surface, tel qu'un revêtement de protection, les propriétés d'usure de l'outil peuvent être adaptées pour des environnements d'exploitation spécifiques.

Cependant, les moyens pour produire des traitements de surface cohérents et économiques faisaient à lépoque défaut. Ce nest pas avant les années 1960, avec le développement des techniques de dépôt physique en phase vapeur, que les scientifiques ont commencé à développer des revêtements efficaces et résistants à l'usure, ce qui a considérablement amélioré la durée de vie des outils par rapport aux techniques antérieures [12–15].

A.2 Méthodologie

Ce projet se compose de trois phases d'étude sur les paramètres optimaux dobtention de dépôts durs, protecteurs à base de CrN-WC. En été 2009, une étude a été menée afin de déterminer la faisabilité de ce système: ces couches se sont révélées dures et adhérentes. Il était donc envisageable de les réaliser comme couches tampons pour du diamant nanocristallin (nc-D). Cette étude a été réalisée avec succès en faisant varier les conditions de dépôt sans chauffage. Ainsi, la microstructure, les propriétés physico-chimiques, mécaniques et tribologiques ont pu être optimisées et contrôlées. Toutefois, les dépôts de CrN-WC (obtenus sans chauffage) ont présenté des problèmes dadhérence et des propriétés mécaniques plus faibles que prévu.

Notre étude a alors consisté à vérifier leffet de la température de dépôt. Le but ici était d'augmenter l'adhérence, et aider à la ségrégation de phase spinodale - conduisant à des propriétés mécaniques améliorées. Des résultats antérieurs obtenus avec d'autres systèmes multi-phasés montrent une amélioration constante des propriétés mécaniques à des températures de dépôt élevées. Ces revêtements à haute température de dépôt ont montré une amélioration marquée dans l'industrie chimique, mécanique, de leurs propriétés tribologiques par rapport à des dépôts obtenus sans chauffage.

A chaque étape de notre étude, les propriétés des revêtements de CrN-WC ont été minutieusement déterminées. La topographie de surface a été mesurée par microscopie à force atomique (AFM) et microscopie électronique à balayage à haute résolution (HR-MEB); la structure des couches a été observée au HR-MEB sur des coupes transverses. La structure cristallographique de nos couches a été analysée par diffraction des rayons X (DRX) alors que la composition chimique a été déterminée par microanalyse X par EDS, spectroscopie Raman, et XPS. La détermination des contraintes sest faite en utilisant un profilomètre optique avec

lequel on a mesuré la courbure des substrats de Si avant et après dépôt; le calcul des contraintes a alors été possible en utilisant la formule de Stoney. Les propriétés mécaniques et tribologiques ont été étudiées par nanoindentation, scratch-tests et tribométrie pion-disque.

A.3 Résultats et Discussion

A.3.1 Etude de faisabilité

En utilisant la pulvérisation magnétron radiofréquence, des couches de Cr-WC-N ont été réalisées sur des substrats de Si et de Ti. Les revêtements binaires de WC sont extra-durs (H $\sim$ 47 GPa), malgré une granulométrie nettement plus faible ($\sim$ 3nm) que la taille de grain critique typique de Hall-Petch pour avoir un bon durcissement. Cela peut être d à la présence de deux phases : WC_{1-x} et W_2C. En outre, les revêtements étaient très peu rugueux, avec un $R_{RMS} \sim$ 1,1 nm. Malheureusement, ces films étaient partiellement délaminés à la fois sur Si et Ti. Les dépôts ternaires de Cr-WC montrent également une bonne dureté (H $\sim$ 19 GPa), avec une bonne adhérence. Ce revêtement se compose probablement des phases WC_{1-x} et Cr_7C_3. Bien que ces résultats soient prometteurs du point de vue propriétés mécaniques, ni WC ni Cr-WC na supporté le plasma micro-ondes de notre système de dépôt chimique en phase vapeur (MPCVD) afin de réaliser une couche de diamant nanocristallin (nc-D) à leur surface.

La présence dazote dans le mélange gazeux conduit de faon significative à la diminution du taux de pulvérisation de WC, résultant en un revêtement WCN de seulement 0,9 μm. Les caractérisations chimiques et structurales ont montré que le dépôt était essentiellement constitué de WCN, avec de petites quantités d'oxyde de métal et de carbone libre. La combinaison dune faible épaisseur de dépôt et de plusieurs phases dans une seule et même structure quasiment amorphe peut expliquer les propriétés mécaniques mesurées (H $\sim$ 12 GPa; E $\sim$ 246 GPa).

Cependant, ces revêtements étaient encore adhérents après traitement par MPCVD, et ont permis de servir de supports à la croissance de nc-D. Malheureusement, la rugosité de surface des revêtements nc-D était trop élevée. Cela peut être le résultat de la nucléation secondaire améliorée au cours de la croissance des revêtements de nc-D.

Même s'il n'est pas aussi dur que le revêtement de WC, le revêtement de CrN-WC montre une dureté beaucoup plus élevée que celle de WCN ou Cr-WC : H $\sim$ 30 GPa. Cela peut être du à la formation d'un nano composite constitué de CrN et WC, cette hypothèse a été vérifiée par des analyses en XPS et DRX. Cependant, il est difficile de savoir si le nano composite est formé de plusieurs phases nanocristallines, ou dun nanocristallin dans une matrice amorphe. Le dépôt de CrN-WC a également subit avec succès le traitement par MPCVD, et des films de diamant nanocristallin ont été réalisés à sa surface. Malheureusement, les revêtements de nc-D déposés sur CrN-WC ont été réalisés dans les mêmes conditions que les nc-D sur WCN. Ainsi, ces nc-D ont également montré une augmentation trop importante de leur rugosité de surface.

Dans l'ensemble, l'étude de faisabilité a été un succès et a montré lintérêt de combiner CrN et WC en une seule couche.

A.3.2 Dépôt de CrN-WC obtenus sans chauffage

A.3.2.1 Variation du mélange gazeux

Des dépôts sans chauffage de CrN-WC ont été réalisés en deux étapes. Dans la première, la puissance appliquée aux cibles est maintenue constante, alors que le mélange gazeux a été modifié pour étudier l'impact de l'augmentation de N_2. Ici, le rapport Cr:W était de 2:1 et le rapport Ar/N_2 a varié de : 80/20, 60/40 et 40/60. La modification de la pression partielle d'azote ne semble pas avoir deffet. En outre, selon les résultats obtenus en EDS, l'incorporation d'azote a été maximale avec le

mélange gazeux de $Ar/N_2 = 60/40$. Cela semble être en corrélation avec les résultats de DRX. A faible teneur en azote, l'orientation cristalline pour le revêtement est (200). Cependant, dès que lon a saturation d'azote, l'orientation cristalline est (111). Ces résultats sont également corrélés à la rugosité de surface des couches : plus la teneur en azote est importante et moins la rugosité de surface des couches est grande.

Un effet supplémentaire de modification de la concentration d'azote est observé sur la vitesse de dépôt et le mode de croissance. De faon inattendue, la pression partielle d'azote la plus basse conduit à la croissance la plus lente. De plus, on note que léchantillon pauvre en azote est ordonné, mais avec de plus gros grains. Les plus gros grains indiquent une plus grande mobilité des adatomes, ce qui peut expliquer la baisse de la vitesse de dépôt (i.e. faible durée de vie des adatomes). Cela peut aussi expliquer le niveau plus élevé de contraintes de compression dans cette couche par rapport aux autres revêtements, avec une mobilité élevée des adatomes/durée de vie courte de ces adatomes, il ny pas assez de temps pour que les processus de relaxation se produisent.

Quand on atteint la saturation en azote, les taux de croissance étaient toutefois raisonnables : 12,3 nm/min et 13,2 nm/min pour les pressions partielles intermédiaires et élevées d'azote, respectivement. Laugmentation de la pression partielle d'azote peut diminuer la mobilité des adatomes, do une durée de vie plus longue pour ces derniers, par rapport au dépôt obtenu avec peu dazote.

Malgré une saturation en azote dans les deux dépôts obtenus à pressions intermédiaires et élevées d'azote, il existe une différence dans le mode de croissance de ces deux revêtements. Le dépôt obtenu avec une pression partielle d'azote intermédiaire semble faire l'objet d'une plus grande quantité d'impacts d'ions, ce qui pousse le mode de croissance vers la frontière entre la zone 2 et la zone 3 dans le modèle de Movchan-Demchishin-Thornton (MDT). Malheureusement, cet exemple

semble souffrir de lacunes importantes, do une grande porosité. Le dépôt obtenu avec une pression élevée en azote semble se situer à l'autre extrémité de ce modèle, à la limite entre la zone T et la zone 2, et cet échantillon semble assez dense, avec une faible porosité ($\sim$ 0,3 %).

Dans l'ensemble, cette étude sur les effets de la variation de la pression partielle d'azote a été des plus intéressantes. Malheureusement, les seules tendances claires que lon peut en déduire sont que la rugosité de surface diminue lorsque la pression partielle dazote augmente et, de faon inattendue, cela conduit à une augmentation des vitesses de dépôt. Cependant, malgré l'augmentation de la porosité, le mélange gazeux intermédiaire a été choisi pour poursuivre notre étude: étudier la variation de la puissance appliquée sur les cibles de pulvérisation. Cela a été fait dans le but dobtenir des vitesses de dépôt raisonnables, avec une faible rugosité de surface et des propriétés mécaniques acceptables.

A.3.2.2 Variation de la puissance appliquée sur les cibles de pulvérisation

Dans la deuxième partie de cette étude, le mélange gazeux a été fixé à Ar/N_2 = 60/40 tandis que la puissance appliquée aux cibles a varié. Cela a entrainé des changements dans le rapport Cr:W. Cinq compositions différentes ont été créées pour étudier la relation composition-propriétés.

A faible teneur en Cr, les revêtements semblent former une " solution-solide " qui présente une structure à un seul pic large, avec la présence dautres phases sous forme de traces. Une fois une valeur critique en Cr atteinte, le film présente une structure nanocomposite. Cependant, en DRX et XPS on ne peut pas déterminer la nature exacte de ce nanocomposite. Il peut s'agir de phases nanocristallines multiples[1], ou une combinaison d'une phase nanocristalline et dune phase amorphe.

[1]Si lXPS est un excellent outil pour mesurer la structure chimique dune couche, il ne révèle pas d'information cristallographique. Normalement, les DRX auraient du révéler cette information, mais il y a un chevauchement des pics de diffraction significatifs relatifs à CrN et WC.

La composition des couches ne semble pas beaucoup influencée par la puissance appliquée aux cibles. Les propriétés mécaniques semblent diminuer avec l'augmentation de la teneur en Cr. Cependant, les films à faible teneur en Cr (Cr:W = 1.5:1 et 1:1) semblent échapper à cette tendance[2]. En outre, les propriétés mécaniques sont nettement plus faibles que prévu, sur la base des résultats de l'étude de faisabilité. Lautre tendance que lon a notée est l'augmentation de la rugosité de surface avec la teneur en Cr. Cela ne peut pas être corrélé ni avec l'évolution de la structure cristallographique, ni avec des changements dans la microstructure des couches.

Lobjectif initial détudier ce système était d'améliorer les propriétés mécaniques des composés binaires constitutifs, avec une adhérence relativement bonne et une faible rugosité de surface. Seule une faible rugosité de surface a été obtenue. L'adhérence du revêtement est faible, et dautres propriétés mécaniques faibles sont également présentées dans cette partie de notre étude. Ces résultats peuvent être dus à une combinaison du faible niveau de contraintes, dune grande porosité et dune contamination élevée en oxygène de ces films. Cependant, il y avait un échantillon qui semblait prometteur: Cr:W avec un ratio de 1,5:1. Bien que ce film montre de faibles contraintes en tension, il présente une bonne adhérence, bien meilleure que les quatre autres revêtements. Par ailleurs, ce dépôt contient moins d'oxygène par rapport aux autres revêtements nano composites.

Par conséquent, on doit être en mesure d'améliorer les résultats précédents par chauffage des substrats lors des dépôts. En effet, en chauffant le dépôt lors de sa croissance, sa composition et ses propriétés mécaniques peuvent s'améliorer grâce notamment à une meilleure adhérence, une porosité plus faible, moins de contamination en oxygène, et la création de contraintes plus importantes. En outre, les meilleurs nano composites présentent une ségrégation de phase complète.

[2]Pour un ratio Cr:W = 1,5:1 le diffractogramme de RX est très complexe, c'est-à-dire qu'il s'agit probablement d'un nano composite et pas d'une solution solide.

Comme il s'agit d'un processus thermodynamique, le chauffage des substrats ne peut quêtre bénéfique.

A.3.3 Dépôts de CrN-WC obtenus en chauffant

A.3.3.1 Dépôt de films de CrN-WC à hautes températures : effet de la composition des couches

Létape consistant à chauffer à haute température les dépôts en cours de croissance sest faite en deux parties complémentaires. Tout d'abord, des films de CrN-WC minces ont été réalisés sur silicium, sans sous-couche. Deux compositions différentes (Cr:W = 0,5:1, 3:1) ont été étudiées pour quatre températures différentes (400 °C, 270 °C, 180 °C, et sans chauffage externe (NEH)). Le temps de dépôt a été fixé, dans le but dobtenir des films de 500 nm d'épaisseur.

La structure chimique de ces huit échantillons a été caractérisée par EDS et XPS. Les dépôts contenant peu de Cr sont composés des phases WC, W_2C, CrN et Cr_2N. En outre, on note la présence, même faible, doxyde CrO_x et de carbone libre. Les films minces contenant beaucoup de Cr ont une structure similaire, mais le carbure de tungstène est remplacé par un oxyde, CrO_x. De plus, il n'y a plus trace de carbone libre. Une tendance intéressante de ces résultats est la réduction de la teneur en Co (provenant de la cible de WC-Co) lorsque la teneur en Cr augmente. Les résultats en EDS montrent également la diminution de la contamination en oxygène par rapport aux dépôts obtenus sans chauffage.

En utilisant le HR-MEB, les épaisseurs et les modes de croissance des films peuvent être déterminés. Toutes les couches ont des épaisseurs inferieures à 500 nm. Toutefois, les écarts les plus importants se produisent lorsque le dépôt est chauffé, cela est lié à la mobilité élevée des adatomes et des temps plus courts de leur présence en surface.

Les dépôts contenant peu de Cr sont plus denses, et ont une structure

colonnaire mais pas très marquée. En combinant ceci avec la morphologie de surface, les échantillons à faible teneur en Cr se situent dans la zone 2 du modèle de MDT. Les dépôts contenant beaucoup de Cr sont également dans cette zone, mais leur structure colonnaire est plus marquée ce qui les situe près dune zone limite entre les zones 2 et 3. Malheureusement, les mesures de rugosité de surface ne peuvent pas être mises en corrélation avec la microstructure. Toutefois, tous les films sont relativement peu rugueux, mais les meilleurs résultats sont obtenus pour les dépôts réalisés en chauffant à haute température. De même, il ne semble pas y avoir de corrélation entre les contraintes et la microstructure, la composition, ou même la température de dépôt.

Bien que les propriétés mécaniques des films minces changent avec la température, il n'y a pas de tendance claire. La seule observation réelle est une augmentation de la rigidité de l'échantillon, et une certaine amélioration de sa dureté aux températures les plus élevées. Cela peut être lié à un niveau de contraintes plus important. Ce résultat sapplique pour les échantillons à faible et à haute teneur en Cr. Toutefois, les valeurs expérimentales obtenues sont beaucoup plus faibles que celles attendues suite à l'étude de faisabilité.

En plus des méthodes de caractérisation standards, nos films minces de CrN-WC ont été soumis au procédé MPCVD afin dêtre recouverts dune couche de nc-D. Alors que tous les échantillons ont résisté au traitement par MPCVD, la plupart ne présente pas de dépôt nc-D. Seuls trois des huit échantillons montrent la présence dun dépôt de nc-D. Ces trois échantillons sont ceux obtenus avec une teneur élevée en chrome et à 390 °C, 270 °C, et NEH. Toutefois, un seul de ces échantillons (dépôt fait à 270 °C) semble avoir un revêtement nc-D recouvrant toute sa surface. Les deux autres échantillons montrent des signes de croissance partielle de nc-D, mais pas une coalescence complète. Bien qu'il n'y ait pas d'explication claire des effets de la température sur la nucléation de nc-D, il peut y avoir une

explication sur la raison pour laquelle seuls les échantillons à teneur élevée en chrome permettent celle-ci. Comme indiqué précédemment, les résultats dEDS indiquent une diminution de la teneur en Co pour les échantillons contenant beaucoup de Cr et déposés à haute température. Or, le cobalt est connu pour être un catalyseur pour la croissance de nanotubes de carbone graphite, sa faible présence pourrait expliquer une meilleure nucléation de nc-D.

A.3.3.2 Dépôt de films de CrN-WC à hautes températures : effet sur les propriétés mécaniques des couches

La seconde partie de cette étude a consisté à examiner lévolution des propriétés mécaniques en fonction de la composition chimique de nos couches. Six revêtements différents, avec des ratios de cibles Cr:W de 2:1, 1.5:1, 1.25:1, 1:1, 0.75:1 et 0.6:1, ont été réalisés à 400 °C. Dautres revêtements comme CrN, WC, et WCN ont également été déposés à haute température afin d'étudier les effets de cette dernière sur la croissance des constituants des couches de CrN-WC.

En EDS, nous avons vérifié la composition chimique de nos systèmes de revêtement, ce qui nous a aidés pour la planification de nos futures expériences. Pour les systèmes WC et WCN, les résultats dEDS sont cohérents. Toutefois, les diffractogrammes de RX montrent une différence importante pour le revêtement de WCN. Au cours de l'étude de faisabilité, un revêtement de WCN a été déposé. Le diffractogramme de RX obtenu pour ce revêtement présentait un seul pic large (FWHM $\sim$ 6,1°), alors que le nouveau diffractogramme montrerait que ce dépôt est constitué de plusieurs phases. Toutefois, lXPS a indiqué la présence dune seule phase: WCN. Par conséquent, on peut conclure que ce revêtement était presque amorphe.

Nous nous sommes ensuite intéressés au dépôt de revêtement WCN à haute température. La résultante DRX montre des pics multiples, avec une largeur à

mi-hauteur (FWHM) beaucoup plus étroite. Apparemment, il semblerait ny avoir quune seule phase, avec des cristaux bien définis. Toutefois, le revêtement CrN, que lon croyait cubique (comme cela était prévu selon les conditions de dépôt adoptées), est en fait hexagonal selon les résultats en EDS. Cela a été confirmé par DRX.

Dans le cas des revêtements CrN-WC déposés à haute température, les résultats dEDS révèlent des différences significatives entre le ratio théorique Cr:W et le ratio obtenu expérimentalement. Si ces revêtements avaient été déposés à basse température, ils seraient de bons compléments des dépôts ayant un ratio Cr:W = 1:1. Cependant, l'utilisation du chauffage a amélioré la formation de phases, et comme le montrent les DRX (Fig. 3.46), ces revêtements ne semblent pas être une solution solide. Lorsque l'on compare les divers diffractogrammes, celui du dépôt ayant un ratio Cr:W = 0,75:1 se démarque. Une étude fine des intensités relatives des pics confirme quil y a eu un problème avec ce dépôt et donc, que les résultats le concernant sont erronés.

Nous avons par la suite étudié la morphologie de surface et la microstructure de nos couches par HR-MEB. A nouveau, contre toute attente, le film de CrN présente une structure poreuse formée de colonnes effilées. Alors que la température normalisée situerait son mode de croissance dans la zone 2, le résultat obtenu expérimentalement donne un revêtement de zone 1. Ceci est conforté par l'état de contraintes en tension du revêtement CrN. Les dépôts de WC et de WCN montrent une croissance caractéristique de la zone T, le revêtement de WCN étant dans une zone limite entre les zones T et 2. Les micrographies des revêtements de CrN-WC montrent quils présentent des microstructures relativement denses avec un mode de croissance situé en zone T, zone 2, et même parfois en zone 3. En outre, les contraintes pour tous les revêtements de CrN-WC sont en compression. Malheureusement, il ne semble pas y avoir de corrélation entre l'état de contraintes et la composition ou la microstructure des couches.

Nous allons à présent aborder les propriétés mécaniques déterminées pour nos couches. Ces propriétés ont été caractérisées par nanoindentation et du scratch-test. La nanoindentation permet de définir à la fois H et E pendant que le scratch-test donne les charges critiques (pour la déformation et les dommages) et H_s.

Selon les résultats de nanoindentation des revêtements constitutifs, le revêtement WCN est le plus dur et le revêtement CrN est le plus mou. Ceci est corroboré par les résultats précédents : en effet, WCN est dense et monophasé alors que CrN est très poreux et présente une structure en forme de colonnes effilées. En ce qui concerne les revêtements de CrN-WC, un manque de diversification dans les résultats nous a quelque peu surpris. Cinq des six revêtements présentent des propriétés quasiment identiques (H $\sim$ 21,2 GPa; E $\sim$ 307 GPa). Bien que ce soit une amélioration significative des propriétés mécaniques des revêtements déposés à basse température, on est encore bien au-dessous de l'état de l'art dans l'industrie des revêtements durs en termes de dureté et module de Young.

Malheureusement, les résultats de H_s nont pas apporté dinformations complémentaires. En moyenne, les valeurs sont significativement plus faibles que les résultats obtenus en nanoindentation. Les valeurs de H_s devraient être relativement proches de celles obtenues en nanoindentation. Cependant, les effets du substrat peuvent être importants dans notre cas. En moyenne, la profondeur du profil obtenu à la première charge critique est plus grande que l'épaisseur du revêtement. Comme il n'y a aucune preuve de délaminage à cette charge, la trace doit être considérée comme provenant dune déformation plastique significative à la fois dans le revêtement et le substrat. Cela affecte donc les mesures de H_s. La seule faon de déterminer correctement la dureté à laide de scratch-tests serait dutiliser un indenteur significativement plus petit et des charges très faibles. Cela permettrait de maintenir le champ de contraintes contenues dans l'échantillon, et éliminerait les effets sur le substrat H_s.

Le même problème sest produit avec les charges critiques. La déformation plastique du revêtement a sensiblement été affectée par le substrat, donc les résultats obtenus ne sont pas fiables. En tant que telles, les valeurs pour la première charge critique (début de fissuration conforme), la deuxième charge critique (début de délaminage du revêtement par écaillage), et la charge critique finale (début darrachement du revêtement du substrat) peuvent être sous-estimées.

A.4 Conclusions et perspectives

Les premiers résultats de l'étude de faisabilité ont été très prometteurs. Cependant, l'étude de suivi de la variation de la composition réelle a été perturbée par des problèmes de contamination par loxygène, par une adhérence faible, un état de contraintes faible, et une forte porosité des couches. Ainsi, nous navons pas pu lors de cette étude reproduire les conditions dobtention dun film dur de CrN-WC par exemple. Le chauffage des substrats au cours du dépôt améliore significativement les propriétés mécaniques des revêtements. Bien que n'atteignant pas la dureté élevée de l'étude de faisabilité, des couches de CrN-WC obtenues avec chauffage du substrat présentaient une bonne dureté tout en étant ductiles.

L'objectif initial dutilisation de ce système CrN-WC était soit de lutiliser comme couche tampon pour des dépôts de nc-D, soit comme revêtement de protection pour l'industrie de la coupe (métal et/ou bois). Malheureusement, il ne nous a pas été possible, dans le temps imparti, de réaliser des essais réels de nos systèmes de dépôts sur des outils de coupe mais maintenant que ceux-ci sont optimisés, des essais de ce genre pourront être envisagés.

Par exemple, si CrN-WC doit servir de couche tampon pour du nc-D soit sur des outils de coupe ou des dispositifs biomédicaux, des tests supplémentaires avec les conditions optimales dobtention de ces dépôts sur différents substrats sont nécessaires. Même avec ces tests terminés, d'autres techniques de caractérisation

seraient nécessaires pour l'évaluation complète des dépôts de CrN-WC, et/ou dun système composite nc-D et CrN-WC.

Des exemples spécifiques de futurs essais tribologiques sont des études dusure, en corrosion, et peut-être en tribo-corrosion. Les études tribologiques/usure devraient être effectuées à la fois en laboratoire (avec un tribomètre standard pion-disque ou un simulateur de hanche) mais aussi dans des conditions de sollicitations réelles (ex. forces, efforts de coupe recréés, électrolyte physiologique pour tests de corrosion etc). Les futurs essais de corrosion devraient se faire dans des solutions acides, neutres et alcalines. Les essais de tribocorrosion permettraient détudier les effets combinés de la tribologie et la corrosion dans différents environnements.

Enfin, le développement des dépôts de CrN-WC a été plein dimprévus et de défis à relever, mais le résultat final a été la mise en place d'un système de revêtement dur qui peut être utile dans des domaines différents. Cependant, bien que cette étude ait permis au LaBoMaP et à lUAB davancer dans leurs travaux de recherche, il reste encore beaucoup à faire pour terminer cette étude du système CrN-WC, un système de revêtement de protection viable, et ses applications.

ELABORATION DE REVÊTEMENTS À BASE DE SYSTÈMES QUATERNAIRES DE METAL-NITROGEN ET CARBONES NANOSTRUCTURES

RESUME : lors de ce projet, des revêtements de CrN-WC ont été étudiés en temps que matériaux hybrides durs et résistants. L'association d'un carbure et d'un nitrure résistants bien à la corrosion et obtenus dans des conditions optimales de dépôt permettra d'avoir des matériaux de protection contre l'usure, la corrosion mais aussi des dépôts servant de couches tampon à du diamant nanocristallin dont l'adhérence est mauvaise. Tout d'abord nous avons déterminé la faisabilité du système de CrN-WC et son utilisation comme couche intermédiaire pour du diamant nanocristallin. En faisant varier les paramètres de dépôt, nous avons optimisé la microstructure, les caractéristiques chimiques, mécaniques et tribologiques de nos couches. Si le système CrN-WC adhère relativement bien sur silicium, ce ne fut pas le cas sur acier. Les propriétés mécaniques de ces dépôts ont été par ailleurs plus faibles que celles que nous attendions. Nous avons ensuite étudié l'influence de la température sur nos dépôts de CrN-WC. En effet, le fait de chauffer lors du dépôt permet d'augmenter l'adhérence des couches et d'améliorer leurs propriétés mécaniques. Les revêtements obtenus à haute température ont bien montré une amélioration marquée de leurs diverses caractéristiques par rapport aux dépôts obtenus sans chauff.

Mots clés : revêtements durs, carbures, carbonitrures, pulvérisation magnétron

NANOCOMPOSITE COATINGS BASED ON QUATERNARY METAL-NITROGEN AND NANOCARBON SYSTEMS

ABSTRACT : For this project, CrN-WC coatings are investigated as a hybrid hard and tough material. The use of a hard-carbide with a corrosion-resistant nitride may produce tailored coatings with the desired combination of properties for use as a stand-alone protective coating, or as a basis for nanocrystalline diamond deposition. The work is divided into three stages. The initial study determined the viability of the CrN-WC system, and its use as an interlayer for nanocrystalline diamond. This successful study was followed by a variation of deposition conditions at low deposition temperature. By varying the deposition parameters, the microstructure, chemical, mechanical, and tribological behavior may be optimized. While the system has relatively good adhesion to silicon substrates, its adhesion to steel was lacking. Additionally, the system showed lower than expected mechanical properties. The final step increased the deposition temperature. The aim here was to increase adhesion and improve the mechanical properties. Prior results with other systems show consistent improvement of mechanical properties at elevated deposition temperatures. The high deposition temperature coatings showed marked improvement in various characteristics over their low deposition temperature cousins.

Keywords: hard coatings, carbide, carbo-nitride, magnetron sputtering

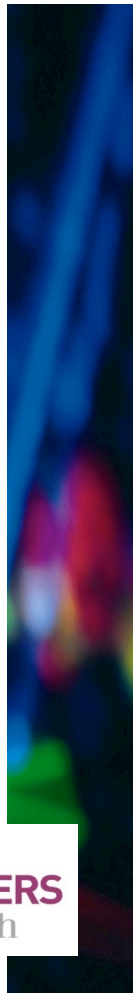

UAB

ARTS ET MÉTIERS ParisTech